Spring 4-22-2011

The Photofragmentation Processes of the closo-Carborane and the Local Structure of Transition Metal Doped Semiconducting Boron Carbide Thin Films

Jing Liu
University of Nebraska-Lincoln, jing.liu@huskers.unl.edu

THE PHOTOFRAGMENTATION PROCESSES OF THE *CLOSO*-CARBORANE AND THE LOCAL STRUCTURE OF TRANSITION METAL DOPED SEMICONDUCTING BORON CARBIDE THIN FILMS

by

Jing Liu

A DISSERTAION

Presented to the Faculty of

The Graduate College at the University of Nebraska

In Partial Fulfillment of Requirements

For the Degree of Doctor of Philosophy

Major: Physics and Astronomy

Under the Supervision of Professor Peter A. Dowben

Lincoln, Nebraska

April, 2011

THE PHOTOFRAGMENTATION PROCESSES OF THE *CLOSO*-CARBORANE AND THE LOCAL STRUCTURE OF TRANSITION METAL DOPED SEMICONDUCTING BORON CARBIDE THIN FILMS

Jing Liu, Ph.D

University of Nebraska, 2011

Advisor: Peter A. Dowben

I investigated the photofragmentation processes of various *closo*-carboranes in an effort to understand the radical-induced polymerization of the *closo*-carboranes (i.e., semiconducting film growth), based on their partial dehydrogenation during plasma-enhanced chemical vapor deposition. The chemistry of vacuum ultraviolet VUV assisted dehydrogenation processes of both the *closo*-carboranes and related *closo*-phosphacarboranes were compared by photoionization mass spectrometry studies. The dominant ion pairs were identified and compared with the energetics constructed by theoretical modeling for the possible dissociation pathways.

Transition metal (Mn, Fe, Co) doped boron carbides thin films produced by plasma-enhanced chemical vapor deposition of orthocarborane (*closo*-1,2-$C_2B_{10}H_{12}$) and metallocenes were investigated by performing K-edge extended X-ray absorption fine structure (EXAFS) and X-ray absorption near edge structure (XANES) measurements. The Mn, Fe and Co transition metal atoms dope boron carbide pairwise on adjacent icosahedra. Each transition metal atom occupies one of the icosahedral boron or carbon apical site atomic site within the icosahedral cage on adjacent edge bonded icosahedral cages. There is good agreement with experiment

and theoretical models. The local spin configurations of all the 3d transition metal doped boron carbides, Ti through to Cu, are compared using theoretical cluster or icosahedral chain calculations.

The chromium doped boron carbide thin films, fabricated by boron carbide-chromium co-deposition, were then studied by current-voltage (I-V) characteristics and temperature dependence of moment measurements. The results provide some reason to believe that magneto-resistive effects are indeed present at room temperature.

Acknowledgements

I would like to express my appreciation to my advisor Prof. Peter A. Dowen for his advice and support during my graduate studies. His leadership, encouragement, patience and kindness helped me learn and grow on the way to achieving my career goals. I believe that what I learned from him will be the wealth of my whole life.

I want to thank my committee members, Professor Evgeny Tsymbal, Professor Christian Binek, Professor Axel Enders and Professor Jennifer Brand for serving on my Supervisory Committee. I am grateful to them for their time, and the careful and critical reading of this dissertation.

I thank to all of my collaborators who made important contributions to my research. Prof. Jennifer Brand's group provided the transition metal doped boron carbide thin films. The photoionization and photofragmenation mass spectra, time of flight mass spectra and PEPIPICO spectra of photofragmentation of the *closo*-carboranes and phosphacarboranes were contributed by Prof. Eckart Rühl and Prof. N. F. Riehs at the Freie Universität Berlin, Prof. A. P. Hitchcock at the McMaster University, Dr. A. L. David Kilcoyne and Dr. T. Tyliszczak at the Lawrence-Berkeley Laboratory. The core level X-ray photoelectron spectra (XPS) of heavily hydrogenated semiconducting $C_2B_{10}Hx$ boron carbide films were provided by Prof. Jeffry A. Kelber at the University of North Texas. The theoretical calculations of electronic structure and local spin configurations of transition metal doped boron carbide by DFT were contributed by Dr. Guangfu Luo and

Prof. Wai-Ning Mei at the University of Nebraska-Omaha.

My peers, Dr. Snow Balaz, Dr. David Wisbey, Dr. Danqin Feng, Dr. Carolina Ilie, Dr. Jie Xiao, Dr. Ning Wu, Zhengzheng Zhang, Keisuke Fukutani, Juan A. Colon Santana, Lingmei Kong, Xin Zhang and Dr. Ihor Ketsman, in their own way, gave me a lot of help for my study and research.

I thank my parents, family and friends with a grateful heart. They are the source of my happiness and the motivation behind my achievements. It is impossible for me to reach this stage without their love, trust and support.

TABLE OF CONTENTS

Chapter 1 Introduction

This thesis describes two types of studies that are intimately related. I investigated photofragmentation processes for a variety of *closo*-carboranes and also characterized the local structure of transition metal doped boron carbide. The dominant fragments and the possible formation paths during the dehydrogenation, single ion fragmentation, double cation fragmentation processes of *closo*-carborane were separately indentified by both experimental and theoretical modeling approaches. The local structure of Co, Fe, Mn doped semiconducting boron carbide thin films were studied. The metal atoms are placed on paired icosahedral cages with each transition metal sitting on adjacent adjoined icosahedral carborane cages, each cage with a transition metal sitting at an apical site, with the transition metal atoms separated by roughly 5 Å.

1.1 *Closo*-carborane and semiconducting boron carbide

The icosaheral closo-carborane ($C_2B_{10}H_{12}$) is composed of 10 B-H and 2 C-H units held together by multicenter bondings. The three isomers of icosaheral *closo*-carborane, which are 1,2-(ortho), 1,7-(meta), and 1,12-dicarba-closo-dodecaborane ($C_2B_{10}H_{12}$), have attracted much attention and the molecular fragmentation of the cage molecules is a starting point for understanding the properties of semiconducting boron carbide thin film grown by plasma enhanced chemical vapor deposition (PECVD) [1-9]. The studies of the electronic structure of *closo*-carborane isomers adsorbed on various substrates have provided fundamental and useful information for fabrication of boron carbide devices [3-9].

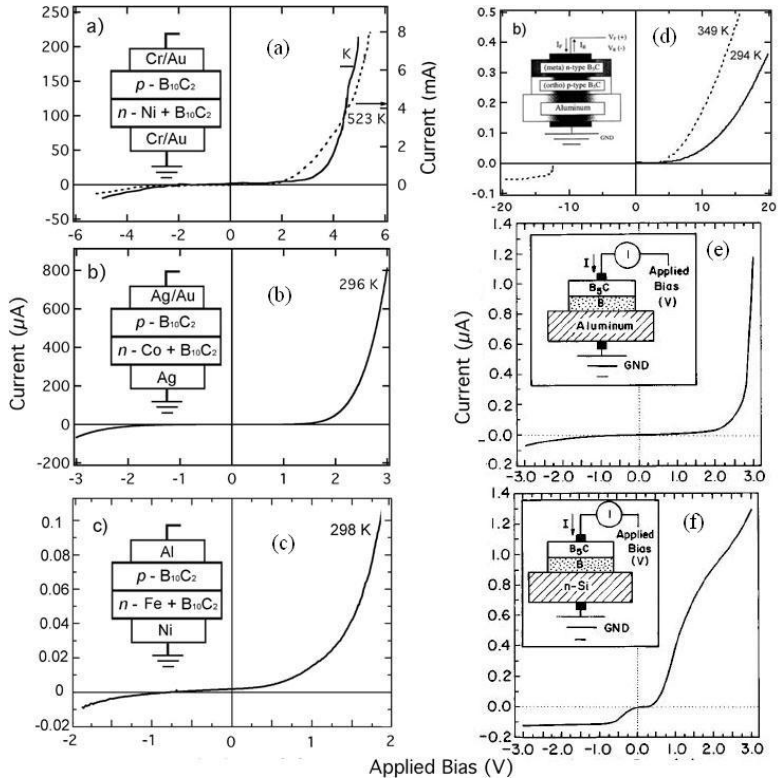

Figure 1.1 The *I–V* characteristics of all boron carbide homojunction diodes (*a*) Ni(n)-$B_{10}C_2$/(p)-$B_{10}C_2$ [17], (*b*) Co(n)-$B_{10}C_2$/(p)-$B_{10}C_2$ [18] and (*c*) Fe(n)-$B_{10}C_2$/(p)-$B_{10}C_2$ [19], heteroisomeric diode (d) p-type boron carbide/n-type boron carbide [12], and heterojunction diodes (e) boron carbide/boron/aluminum (f) and boron carbide/boron/*n*-Si(111) [11], formed by the PECVD decomposition of orthocarborane and the appropriate metallocene. Each insert shows the schematic of the diode, as assembled.

The ability to fabricate different types of semiconducting boron carbide diodes by plasma enhanced chemical vapor deposition (PECVD) of *closo*-carboranes isomers has been demonstrated [10-16]. The new class of devices made from this unusual semiconductor include homojunction diode (Figure 1.1a,b,c) [10], heterojuction diodes

[11] (Figure 1.1e,f), heteroisomeric diode (Figure 1.1d) [12,15,16] and with metal inclusion the range of homojunction devices that can be fabricated has been vastly expanded [17-20]. These diodes, because of the large capture cross-section of boron (~500 barns) may have applications in neutron detection [21]. The boron carbide thin film deposited by the orthocarborane as source molecule has been also used as barrier in this ferromagnetic-boron carbide-ferromagnetic junction has advantage of avoiding the oxidation of the ferromagnet interface which is a challenging issue for the magnetic junction by using the oxide barrier.

1.1 Metallocarboranes and transition metal doped boron carbide

The introduction of metal dopants to *closo*-carborane and boron carbide has broadened the scope of their applications. The dicarbollide ions ($C_2B_9H_{11}^{2-}$) have identical electron counts as the $C_5H_5^-$ ion and their open pentagonal faces would likely contain six delocalized electrons in five nearly equivalent atomic orbitals. As $C_5H_5^-$ ion has been known to form metallocenes (($M(C_5H_5)_2$, M = transition metal)), the metallocarboranes were predicted in which $C_2B_9H_{11}^{2-}$ ions have strong bonding to appropriate transition metal ions [23,24]. In the mid 1960s, the first metallocarborane $Fe(C_2B_9H_{11})_2^-$ was synthesized and characterized, which involve two dicarbollide ions ($C_2B_9H_{11}^{2-}$) connected via a metal center to make a “sandwich” structure [23]. The symmetrically bonded “sandwich” structure was obtained using transition metal Fe, and Cr center (Figure 1.2a). Alternative “slipped sandwich” structure (Figure 1.2b) was adopted by Cu, Ni, Cu and Pd complexes [24-26]. In addition to structures mentioned

above, metal atoms could be bonded to one or multiple borane cages framework (Figure 1.2c) [25-26].

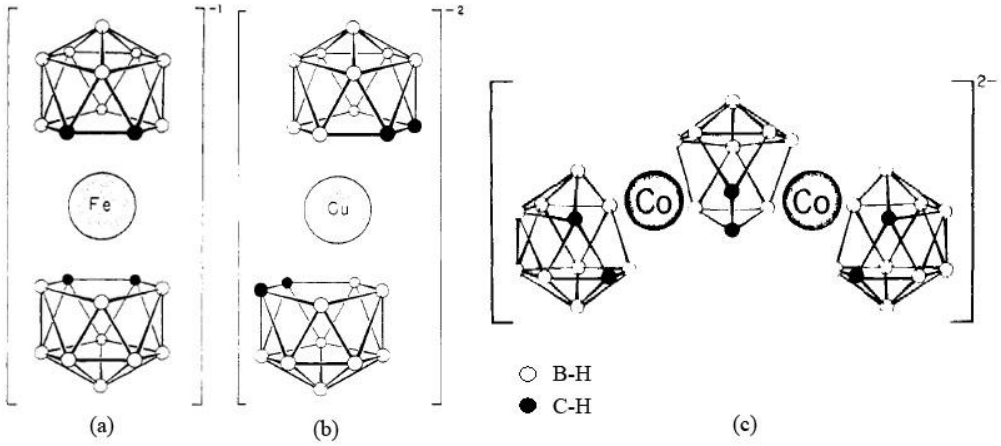

Figure 1.2. The structures of the symmetrically bonded "sandwich" derivative $Fe(C_2B_9H_{11})_2^-$ (a), the "slipped sandwich" derivative $Cu(C_2B_9H_{11})_2^{2-}$ (b) and the double-barreled complex $B_{26}C_6H_{22}Co_2^{2-}$ (c), adapted from Ref. 24, 26.

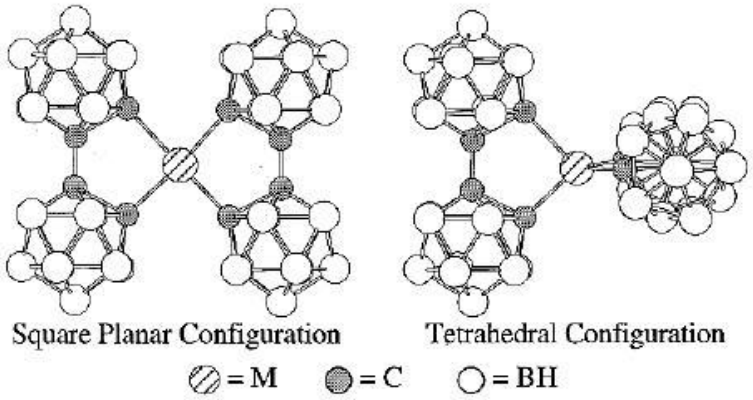

Figure 1.3. The idealized structural configurations for $[(M\{(C_2B_{10}H_{10})_2\}_2]^{2-}$. Adapted from Ref. 29.

Instead of bonding the boron and/or carbon atoms inside the cage, metal atoms act a series of unusually stable transition metal biscarborane derivatives [($M^{4-}_{n}\{(C_2B_{10}H_{10})_2\}_2]^{n-}$ (M = Co(II), Ni(II), Cu(III)) and $[(M\{(C_2B_{10}H_{10})_2\}_2]^{2-}$(M = Co(II), Zn) (Figure 1.3) with acting as bridge to bond the cages for a series of metallocarborane synthesized by crystal growth [27-29]. They showed unusual air and water stability which can be attributed to the metal-carbon bonds as parts of bulky polyhedral avoiding further substitution at carbon or metal sites, all in part because of the strong Coulombic interaction between central metal irons and ligands.

A new class of boron carbide homojunction diodes with Ni, Co, Fe doping have been produced by PECVD with orthocarborane or metacarborane, $M(C_5H_5)_2$ (M=Co, Ni, Fe) and argon as the plasma reactor gases, shown in Figure 1.1a,b,c. The properties of these diodes were observed and compared [17-20]. The Ni, Fe and Co doped boron carbide thin film grown by PECVD has showed as n-type dopant in boron carbide. The I-V characteristics of Ni doped boron carbide thin film with different Ni concentration provided clear evidence for the trend toward n-type behavior at higher doping concentrations [20]. The device characteristics of transition metal doped boron carbide indicate that even small quantities dopants can evidently affect the electronic structures of the boron carbide.

There are several key questions this thesis attempts to address. Can we understand why these cage molecule fragments are in very specific routes? Can we understand how the cages combine to form the semiconductor, so very promising for a number of applications? And can we understand how a transition metal can successfully dope this

unusual semiconductor based on the packing of icosahedra? These interrelated issues are the focus of this thesis.

References:

[1] K. Park, M. R. Pederson, L. L. Boyer, W.-N. Mei, R. F. Sabirianov, X. C. Zeng, S. S. Bulusu, S. Curran, J. Dewald, E. Day, S. Adenwalla, M. Diaz, L. G. Rosa, S. Balaz and P. A. Dowben, Phys. Rev. B **73**, 035109 (2006).

[2] S. Lee, P. A. Dowben, A. T. Wen, A. P. Hitchcock, J. A. Glass Jr. and J. T. Spencer, J. Vac. Sei. Technol. A **10**, 881 (1992).

[3] H. Zeng, D. Byun, J. Zhang, G. Vidali, M. Onellion and P. A. Dowben. Surf. Sci. **13** , 239–250 (1994).

[4] D. Byun, S. Hwang, J. Zhang, H. Zeng, F. K. Perkins, G. Vidali and P. A. Dowben, Jap. J. Appl. Phys. Lett. **34**, L941–L944 (1995).

[5] J. Zhang, D. N. Mcllroy, P. A. Dowben, H. Zeng, G. Vidali, D. Heskett and M. Onellion, J. Phys. Cond. Matt. **7,** 7185–7194 (1995).

[6] D. N. McIlroy, J. Zhang, P. A. Dowben and D. Heskett, Mat. Sci. Eng. A **217/218**, 64–68 (1996).

[7] D. N. McIlroy, C. Waldfried, T. McAvoy, J. W. Choi, P. A. Dowben and D. Heskett, Chem. Phys. Lett. **264**, 168 (1997).

[8] J. M. Carpinelli, E. W. Plummer, D. Byun and P. A. Dowben, J. Vac. Sci. Technol. B **13**, 1203–1206 (1995).

[9] A. Tillekaratne, D. Siap and M. Trenary, J. Phys. Chem. C, **112**, 8682–8689 (2008).

[10] D. N. McIlroy, S. -D.Hwang, K. Yang, N. Remmes, P. A. Dowben, A. A. Ahmad, N. J. Ianno, J. Z. Li, J.Y. Lin, H. X. Jiang, Appl. Phys. A **67**, 335 (1998).

[11] S.-D. Hwang, D. Byun, N. J. Ianno, P. A. Dowben and H. R. Kim, Appl. Phys. Lett. **68**, 1495 (1996).

[12] A. N. Caruso, P. A. Dowben, S. Balkir, N. Schemm, K. Osberg, R. W. Fairchild, O. B. Flores, S. Balaz, A. D. Harken, B. W. Robertson and J. L. Brand, Materials Science and Engineering B **135**, 129 (2006).

[13] K. Osberg, N. Schemm, S. Balkir, J. I. Brand, S. Hallbeck and P. A. Dowben, IEEE Sensors Journal **6**, 1531 (2006).

[14] S. Balaz, D. I. Dimov, N. M. Boag, K. Nelson, B. Montag, J. I. Brand and P. A. Dowben, Applied Physics A **84**, 149 (2006).

[15] A. N. Caruso, S. Balaz, B. Xu, P. A. Dowben, A. S. McMullen-Gunn, J. I. Brand, Y. B. Losovyj and D. N. McIlroy, Appl. Phys. Lett. **84**, 1302 (2004).

[16] A. N. Caruso, S. Balaz, B. Xu, Peter A. Dowben, A. S. McMullen-Gunn, J. I. Brand, Ya. B. Losovyj and D. N. McIlroy, J. Phys.: Condens. Matter **16**, L139 (2004).

[17] S.-D. Hwang, K. Yang, P. A. Dowben, A. A. Ahmad, N. J. Ianno, J. Z. Li, J. Y. Lin, H. X. Jiang and D. N. McIlroy, Appl. Phys. Lett. **70**, 1028 (1997).

[18] L. Carlson, D. Lagraffe, S. Balaz, A. Ignatove, Y. B. Losovyj, J. Choi, P. A. Dowben and J. I . Brand, Appl. Phys. A **89**, 192 (2007).

[19] P. A. Dowben, O. Kizilkaya, J. Liu, B. Montag, K. Nelson, I. F. Sabirianov and J. I. Brand, Materials Lett., **63**, 72 (2009).

[20] N. Hong, M. A. Langell, J. Liu, O. Kizilkaya and S. Adenwalla, J. Appl. Phys. **107**, 024513 (2010).

[21] A. D. Harken, E. E. Day, B. W. Robertson and S. Adenwalla, Jap. J. Appl. Phys. **44**, 444 (2005).

[22] L. Bernard, J. Monson, A. Sokolov, Z.-Y. Liu, C.-S. Yang, P. A. Dowben and B. Doudin, Appl. Phys. Lett. **83**, 3743 (2003).

[23] M. F. Hawthorne, D. C. Young and P. A. Wegner, J. Am. Chem. Soc. **87**, 1818 (1965).

[24] M. F. Hawthorne, D. C. Young, T. D. Andrews, D. V. Howe, R. L. Pilling, A. D. Pitts, M. Reintjes, L. F. Warren Jr. and P. A. Wegner, J. Am. Chem. Soc. **90,** 879 (1968).

[25] M. F. Hawthorne, L. F. Warren Jr., K. P. Callahan and N. F. Travers, J. Am. Chem. Soc. **93**, 2407 (1971).

[26] K. P. Callahan and M. F. Hawthorne, Pure Appl. Chem. **39** 475 (1974).

[27] D. A. Owen and M. F. Hawthorne, J. Am. Chem. Soc. **92**, 3194 (1970).

[28] D. A. Owen and M. F. Hawthorne, J. Am. Chem. Soc. **93**, 873 (1971).

[29] D. E. Harwell, J. McMillan, C. B. Knobler and M. F. Hawthorne, Inorg. Chem. **36**, 5951 (1997).

Chapter 2 Experimental

2.1 Sample preparation

All three isomers of icosahedra *closo*-carboranes ($C_2B_{10}H_{12}$), that is, orthocarborane (*closo*-1,2-dicarbadodecaborane or 1,2-$C_2B_{10}H_{12}$), metacarborane (*closo*-1,7-dicarbadodecaborane or 1,7-$C_2B_{10}H_{12}$), and paracarborane (*closo*-1,12-dicarbadodecaborane or 1,12-$C_2B_{10}H_{12}$), were purchased from either Katchem or Aldrich and resublimed prior to use, with purity in all cases confirmed by nuclear magnetic resonance spectroscopy (NMR) spectroscopy [1]. NMR spectra were obtained on a Bruker AVANCE400 operating at ^{1}H 400.1 MHz, ^{13}C 100.6 MHz, and ^{11}B 128.38 MHz. Proton and carbon NMR spectra were referenced to solvent and boron NMR spectra were referenced to an insert of $BF_3 \cdot Et_2O$. The assignment of the boron and proton resonances was confirmed by means of $^{11}B\{^{1}H\}$-$^{11}B\{^{1}H\}$ and $^{1}H\{^{11}B\}$-$^{11}B\{^{1}H\}$ COSY NMR spectra. The schematics of molecular structures are shown in Figure 2.1.

The transition metal doped semiconducting boron carbides thin films were provide by the group of Prof. Jennifer Brand (unless otherwise noted) and fabricated using plasma enhanced chemical vapor deposition (PECVD) with a *closo*-carborane source, a metallocene source and argon gas as plasma reactor gases. Specifically, orthocaborane (*closo*-1,2-dicarbadodecaborane or 1,2-$C_2B_{10}H_{12}$) was combined with ferrocene ($Fe(C_5H_5)_2$) and manganocene ($Mn(C_5H_5)_2$) in the PECVD process for Fe and Mn doping. Metacarborane (*closo*-1,7-dicarbadodecaborane, 1,7-$C_2B_{10}H_{12}$) and cobaltocene ($Co(C_5H_5)_2$) were used for Co doping.

The high energy electrons present in radio frequency (RF) plasma supply the energy in chemical reactions of molecules. The plasma was generated in the above

source gases in combination with the argon gas. The argon carrier gas assists in the flow, dissociation and ionization of the gaseous molecules in the reactor chamber. Chemically reactive ions bombard and deposit on the substrates to form the new semiconductor thin films. The assistant of plasma in PECVD makes the low energy growth processing possible and overcomes the kinetic limitations that may exist in other CVD processes [2].

PECVD has been approved to be a successful approach to form thin films of insulators, semiconductors and conductors in the fabrication of electrical and optical devices, such as silicon oxide, silicon nitride, organic polymers and other materials [2, 3]. The PECVD is a well established approach to grow semiconducting boron carbides which have been used to fabricate heterojunction diode with silicon [4-8], silicon carbide [9] and other semiconducting boron carbides (making these devices all boron carbide devices) [10-13] and a boron carbide transistor [14].

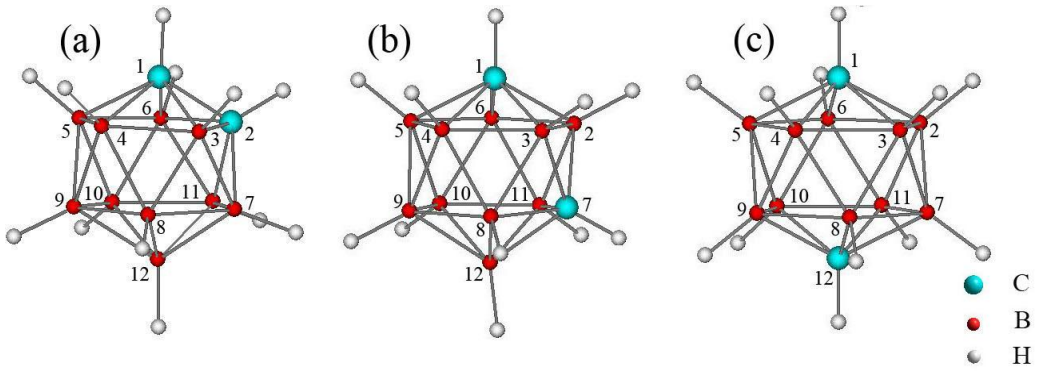

Figure 2.1. Schematics of structures of (a) *closo*-1,2-orthocarborane (1,2-$C_2B_{10}H_{12}$), (b) *closo*-1,7-metacarborane (1,7-$C_2B_{10}H_{12}$) and (c) *closo*-1,12-paracarborane (1,12-$C_2B_{10}H_{12}$).

2.2 X-ray absorption fine structure spectroscopy (XAFS): X-ray absorption near edge structure (XANES) and extended X-ray absorption fine structure (EXAFS) spectroscopies

X-ray absorption fine structure (XAFS) is the oscillatory structure of the X-ray absorption coefficient at energies near and above an X-ray absorption edge, and is also referred to X-ray absorption spectroscopy [15-17]. XAFS is an important technique for the investigation of local structural information such as coordination and local bond distances. The technique can be applied to liquids, solids, and even molecular gas systems. The application of EXAFS is elementally specific and often works at surprisingly low concentrations. Therefore, this technique is widely used in biology, geology, chemistry and material sciences to study various types of materials [18, 19].

The general experimental apparatus for XAFS includes the light source, monochromator and detector. Synchrotron radiation is an ideal light source for XAFS because of its unique characteristics of high intensity and as a tunable broadband photon energy source. There are transmission, fluorescent and electron yield detection modes for XAFS based on utilization of different monochomators and detectors [15-17]. Figure 2.2 illustrates the setup for XAFS measurement of our samples in fluorescence mode. The fluorescence measurement mode was used here for transition metal doped semiconducting boron carbide samples. In the case of thin film or dilute samples, the fluorescence mode is more sensitive to low elemental concentration than the transition mode where the signal is likely to be swamped by a large background absorption. XAFS measures the absorption coefficient $\mu(E)$ of X-rays as function of X-ray energy. In fluorescent yield mode, emitted fluorescent X-ray is detected. Thus,

coefficient μ(E) is expressed as the ratio of intensity of measured fluorescent X-ray (I_f) to intensity of incident X-ray (I_o) [15-17].

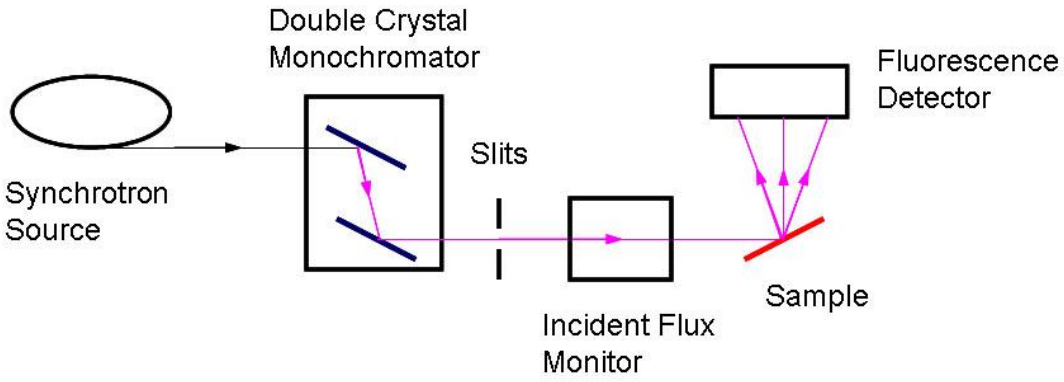

Figure 2.2. Schematics of experimental setup for XAFS measurement in fluorescence mode.

The X-ray absorption near edge structure spectroscopy (XANES) and extended X-ray absorption fine structure (EXAFS) spectroscopies of transition metal doped semiconducting boron carbide thin films were collected at the DCM beamline at the Center for Advanced Microstructures and Devices (CAMD) (Figure 2.3 and 2.4). Monochromatic light was obtained using a double crystal monochromator of Lemonnier type [18], equipped with a Ge (220) crystal pair. The estimated energy resolution was approximately 2 eV. Spectra were collected in the fluorescence yield mode, using a silicon drift detector for the iron (Fe) doped boron carbide and using the Canberra 13-element high purity germanium diode array detector for manganese (Mn) doped boron carbide. Due to the low transition metal concentrations, self-absorption is regarded as negligible and the data were not corrected for self-absorption. Two to five scans were collected to ensure reproducibility of the experimental data. The absolute energy scale was calibrated by assigning the transition metal K-edge to the first inflection point of the spectra taken from an

appropriate reference metal foil.

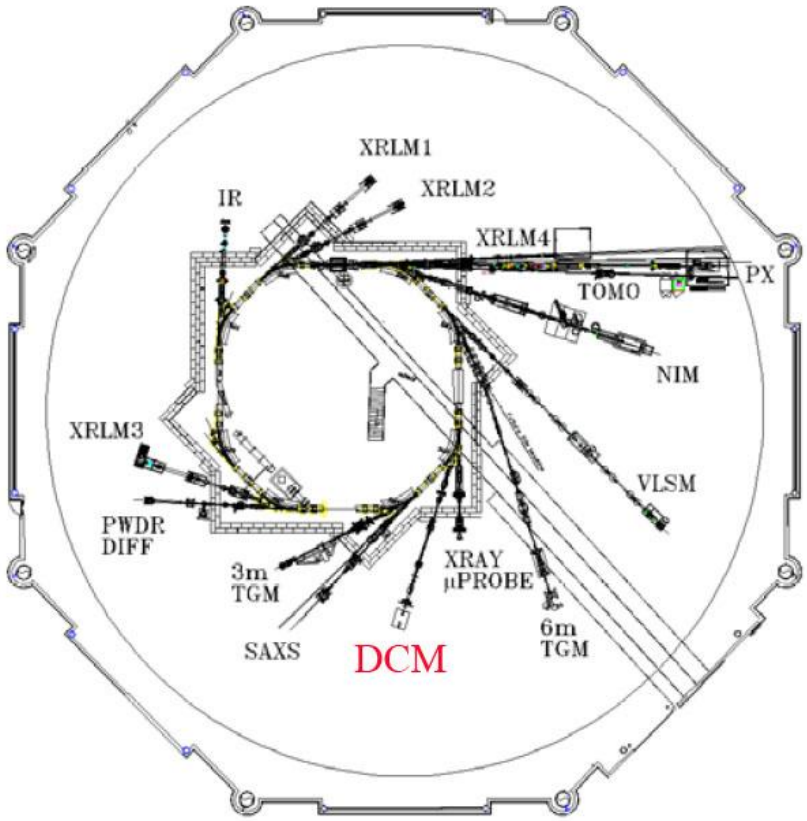

Figure 2.3. General view of the CAMD facility [19].

Figure 2.4. DCM (double crystal monochromater) beamline which was used to measure the XANES and EXAFS spectra.

In XAFS, the X-ray is absorbed by atoms through the photo-electric effect [15-17]. The sample is largely, but far from perfectly transparent to the X-ray flux below the absorption edge of the absorbing atom. The energy of absorbed X-ray photon is transferred to ejected core-level electron with a core hole left when the photon energy is at or above the edge. It results in a sharp increase (absorption edge) in absorption spectrum. The absorption edge energy is elementally specific and dependent on the atomic number of absorbing atom. It is a spectroscopic elemental fingerprint type tool for determining the constituent elements. Once the core hole is refilled, a fluorescence X-ray or Auger electron is ejected from the atom. The ejected photo-electron can be scattered by neighbor atoms and return back to the absorbing atom and interfere with itself. The interference effect of photo-electron causes the oscillatory behavior in XAFS spectrum with energy. This means if the absorbing atom is isolated, $\mu(E)$ has a sharp step at the absorption edge and is a smooth function of energy above this absorption edge. With other adjacent atoms, the electron wave emitted by absorbed atom is scattered by neighboring atoms. The outgoing and scattered parts of the final state wavefunction interfere when the initial state is localized. Thus, the oscillatory structure can be interpreted to obtain the local environment of the X-ray absorbing atom. More details will be discussed in later chapters

Above the absorption edge, the first region of 30-50 eV of XAFS is referred to as X-ray absorption near edge structure (XANES). XANES is often dominated by strong scattering processes and local atomic resonances [15-17]. The 50 eV above absorption edge region is corresponded to extended X-ray absorption fine structure (EXAFS) which exhibits oscillation behavior due to the interference effect of photoelectrons.

More detail about the theory of EXAFS will be discussed in Chapter 3. An example of Zn K edge XAFS of w-ZnO [21] is shown in Figure 2.5.

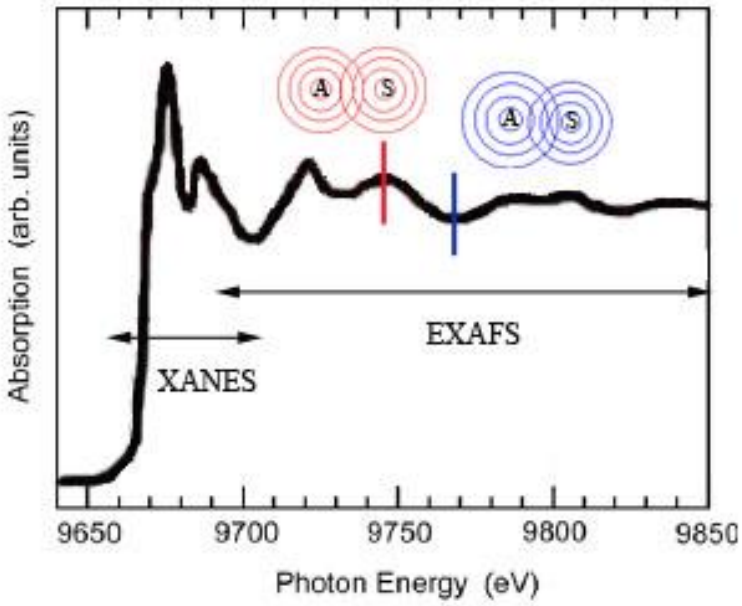

Figure 2.5. Zn K edge X-ray absorption fine structure of w-ZnO powder. Adapted from Ref [21]. The insert represent the interference between the initial electron wave emitted by absorbed atom and scattered wave resulting in the constructive (red) or destructive (blue) effect.

2.3 Electrical resistance and magnetoresistance measurement

To explore the electrical and magnetic properties of Cr doped boron carbide, the electrical resistance (I-V curves) and magnetoresistance were measured. The samples were provided by the group of Prof. Anthony Caruso.

The measured samples of Cr doped boron carbide thin film on SiO_2 substrate were made by boron carbide-Cr co-deposition using boron carbide and chromium targets as sputtering sources. The pattern of gold electrodes on SiO_2 substrate were made by photolithography before the co-deposition process. The electrical resistance

seen as current verse bias was obtained in room temperature by applying a bias from -3 V to +3 V and from + 3 V to -3 V with 0.05 V step. The I-V curve taken under 0 and 8000 Gauss magnetically field parallel to the current direction with an applied bias from -3 V to +3 V were compared.

The magnetoresistance effect is the change of electrical resistance in conductors or semiconductors on the application of magnetic field. The magnetoresistance measurement was obtained by measuring the electrical resistance when scanning the applied magnetic field. The percentage magnetoresistance is defined as $\frac{R_H - R_o}{R_H} \times 100\%$, where R_o and R_H are resistance in zero and applied magnetic field.

2.4 Mass spectrometry

The photoionization and photofragmenation mass spectrometry was performed to study the dehydrogenation in the *closo*-carboarnes by using synchrotron vacuum ultraviolet (VUV).The VUV mass spectrometry of hydrogen loss and molecular fragmentation was done at much lower photon energies, also with synchrotron radiation. The time of flight mass spectrometry at B 1s and C 1s threshold and triple coincidence mass spectrometry were performed to study the photoframentation of *closo*-carborane isomers. I analyzed these mass spectra measurements made by my collaborators [22-25].

2.4.1 Description of photoionization and photofragmentation processes

In the photoionization and photoframentation processes, the parent molecule is

promoted to an excited state after absorption of the photon. Then, the excited molecular species can fragment in a variety of decay processes [26,27]. In the photoionization process, a parent ion and its associated electron were produced when the photon energy is above the ionization energies (IE). In the photofragmentation process, the decay can result in one or more ion fragments, associated neutral fragments and electrons. Part of the photon energy is consumed for breaking bonds as well as ionization. The excess energy in the forms of kinetic energy and internal energy (including electronic energy, vibrational energy and rotational energy) are distributed among all the fragments.

The ionization energies (IE) were determined for *closo*-carboranes and *closo*-phosphacarboranes are about 10 eV [24]. Above the ionization threshold, the cation fragmentation occurs and the multiple fragmentation routes are also possible for the *closo*-carboranes [22,23], where possible one wants to measure the appearance potential of the fragment ions. In this work, this was not possible because of the low yields at the appearance potential (AP) threshold. At low photon energy range of 10-35 eV, hydrogen loss from the parent dominates the fragmentation process nonetheless [22]. During mass spectrometry experiments studying the photoionization and photoframentation of the gas phase *closo*-carboranes and *closo*-phosphacarboranes, the molecules were in thermal equilibrium at room temperature. As a plus, the borane and carborane species exhibit high thermal stability [28]. Thus, the thermal fragmentation is not significant in the related experiments.

2.4.2 Photoionization and photofragmentation using synchrotron vacuum ultraviolet (VUV)

As just noted, the gas phase photoionization and photodecomposition for the various isomers of *closo*-dicarbadodecaborane and *closo*-phospha-carbadodecaborane were investigated by photoionization mass spectrometry using synchrotron vacuum ultraviolet (VUV) radiation in the gas phase [24]. The monochromatic light was provided by a 3 m normal incidence monochromator (3 m NIM-1), at BESSY II, which was equipped by a 600 L/mm grating. For higher influences, undispersed VUV synchrotron radiation was used. Inserting a LiF cutoff filter allows us to measure mass spectra without higher order radiation or stray light. A quadrupole mass filter was used for photoion detection [29].

Because of the limited cation count rates, total flux was important for obtaining photoionization mass spectra with sufficient ion intensity. Photoionization mass spectra were taken in the range of 126 to 146 amu with zero order light from the normal incidence monochromator. The geometry of the normal incidence monochromator cuts off the zero order synchrotron white light at above about 35 eV. On the other hand, photo-fragmentation of the *closo*-carborane cation should occur at photon energies above the photoionization thresholds [22]. It is at these low energies of 10 to 35 eV that dehydrogenation is believed to dominate the fragmentation process [22].

2.4.3 Time of flight mass spectrometry

To investigate the ionic fragmentation processes of *closo*-carboranes, a time-of-flight (TOF) mass spectrometer was used [22]. The time-of-flight mass spectrometer consisted of a two stage acceleration region separated by grids, followed by a 30 cm drift tube. Wiley-McLaren focusing conditions were used [30,31]. A -250

V/cm extraction field was used for the ions. Under these conditions, splitting was generally not detected for any of the mass peaks, indicating there was negligible distortion of the yields due to loss of high kinetic energy ions. Note that isotopic and $Y\text{-}H_x$ distributions tend to blur any such effects, except for H^+ (fragment units are labeled Y_n^+, where Y^+ corresponds to BH^+ or CH^+). The overall efficiency for ion detection is estimated to be about 15%. The start of the flight time scale was the signal from an electron accelerated by a field of +250 V/cm (for experiments at the Advanced Light Source) or +300 V/cm (for experiments taken at BESSY-I) to a channelplate or a channeltron adjacent to the ionization region.

2.4.4 Triple coincidence mass spectrometry

The coincidence TOF mass spectrometry was performed to study the double cation fragmentation processes of *closo*-carboranes [25,29]. In the photoelectron-photoion-photoion coincidence (PEPIPICO) experiments, there are three particles, including two of the positive ions and one of the electrons from the charge separation, were detected. The detection of the electron provides a qualitative time zero from which the times of flight of each of the product ions through a drift tube can be measured. Photoelectron-photoion-photoion coincidence (PEPIPICO) spectra were acquired using a custom built multi-stop time-to-digital converter with a time resolution of 12 nsec. Soft X-rays from the undulator beamline 9.0.1 of the Advanced Light Source [32] and the HE-TGM-2 beamline at BESSY I [33] were used with almost identical electron and cation detection setups, yielding virtually identical results. In order to avoid excessive accidental coincidence events and to keep the overall event rates within the capacity of the processing system, rather narrow

entrance and exit slits were used, typically ~10 μm. The photon energy resolution was better than 0.1 eV FWHM at the ALS and <0.3 eV at BESSY-I.

We plot both flight times and estimated cation ion mass (in amu), as a matter of convenience, since the individual ion flight times are proportional to the square root of ion mass. The peak shapes of PIPICO spectra were usually affected by several factors, such as apparatus discrimination, the kinetic energy release distribution and the ion angular distribution [34,35]. The general peak shapes for two body dissociation are rectangular, narrow single peak and double peak structure [36]. The peak shapes in PEPIPICO can also provide the information about the mechanism of dissociation processes [23,37]. The double cation fragmentation reaction obeys the conservation law of the momentum so that the linear momenta are given to two fragments equal and opposite. Thus, the peak projection in the t_1-t_2 plane normally has slope of -1. For three body dissociation, the neutral could be ejected before charge separation (deferred charge separation) or after charge separation (secondary dissociation). The least likely way is that all fragments are generated at once (simultaneous Coulomb explosion). The slope of peak for deferred charge separation is -1, while the absolute value of secondary dissociation is the ratio of mass of the product to mass of its precursor.

References:

[1] S. Balaz, A. N. Caruso, N. P. Platt, D. I. Dimov, N. M. Boag, J. I. Brand, Ya. B. Losovyj, and P. A. Dowben, J. Phys. Chem. B **111**, 7009 (2007).

[2] D. W. Hess, Ann. Rev. Mater. Sci. **16**, 163 (1986); M. Meyyanppan, J. Phys. D: Appl. Phys. **42**, 213001 (2009).

[3] R. Hezel, and R. Schorner, J. Appl. Phys. **52**, 3076 (1981); A. G. Aberle, and R. Hezel, Prog. Photovoltaics **5**, 29 (1997); M. Shen, A. T. Belleds. Plasma Polymeriztion, ACS Symposium Series, Washington, DC: Am. Chem. Soc. **108**, 344 (1979).

[4] B. W. Robertson, S. Adenwalla, A. Harken, P. Welsch, J. I. Brand, P. A. Dowben, and J. P. Claassen, Appl. Phys. Lett. **80**, 3644 (2002).

[5] B. W. Robertson, S. Adenwalla, A. Harken, P. Welsch, J. I. Brand, J. P. Claassen, N. M. Boag, and P. A. Dowben, Advances in Neutron Scattering Instrumentation, Ed. I. S. Anderson, and B. Guérard, Proc. SPIE **4785**, 226 (2002).

[6] S. Adenwalla, R. Billa, J. I. Brand, E. Day, M. J. Diaz, A. Harken, A. McMullen-Gunn, R. Padmanabhan, and B. W. Robertson, Penetrating Radiation Systems and Applications V, Proc. SPIE **5199**, 70 (2003).

[7] C. Lundstedt, A. Harken, E. Day, B. W. Robertson, and S. Adenwalla, Nucl. Instrum. Methods in Phys. Res. A **562**, 380 (2006).

[8] S. Lee, J. Mazurowski, G. Ramseyer, and P. A. Dowben, J. Appl. Phys. **72**, 4925 (1992); S. Lee, and P. A. Dowben, Appl. Phys. A **58**, 223 (1994).

[9] S. Adenwalla, P. Welsch, A. Harken, J. I. Brand, A. Sezer, and B. W. Robertson, Appl. Phys. Lett. **79**, 4357 (2001).

[10] A. N. Caruso, R. B. Billa, S. Balaz, J. I. Brand, and P. A. Dowben, J. Phys. Cond. Matter **16**, L139 (2004).

[11] A. N. Caruso, P. A. Dowben, S. Balkir, N. Schemm, K. Osberg, R. W. Fairchild, O. Barrios Flores, S. Balaz, A. D. Harken, B. W. Robertson, and J. I. Brand, Mater. Sci. Engineering B **135**, 129 (2006).

[12] K. Osberg, N. Schemm, S. Balkir, J. I. Brand, S. Hallbeck, P. Dowben, and M. W. Hoffman, IEEE Sensors Journal **6,** 1531 (2006).

[13] S. Balaz, D. I. Dimov, N. M. Boag, K. Nelson, B. Montag, J. I. Brand, and P. A. Dowben, Appl. Phys. A **84**, 149 (2006).

[14] S.-D. Hwang, D. Byun, N. J. Ianno, P. A. Dowben, and H. R. Kim, Appl. Phys. Lett. **68**, 1495 (1996).

[15] J. J. Rehr, and R. C. Alberts, Rev. Mod. Phys. **72**, 621 (2000).

[16] P. A. Lee, P. H. Citrin, P. Eisenberger, and B. M. Kincai, Rev. Mod. Phys. **53**, 769 (1981).

[17] R. A. Scott, Methods in Enzymology, Enzyme Structure, Part J, Academic Press, Orlando, Florida, **117**, 114 (1985).

[18] U. Skyllberg, P. R. Bloom, J. Qian, C.-M. Lin, and W. F. Bleam, Environ. Sci. Technol. **40**, 4174 (2006); P. D'Angelo, A. Lapi,. V. Migliorati, A. Arcovito,| M. Benfatto, O. M. Roscioni, W. Meyer-Klaucke, and S. Della-Longa., Inorg. Chem. **47**, 9905 (2008).

[19] P. S. Lysaght, J. C. Woicik, M. A. Sahiner, S.-H. Lee, R. Jammy, Appl. Phys. Lett. **91**, 1122910 (2007); T. Yamamoto, Y. Kawashima, Y. Kusakabe, S. Matsuda, Y. Mizukoka, Y. Nakade, and T. Okajima, J. Phys.: Condens. Matter, **21**, 104211 (2009).

[20] http://camd.lsu.edu/pdf/Rose_Final_06-19-2009.pdf (CAMD 2009 annual report)

[21] I. Tanaka, and T. Mizoguchi, J. Phys.: Condens. Matter **21**, 104201 (2009).

[22] D. Feng, J. Liu, A. P. Hitchcock, A. L. D. Kilcoyne, T. Tyliszczak, N. Riehs, E. Ruhl, J. D. Bozek, D. McIlroy, and P. A. Dowben, J. Phys. Chem. A **112**, 3311 (2008).

[23] E. Rühl, A. P. Hitchcock, J. D. Bozek, T. Tyliszczak, A. L. D. Kilcoyne, D. N.McIlroy, A. Knop-Gericke, and P. A. Dowben, Physica Status Solidi B **246**, 1496 (2009).

[24] E. Ruhl, N. F. Riehs, S. Behera, J. Wilks, J. Liu, H.-W. Jochims, A. N. Caruso, N. Boag, J. A. Kelber, and P. A. Dowben, J. Phys. Chem. A **114**, 7284 (2010).

[25] J. Liu, E. Rühl, A. P. Hitchcock, D. N. McIlroy, J. D. Bozek, A. L. David Kilcoyne, T. Tyliszczak, A. Knop-Gericke, N. M. Boag and P. A. Dowben, "Photo-fragmentation of the *closo*-Carboranes Part III: Double Cation Fragmentation", in preparation.

[26] R. Schinke, Photodissociation Dynamics: Spectroscopy and Fragmentation of small polyatomic molecules, (Cambridge University Press, Cambridge 1993).

[27] H. Lefebvre-Brion and R.W. Field, Perturbations in the Spectra of Diatomic Molecules,(Academic Press, Orlando, 1986).

[28] J. Plešek, Chem. Rev. **92,** 269 (1992).

[29] M. Schwell, F. Dulieu, C. Gee, H.-W. Jochims, J. L. Chotin, H. Baumgärtel, and S. Leach, Chem. Phys. **260**, 261 (2000); F. Gaie-Levrel1, C. Gutlé, H.-W. Jochims, E. Rühl, and , M. J. Schwell, Phys. Chem. **112**, 5138 (2008).

[30] C. W. Wiley, and I. H. McLaren Rev. Sci Instrum. **26**, 1150 (1955).

[31] E. Rühl, C. Schmale, H. W. Jochims, E. Biller, M. Simon, and Baumgärtel, H. J. Chem. Phys. **95**, 6544 (1991).

[32] B. Langer, N. Berrah, A. Farhat, O. Hemmers, and J. D. Bozek, Phys. Rev. A **53**, R1946 (1996).

[33] S. Bernstorff, W. Braun, M. Mast, W. Peatman, and T. Schroeter, Rev. Sci. Instrum. **60**, 2097 (1989).

[34] R. Lablanquie, I. Nenner, P. Millie, P. Morin, J. H. D. Eland, M. J. Hubin-Franskin, and J. Delwiche, J. Chem. Phys. **82**, 2951 (1985).

[35] J. H. D. Eland, Vaccum Ultraviolet Photoionization andPphotodissociation of Molecules and Clusters, Ed. C. Y. Ng, (World Scientific: Singapore, P297, 1991).

[36] A. Lindgren, Studies of Molecular and Cluster Fragmentation Using Synchrotron Radiation: Measurements and Models. Ph.D. thesis, Lund Universtity, United Kingdom, October 2006.

[37] J. H. D. Eland, Acc. Chem. Res., **22**, 381 (1989); J. H. D. Eland, Laser Chem. **11**, 259 (1991).

Chapter 3 Theoretical methodologies

3.1 Theory of XANES and EXAFS

The X-ray absorption is a transition between the core level electrons in absorbing atom to the free or unoccupied continuum levels. The photoelectron can be scattered from the electrons of the neighboring atoms and interfere with absorbing atom. The absorption coefficient will be altered by the effects of the scattered back photoelectron [1-5].

The normalized XAFS spectrum $\chi(E)$ is defined as

$$\chi(E) = [\mu(E) - \mu_o(E)]/\Delta\mu_o \tag{1}$$

where $\mu(E)$ is the absorption coefficient, $\mu_o(E)$ is a smooth background function and $\Delta\mu_o$ is the normalization factor which is often approximated by the magnitude of the jump in absorption at the edge.

The physical description of the absorption coefficient $\mu(E)$ from Fermi's Golden rule is

$$\mu(E) \propto \sum_{f}^{E_f > E_c} \left|\langle f|H|i\rangle\right|^2 \delta(E_f - E_i - E) \tag{2}$$

where $|i\rangle$ is the initial state with an a core electron. $\langle f|$ is the final state in the presence of core hole. H is the interaction Hamiltonian.

With the dipole approximation, the absorption coefficient is given by

$$\mu(E) \propto \sum_{f}^{E_f > E_c} \left|\langle f|\hat{\varepsilon}\cdot\vec{r}|i\rangle\right|^2 \delta(E_f - E_i - E) \tag{3}$$

where $\hat{\varepsilon}$ is the X-ray polarization vector.

In the multiple-scattering theory, X-ray absorption fine structure is interpreted as the sum over multiple-scattering paths. Thus, $\mu(E)$ can be expressed in terms of a multiple-scattering path expansion of the full propagator *G* [6], which is rewritten as

$$\mu(E) \propto -\frac{1}{\pi}\,\mathrm{Im}\langle i|\hat{\varepsilon}^* \cdot rG(r,r';E)\hat{\varepsilon}\cdot r|i\rangle\Theta(E-E_F) \qquad (4)$$

Where *G* is Green's function describing all possible ways for a photoelectron to interact with the surrounding atoms. E_F is the Fermi energy, Θ is a broadened step function at the Fermi energy.

Using the separable representation of Green's-function propagators,

$$G = G^0 + G^0tG^0 + G^0tG^0tG^0 + \cdots\cdots. \qquad (5)$$

Here G^0 is free propagator, t is scattering matrices.

Then the problem is separated into single scatter at the absorption site (G^c) and remaining scatters (G^{sc}), which are treated in perturbation theory, i.e. $G = G^c + G^{sc}$.

Thus, the X-ray absorption coefficient can be expressed as

$$\mu(E) = \mu_o(E)(1+\chi(E)) \qquad (6)$$

For XANES region, $\mu_o(E)$ is a rapidly changing function with features comparable with $\chi(E)$, so currently the XANES is hard to analyze quantitatively and precisely. In EXAFS region, however, $\mu_o(E)$ is a smooth background function and can be constructed in a better manner to analyze the EXAFS quantitatively. More details about calculate the Green's function could be obtained from Ref 1-3 and 6.

The quantitative expression of normalized EXAFS as function of wave vector $k = \frac{2m}{\hbar}\sqrt{\hbar w - |E_o|}$ is given by [7]

$$\chi(k) = \sum_j \frac{S_o^2 N_j |f_j(k)|}{kR_j} \sin(2kR_j + \delta_j(k)) e^{-2R_j/\lambda_j} e^{-2k^2\sigma_j^2} \quad (7)$$

there R_j is interatomic distance, N_j is the coordination number, $f_j(k) = |f_j(k)| e^{i\Phi(k)}$ is the scattering amplitude. The amplitude reduction term S_o^2 accounts for the many-body effects. This value is usually between 0.7 and 1.0. The factor $\delta_j(k)$ is the result of the central-atom partial-wave phase. The factors $\delta_j(k)$ and the scattering amplitude $f_j(k)$ depend on atomic number of the neighboring atom. λ_j is energy-dependent XAFS mean free path. σ_j is the root-mean-square fluctuation in bond length which contains the information of structural disorder.

The FEFF codes, named after the fast Fourier transform of the effective scattering amplitude, is a series of program for *ab initio* multiple scattering calculations of EXAFS [1-4]. For the theoretical calculation, with input the coordinates of atoms and information of absorbing atom, the phase shift δ_j, scattering amplitude $f_j(k)$ and mean-free path λ_j can be calculated for a particular scattering shell or scattering paths for the cluster of atoms [8]. Then, other parameters in the EXAFS equation could be predicted and refined to get the best fit of measured data $\chi(k)$ or the Fourier transformed data in R-space. The theoretical calculation of XANES has been a challenging problem. A self-consistent real-space multiple-scattering (RSMS) approach was presented and implemented in *ab initio* FEFF8 code to interpret the XANES [9].

The EXAFS data of Fe, Mn doped semiconducting boron carbide samples were analyzed and fitted by FEFF6 codes program. The fitting Fourier transformed EXAFS

$k\chi(k)$ data, in radial coordinates, were obtained for Mn and Fe doped boron carbide within 6 Å.

3.2 Density functional theory (DFT)

The density functional theory (DFT) has been developed to simulate the properties of a wide range of materials. Unlike other *ab initio* methods, the density functional theory describes the system using the charge density instead of the wavefunction. The very first discussion of density functional theory could be traced back to 1964 paper by Hohenberg and Kohn [10,11]. They proposed that the ground state energy E is a functional of charge density ρ. The fundamental statement of DFT is

$$\delta\{E(\rho)-\mu(\mathrm{N}(\rho)-\mathrm{N})\}=0. \tag{8}$$

Here $E(\rho)$ is the ground state energy functional and $E(\rho)=V_{ext}(\rho)+F(\rho)$, where functional $V_{ext}(\rho)$ is external potential, $F(\rho)$ includes two terms-the kinetic energy $T(\rho)$ and electron-electron correlation energy $V_{ee}(\rho)$. μ is chemical potential, N is the number of particles in the system and $\mathrm{N}(\rho)=\int\rho(\mathbf{r})d\mathbf{r}$.

Later, Kohn and Sham [10,12] introduced an exchange-correlation functional to approximate the kinetic and electron-electron functionals. Their theory assumes a non-interacting system with a single determinant wavefunction ϕ_i. The kinetic energy is defined as

$$T_{s(\rho)}=-\frac{1}{2}\sum_{i}^{\mathrm{N}}\langle\phi_i|\frac{\hbar^2\nabla^2}{2m}|\phi_i\rangle \tag{9}$$

where the ground state charge density $\rho(\mathbf{r}) = \sum_{i}^{N} \left| \phi_i^2 \right|$, and the electron-electron interaction becomes the Coulomb interaction (electrostatic interaction). The ground state energy can be written as

$$E(\rho) = T_s(\rho) + V_{ext}(\rho) + V_{coulomb}(\rho) + E_{xc}(\rho) \tag{10}$$

where $E_{xc}(\rho)$ is the exchange–correlation functional

$$E_{xc}(\rho) = (T(\rho) - T_s(\rho)) + (V_{ee}(\rho) - V_{coulomb}(\rho)). \tag{11}$$

By minimizing the total energy with respect to ϕ_i, it was found that ϕ_i is the eigenstate of a single Hamiltonian called Kohn-Sham Hamiltonian H_{KS}.

$$H_{KS}\phi_k = \varepsilon_i \phi_i \tag{12}$$

$$H_{KS} = -\frac{\hbar^2 \nabla^2}{2m} + v_{ext} + v_{coulomb} + v_{xc} \tag{13}$$

where $v_{xc} = \frac{\delta E_{xc}(\rho)}{\delta \rho}$ is exchange-correlation potential.

Thus, this approach should obtain many of properties of the many-body system by considering the non-interacting system in an effective local potential (exchange-correlation potential). For the exact functional and then the exact local potential, the ground state charge density and energy must be obtained (only approximately known).

The exchange-correlation functional, a crucial part of density functional theory, is only approximately known. There have been many efforts to find good approximations for the exchange-correlation functional to solve the many-body system problems more correctly. The most popular approximations include local

density approximation (LDA) [13], generalized gradient approximation (GGA) [14] and hybrid exchange functionals [15]. The idea of LDA is to approximate the exchange-correlation functional solely as a simple function of the local charge density at each point in a uniform electron gas density ρ. The LDA has been used fairly successfully to obtain reliable results for many systems with relatively low computational cost. However, LDA gives less accurate minimum energy geometries and binding energies. The addition of GGA is to adopt an energy functional that depends on density and its gradients at considered point. Although the functional is still local, GGA usually gives more accurate geometry and improved total energy. The hybrid functionals are widely used in computational chemistry, and the B3LYP functional remains one of the most common. The hybrid functional is a combination of LDA (with estimates of the GGA corrections) and Hartree-Fock (HF) methodologies, which should give more reliable geometry and binding energy than GGA alone in molecular systems.

3.3 Theoretical approach

The DFT hybrid functional (DFT-B3LYP) with standard 6-31 G* basis set and the Perdew-Wang 91 exchange correlation potential were used to calculate the ground-state energies for three isomers of *closo*-carborane as well as the fragments to construct the energetics for the photoframentation processes, which has been proved to be a successful approach for modeling *closo*-carborane decomposition [11,16,17].

In all cases, all possible inequivalent ion pairs, fragments and the different molecular structures with the same mass were considered. In modeling each dissociation pathway related to the reactions evident from experiment, all symmetrically non-equivalent appropriate carbon and boron atom combinations from within the *closo*-carborane were considered. We report here the fragmentation energies as those with the minimum energy cost.

Parent ion loss of H and H_2 was investigated and the energetics of neutral and cation parent ion formation with and without loss of hydrogen was calculated [16]. The energetics of cation fragmentation with fragments larger than just hydrogen has been also investigated. In fact the ground-state energies for a variety of carborane clusters were also calculated by the semiempirical method PM3 as comparison to the results from DFT calculation [17]. Both the semiempirical and *ab initio* calculations were geometry optimized to obtain the lowest unrestricted Hartree-Fock (UHF) energy states. The ground-state geometries of these carborane clusters were optimized using energy minimization with semiempirical method PM3 before the DFT calculations to save on computational time. Although not a dominant fragmentation process, dication fragmentation was also investigated. Estimates of the energetics for the molecular dication decomposition processes were also carried out by density functional theory using the standard hybrid functional B3LYP with 6-31G* basis. The energies of three major ion pairs species including H^+ and BH_2^+/CH^+ ion pairs, BH_2^+/CH^+ and Y_{11}^+ ion pair, Y_3^+ and Y_9^+ ion pairs (where Y = (BH) or (CH)) were

constructed for three isomers 1,2-, 1,7- and 1,12-$C_2B_{10}H_{12}$.

Both semi-empirical by PM3 and density functional theory were used to get the structural coordinates of Fe and Mn doped semiconducting boron carbide for the extended X-ray absorption fine structure spectroscopy (EXAFS) data fitting. This time, the DFT calculations [18,19] were performed with PW91 now with the generalized gradient approximation (GGA) included. All the electrons were considered equally, and the double numerical plus polarization (DNP) basis set, which is comparable to the 6-31G** basis set, was used. The convergence tolerance for the self-consistent field is 2.72×10^{-6} eV, and the structures were optimized till the maximum force is below 0.054 eV/Å.

Reference:

[1] J. J. Rehr and R. C. Albers, Rev. Mod. Phys. **72**, 621 (2000)

[2] J. J. Rehr, J. Mustre de Leon, S.I. Zabinsky and R. C. Albers, J. Am. Chem. Soc. **113**, 5135 (1991)

[3] S. I. Zabinsky, J. J. Rehr, A. Ankudinov, R. C. Albers and M. J. Eller, Phys. Rev. B **53**, 2995 (1995).

[4] P. A. Lee, P. H. Citrin, P. Eisenberger and B. M. Kincard, Rev. Mod. Phys. **53**, 769 (1981).

[5] M. Newville, Fundamentals of XAFS, (Jul. 2004). Available at http://xafs.org/Tutorials?action=AttachFile&do=view&target=Newville_xas_fundamentals.pdf

[6] P. A. Lee and J. B. Pendry, Phys. Rev. B **11**, 2795 (1975).

[7] D. E. Sayers, E. A. Stern and F. W. Lytle, Phys. Rev. Lett. **27**, 1204 (1971).

[8] Details of the FEFF program, http://leonardo.phys.washington.edu/feff/

[9] A. L. Ankudinov, B. Ravel, J. J. Rehr, S. D. Conradson, Phys. Rev. B **58**, 7565 (1998).

[10] W. Kohn and L. J. Sham, Phys. Rev. A **140**, 1133 (1965).

[11] P. Hohenberg and W. Kohn, Phys. Rev. B **136,** 864 (1964).

[12] R. G. Parr, Ann. Rev. Phys. Chem. **34**, 631(1983); N. M. Harrison, Computational Materials Science, Ed. C. R. A. Catlow and E. A. Kotomin (IOS press, Amsterdam, 2003).

[13] R. G. Parr, W. Yang, Density-Functional Theory of Atoms and Molecules, (Oxford: Oxford University Press, London, 1994).

[14] J. P. Perdew and Y. Wang, Phys. Rev. B **33**, 8800, (1986); Ibid. E **34**, 7406, (1986); J. P. Perdew, in Electronic Structure of Solids 91, Ed. P. Ziesche and H. Eschrig (Akademie Verlay, Berlin, 1991

[15] D. Becke, J. Chem. Phys., **98**, 1372 (1993); A.D. Becke, Ibid. **98,** 5648 (1993).

[16] E. Ruhl, N. F. Riehs, Swayambhu Behera, J. Wilks, J. Liu, H.-W. Jochims, A. N. Caruso, N. Boag, J. A. Kelber, and P. A. Dowben, J. Phys. Chem. A, **114**, 7284 (2010).

[17] D. Feng, J. Liu, A. P. Hitchcock, A. L. D. Kilcoyne, T. Tyliszczak, N. Riehs, Ruhl, E.; Bozek, J. D.; McIlroy, D.; Dowben, P. A. J. Phys.Chem. A, **112**, 3311 (2008).

[18] J. Liu, G. Luo, W-N Mei, O. Kizilkaya,E. D. Shepherd, J. I. Brand and P. A. Dowben *J. Phys. D: Appl. Phys.* **43**, 085403 (2010).

[19] G. Luo, J. Lu, J. Liu, W-N Mei, and P.A. Dowben *Materials Science and Engineering B* **175,** 1 (2010).

Chapter 4 Chemistry of *closo*-carborane: photofragmetation of *closo*-carboranes

The study of photofragmentation processes for *closo*-carborane is one part of the efforts to understand the growth and chemistry of the semiconducting boron carbides of approximate stoichiometry "$C_2B_{10}H_x$" (where x represents up to 40 at% fraction of hydrogen) [1]. This is important in material physics as the *closo*-1,2-orthocarborane is presently the main precursor source molecule to fabricate the semiconducting boron carbide thin films via plasma enhanced chemical vapor deposition (PECVD). The hydrogen content in resulting boron carbide and previous cluster calculations [2] suggest that the decomposition of *closo*-carboranes to form the "$C_2B_{10}H_x$" does not result in complete fragmentation of the icosahedral cage, but regrettably little is known about the detailed decomposition mechanisms of the *closo*-carboranes [2].

The chemistry of dehydrogenation processes of both the *closo*-carboranes and related *closo*-phosphacarboranes (shown in Figure 4.1) were investigated by photoionization mass spectrometry studies [3]. The ionic photofragemetation of three isomers of *closo*-carboranes in the region of B 1s and C 1s cores threshold have been also studied by time of flight (TOF) mass spectroscopy in order to understand the mechanisms of the single ion fragmentation processes [4]. Thermodynamic cycles are constructed by theoretical modeling as well for neutral and ionic species in an attempt to systemically characterize the single ion fragmentation processes. The studies of

double cation pair production of *closo*-carborane at or above B1 s and C 1s threshold were carried out by photoion-photoion coincidence (PIPICO) and photoelectron-photoion-photoion coincidence (PEPIPICO) mass spectra measurements. The energetics of neutral hydrogen, di-hydrogen and related possible fragments from the parent cation and neutral molecules, ionization potentials, cation fragmentation and double cation fragmentation were studied. In later case, three ion pairs species, H^+ and BH_2^+/CH^+, BH_2^+/CH^+ and Y_{11}^+ ion pairs (where Y = (BH) or (CH)), Y_3^+ and Y_9^+ (where Y = (BH) or (CH)) ion pairs, are constructed for comparison [5].

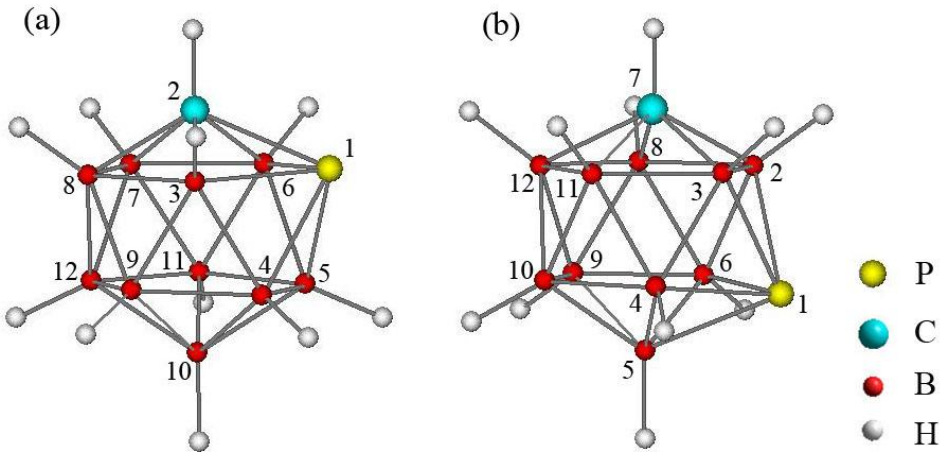

Figure 4.1. Schematic representations of phosphacarboranes: (a) *ortho*-1-phospha-2-carbadodecaborane ($1,2\text{-}PCB_{10}H_{11}$) and (b) *meta*-1-phospha-7-carbadodecaborane ($1,7\text{-}PCB_{10}H_{11}$)

4.1 Vacuum ultraviolet (VUV) assisted dehydrogenation in the *closo*-carboranes and semiconducting $C_2B_{10}H_x$ films

4.1.1 The *closo*-carborane dehydronation in the near VUV

The observed dehydrogenation for the various isomers of *closo*-dicarbadodecaborane and *closo*-phospha-carbadodecaborane were investigated by photoionization mass spectrometry using synchrotron vacuum ultraviolet (VUV) radiation in the gas phase. The geometry of the normal incidence monochromator cuts off the zero order synchrotron light at above about 35 eV, as stated in chapter 2. It is at these low energies of 10 to 35 eV that dehydrogenation is believed to dominate the fragmentation process [6].

Because of the multiplicity of boron atoms [6], the existence of multiple isotopes even at relative abundance of ^{10}B (19.8%) and ^{11}B (80.2%), will lead to a multiplicity of parent ion masses, as seen in Figure 4.2. Any photoionization mass spectroscopy geared towards identifying dehydrogenation must take into account the natural isotopic abundance of boron (^{10}B and ^{11}B) and carbon, and how this lead to a multiplicity of parent ion masses. Analysis of the parent ion mass spectrum was done using the procedures applied to other polyatomic clusters with a natural multiple isotope distribution [7]. Even with careful consideration of the isotopic abundances of the main group elements, the distribution of masses in the parent ion region of the photoionization mass spectrum tend towards smaller masses than expected for the

three different isomers of *closo*-dicarbadodecaborane, if no loss of hydrogen is present. This is illustrated in Figure 4.2 and Figure 4.3 for orthocarborane (1,2-$C_2B_{10}H_{12}$), metacarborane (1,7-$C_2B_{10}H_{12}$), and paracarborane (1,12-$C_2B_{10}H_{12}$).

Similarly, for the two related icosahedral cage molecules, 1-phospha-2-carbadodecaborane (1,2-$PCB_{10}H_{11}$) and 1-phospha-7-carbadodecaborane (1,7-$PCB_{10}H_{11}$), the distribution of parent molecule cation masses, from VUV photoionization, tends towards smaller masses than expected for ionization without loss of hydrogen, as seen in Figure 4.4. These observed smaller masses for the parent cations resulting from VUV photoionization are the result of hydrogen loss.

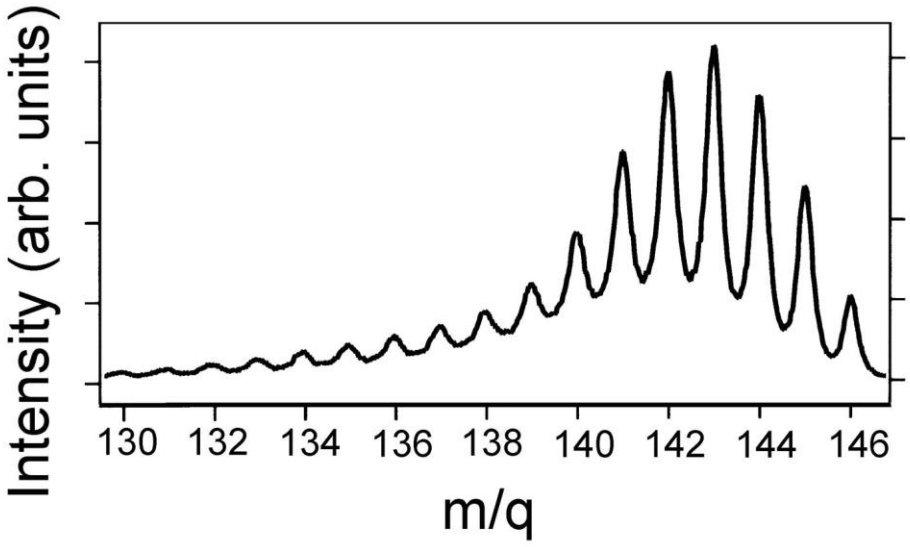

Figure 4.2. The part ion mass spectrum of closo-meta 1,7-dicarbadodecaborane in the region of 126 to 146 m/q. Photoionization was done with zero order light cut off at 35 eV by the geometry of the beamline (see text). Multiple mass peaks are seen as the result of hydrogen loss and the statistical distribution of the natural abundance of the ^{10}B and ^{11}B isotopes of boron.

The experimental photoionization mass distribution requires corrections for both hydrogen loss, and the boron and carbon isotopic abundance, as shown in Figures 4.3 and 4. We find that the photo-fragmentation of the parent cation, in the VUV, results in the loss of an even number of hydrogen atoms. This likely corresponds to the formation of H_2. The formation of H_2 from 2 H can release about 4.56 eV energy [8], so the formation of H_2 is energetically favored. In addition, H_2 is more stable than 2 H atoms because the diatomic hydrogen molecule has lower total energy by forming the covalent bond. Note that the neutrals cannot be directly measured in the present experimental setup, so we cannot provide much information about neutrals formed, from the data available to us. The hydrogen loss from the parent cation is evident and can be estimated, as shown in Figure 4.5a for orthocarborane (1,2-$C_2B_{10}H_{12}$), metacarborane (1,7-$C_2B_{10}H_{12}$), and paracarborane (1,12-$C_2B_{10}H_{12}$), and in Figure 4.5b, for the two related icosahedral cage molecules, 1-phospha-2-carbadodecaborane (1,2-$PCB_{10}H_{11}$) and 1-phospha-7-carbadodecaborane (1,7-$PCB_{10}H_{11}$). This hydrogen loss is apparently largely H_2, and almost completely even multiples of molecular hydrogen (Figure 4.5). We conclude that for energetic reasons dehydrogenation of the parent *closo*-carborane cations is dominated by H_2 loss.

Regrettably, photoionization mass spectroscopy does not identify which hydrogens are preferentially lost, and we must resort to theory and the solid state for guidance. Nonetheless, the favored loss of H_2 from adjacent sites should tend to lead

toward the formation of edge bonded icosahedra [9] in the solid state, and this surmise is certainly consistent with recent local structural information [10], as discussed in detail in chapter 5.

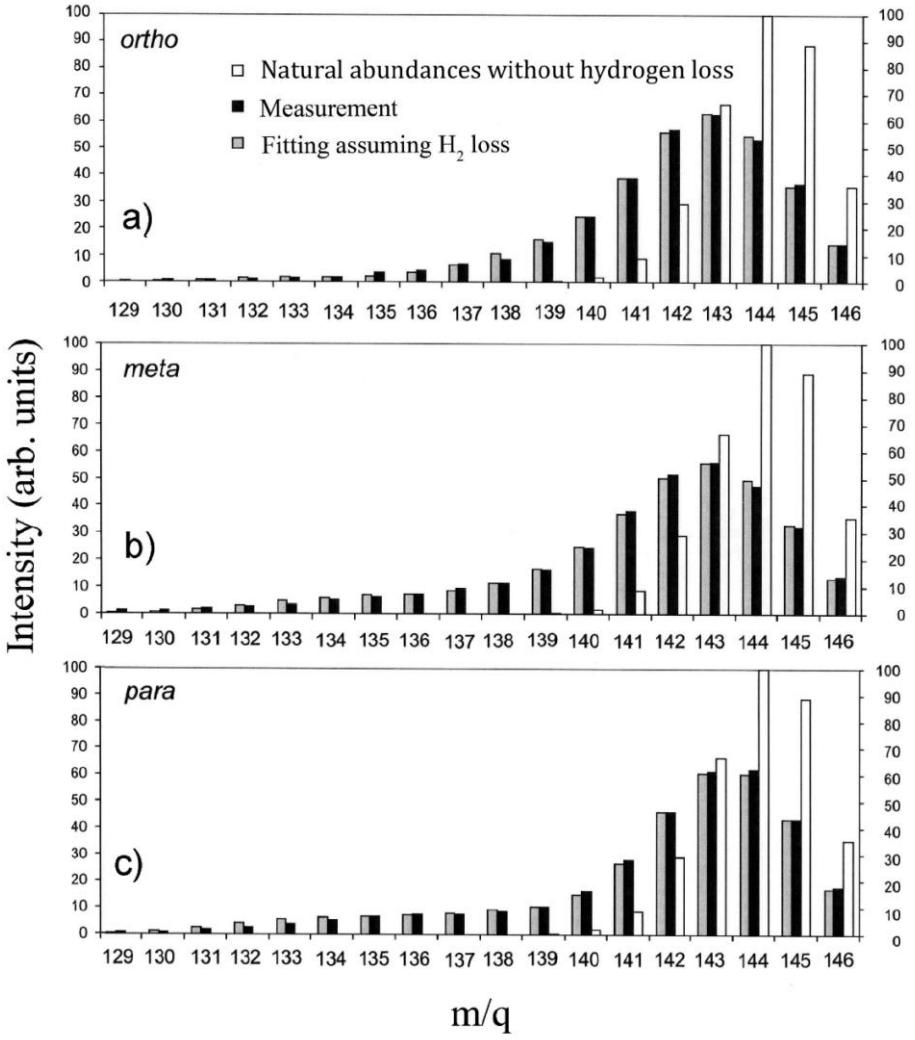

Figure 4.3. The predicted parent cation mass distribution, with boron and carbon isotopic abundance considered, compared to the photoionization experiment for three different isomers of *closo*-dicarbadodecaborane: (a) orthocarborane (1,2-$C_2B_{10}H_{12}$), (b) metacarborane (1,7-$C_2B_{10}H_{12}$), and (c) paracarborane (1,12-$C_2B_{10}H_{12}$). There is good agreement with the experimental data if there are corrections made to the parent ion

mass distribution for both hydrogen loss, and the boron and carbon isotopic abundance, as shown.

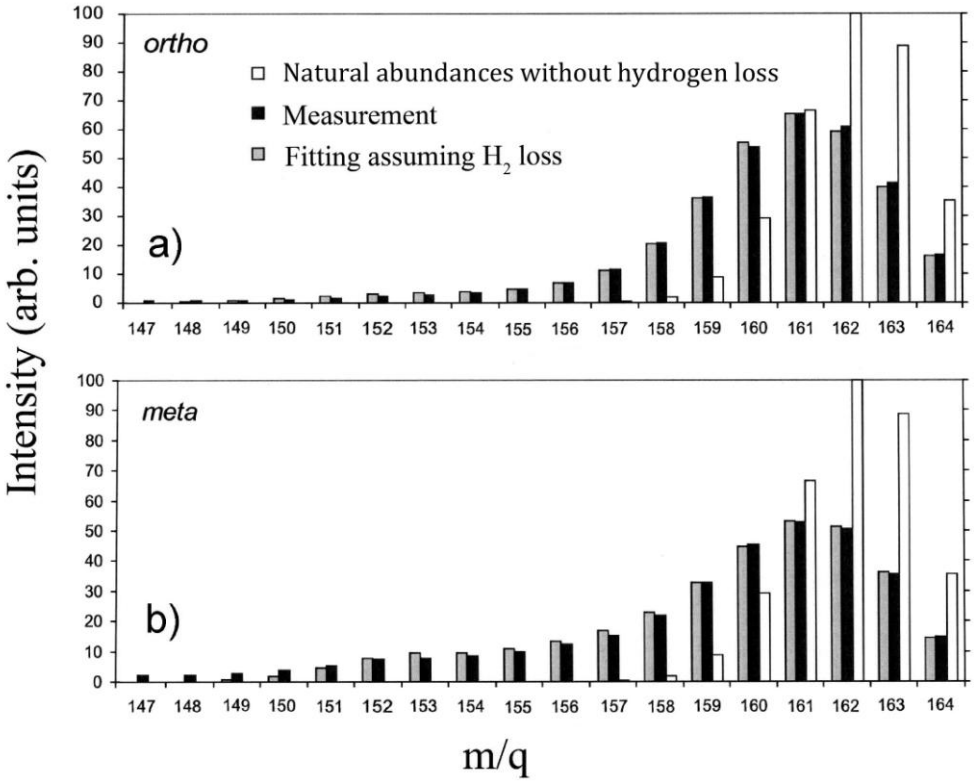

Figure 4.4. The predicted parent cation mass distribution, with boron, carbon and phosphorus isotopic abundance considered, compared to the photoionization experiment for (a) ortho-1-phospha-2-carbadodecaborane (1,2-$PCB_{10}H_{11}$) and (b) meta-1-phospha-7-carbadodecaborane (1,7-$PCB_{10}H_{11}$). There is again good agreement with the experimental data if there are corrections made to the parent ion mass distribution for both hydrogen loss, and the boron and carbon isotopic abundance, as shown.

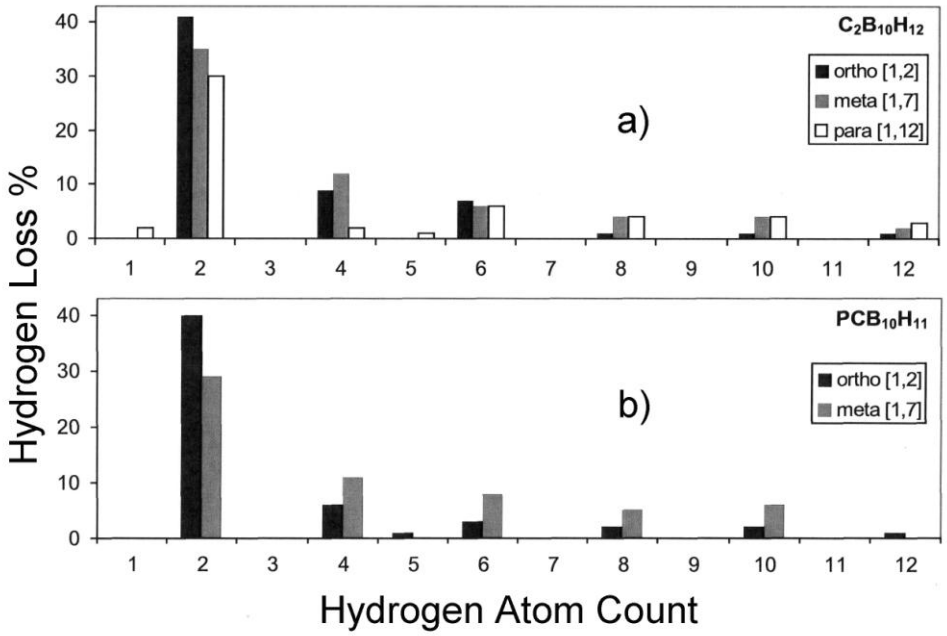

Figure 4.5. The loss of hydrogen from the parent cation for (a) the three different isomers of *closo*-dicarbadodecaborane (i.e. orthocarborane (1,2-$C_2B_{10}H_{12}$), metacarborane (1,7-$C_2B_{10}H_{12}$), and paracarborane (1,12-$C_2B_{10}H_{12}$)) and (b) two isomers of the *closo*-phosphacarborane (ortho-1-phospha-2-carbadodecaborane (1,2-$PCB_{10}H_{11}$) and (b) meta-1-phospha-7-carbadodecaborane (1,7-$PCB_{10}H_{11}$)), as determined from the photoionization mass spectra of Figures 4.3 and 4.4.

4.1.2 Modeling of the dehydrogenation

We have calculated all the symmetrically unique pairwise combinations for di-hydrogen (H_2) loss from the parent cation for the three different isomers of *closo*-dicarbadodecaborane: (a) orthocarborane (1,2-$C_2B_{10}H_{12}$), (b) metacarborane

(1,7-$C_2B_{10}H_{12}$), and (c) paracarborane (1,12-$C_2B_{10}H_{12}$), and (d) ortho-1-phospha-2-carbadodecaborane (1,2-$PCB_{10}H_{11}$) and (e) meta-1-phospha-7-carbadodecaborane (1,7-$PCB_{10}H_{11}$), by the means of DFT as stated in Chapter 3. This is summarized in Figure 4.6, using the number notation schemes of Figure 4.1 for the various *closo*-carboranes. In all cases, the reaction:

$$B_{10}C_2H_{12} \rightarrow B_{10}C_2H_{10}^{+} + H_2 + e^{-} \quad (1)$$

favors loss of adjacent hydrogen atoms farthest away from the carbon atoms or farthest away from the carbon and phosphorus (Figure 4.6). The range of bond dissociation energies possible in reaction (1) is greatest with hydrogen atom loss from orthocarborane (1,2-$C_2B_{10}H_{12}$) (roughly 11.5 to 14.5 eV or a range of energies covering 3 eV) and least with ortho-1-phospha-2-carbadodecaborane (1,2-$PCB_{10}H_{11}$) and meta-1-phospha-7-carbadodecaborane (1,7-$PCB_{10}H_{11}$) (11.8 to 13.5 eV or 10.8 to 12.8 eV respectively, or a range of energies 2 eV or less), as summarized in Figure 4.6. Except for ortho-1-phospha-2-carbadodecaborane (1,2-$PCB_{10}H_{11}$), the fraction of di-hydrogen (H_2) loss from the parent cation follows the trend of the calculated energetics. In the case of ortho-1-phospha-2-carbadodecaborane (1,2-$PCB_{10}H_{11}$), the energy range of symmetrically different pair combination of H_2, varies only over a small range of less than 2 eV (11.8 to 13.5 eV), but the fraction of H_2 loss relative to other even and odd numbers of hydrogen loss (40%) is larger than seen for

meta-1-phospha-7-carbadodecaborane (1,7-$PCB_{10}H_{11}$), metacarborane (1,7-$C_2B_{10}H_{12}$), and paracarborane (1,12-$C_2B_{10}H_{12}$), as illustrated in Figure 4.5.

As summarized in the plots of the energetics of pairwise loss of hydrogen (Figure 4.6), the loss of hydrogen from boron atoms is always favored over the loss of a hydrogen from a carbon atom. Indirectly, this boron dehydrogenation is substantiated by the propensity for most boron-rich solids whose majority carriers are holes, i.e. there is an introduction of acceptor states into the growing solid semiconductor.

The hydrogen loss occurs on the boron atoms with the smallest excess electron populations (0.01e to 0.15e) and farthest away from the carbons with an excess electron charge of roughly 0.31e, determined using Mulliken method, as summarized in Figure 4.7. It is not, however, related to the overall dipole that ranges from 4.42 D for *ortho*-carborane, 3.55 D for *ortho*-phosphacarborane, 2.79 D for *meta*-carborane, 2.24 D for *meta*-phosphacarborane, and 0 D for *para*-carborane [11].

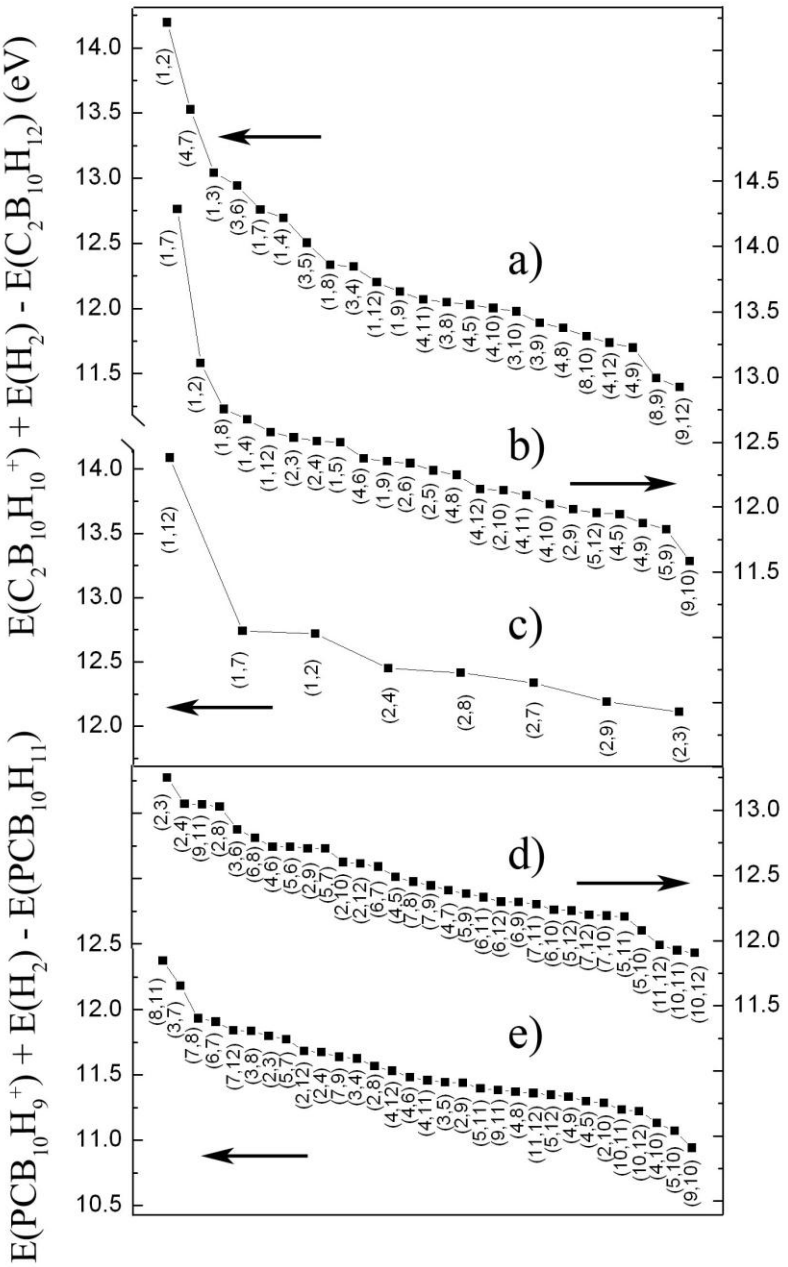

Figure 4.6. The energy cost for the loss of di-hydrogen from the parent cation for the three different isomers of *closo*-dicarbadodecaborane: (a) orthocarborane (1,2-$C_2B_{10}H_{12}$), (b) metacarborane (1,7-$C_2B_{10}H_{12}$), and (c) paracarborane (1,12-$C_2B_{10}H_{12}$), and (d) ortho-1-phospha-2-carbadodecaborane (1,2-$PCB_{10}H_{11}$) and (e) meta-1-phospha-7-carbadodecaborane (1,7-$PCB_{10}H_{11}$), calculated using calculated

using the hybrid density function theory (B3LYP), as discussed previously. These pairwise hydrogen atom loss energies are in eV and indexed according to the icosahedral site according to the numbering schemes shown in Figures 2.1 and 4.1. Not all pair combinations are plotted: some hydrogen pair combinations, identical by symmetry considerations, are not shown.

Although direct confirmation of the favored site for hydrogen loss is not available from the data we have presently in hand, some experimental support for our contention is available from studies the heavily hydrogenated boron carbide semiconducting films "$C_2B_{10}H_x$" which has been done by my collaborators [3]. There is a significant variation in the hydrogen content of semiconducting "$C_2B_{10}H_x$" boron carbide films fabricated by PECVD using orthocarborane as a precursor [1,12]. Loss of hydrogen leads to film densification, but overall, such semiconducting "$C_2B_{10}H_x$" boron carbide films have a much smaller band gap of 0.7 to 1.5 eV [13-16] than the free or adsorbed molecular highest occupied molecular orbital (HOMO) to lowest unoccupied molecular orbital (LUMO) of 9 eV to 11.3 eV for the *closo*-dicarbadodecaboranes and 7.8 to 9.5 eV for the *closo*-phospha-carbadodecaboranes [11,13,17]. Consequently far less than 10 eV photon energy, the lower limit of the photoionzation threshold in the gas phase is needed for photoionization of the icosahedra in the semiconducting "$C_2B_{10}H_x$" boron carbide film. Indeed we find that the Xe line, with a photon energy of 8.4 eV, is

adequate for photoemission/photoionization of the inorganic solid state films.

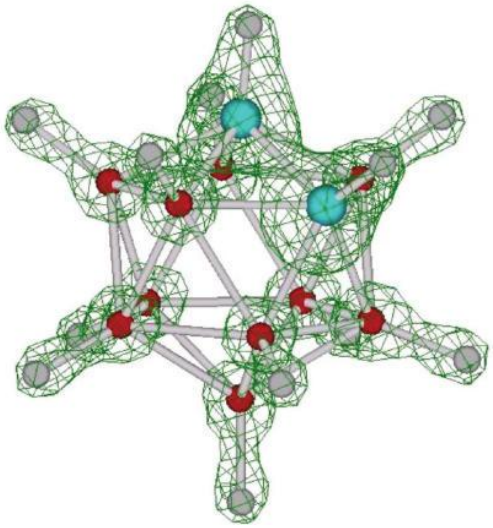

Figure 4.7. The charge densities of the frontier orbitals for *ortho*-1,2-closo-dicarbadodecaborane, based on the Mulliken charge populations, calculated using the hybrid density function theory (DFT-B3LYP). The larger blue is carbon, red is boron.

To confirm the site location of dehydrogenation, ammonia was used as a "probe" molecule, as has been reported recently [18]. The VUV excitation energy used here (8.4 eV) is below the ionization threshold of gaseous NH_3, and the most significant excitation reaction is [18,19]:

$$NH_3 + hv \rightarrow NH_2^*(\tilde{A}^2A_1) + H \qquad (2)$$

Given a source-sample distance of ~2 cm, an NH_3 pressure of 10^{-4} Torr, and an NH_3 absorption coefficient (K) at this wavelength of ~90 $atm^{-1}cm^{-1}$ [18], the relative fraction of photons absorbed by NH_3 molecules, according to the Beer-Lambert law,

is only 2 x 10^{-5}. Therefore, absorption of photons by the gas can be neglected. Similarly, an estimation of the "effective pressure" due to NH_2^* is ~ 10^{-9} Torr, indicating that such effects can be neglected under the conditions of these experiments.

In the absence of VUV irradiation of the semiconducting "$C_2B_{10}H_x$" boron carbide films, there is no uptake, absorption or adsorption of nitrogen containing species at ambient temperatures upon exposure to NH_3. It is only in the presence of both ammonia and VUV radiation (8.4 eV) that nitrogen adsorption is observed [3], as seen in Figure 4.8. This core level spectra photoelectron spectra (XPS) were measured by my collaborators at the University of North Texas.

Referencing the energy of the main C 1s feature (Figure 4.8b,i) to the binding energy of aliphatic carbon, 285 eV, and a C 1s shoulder feature is observed at a binding energy of 283 eV, yields a B 1s maximum at 187.9 eV in excellent agreement with results in the literature [20-22]. A small N 1s feature (Figure 4.8d-i) is also observable for the pristine sample, even in the absence of a sample (empty sample holder), and is due to signal contamination from the Ta sample holder (the signal was observed with only the sample holder in the chamber and no semiconducting boron carbide sample present). The lower electronegativity of B relative to C indicates that B atoms bonded to C (B-C) should have lower charge densities and therefore higher core level binding energies than boron atoms bound to other boron atoms (B-B),

neglecting possible final state effects. Accordingly, the B 1s core level spectrum (Figure 4.8a,i) could be accurately decomposed into B 1s components at binding energies of 187.8 eV and 189.3 eV for the B-B and B-C environments, respectively [21].

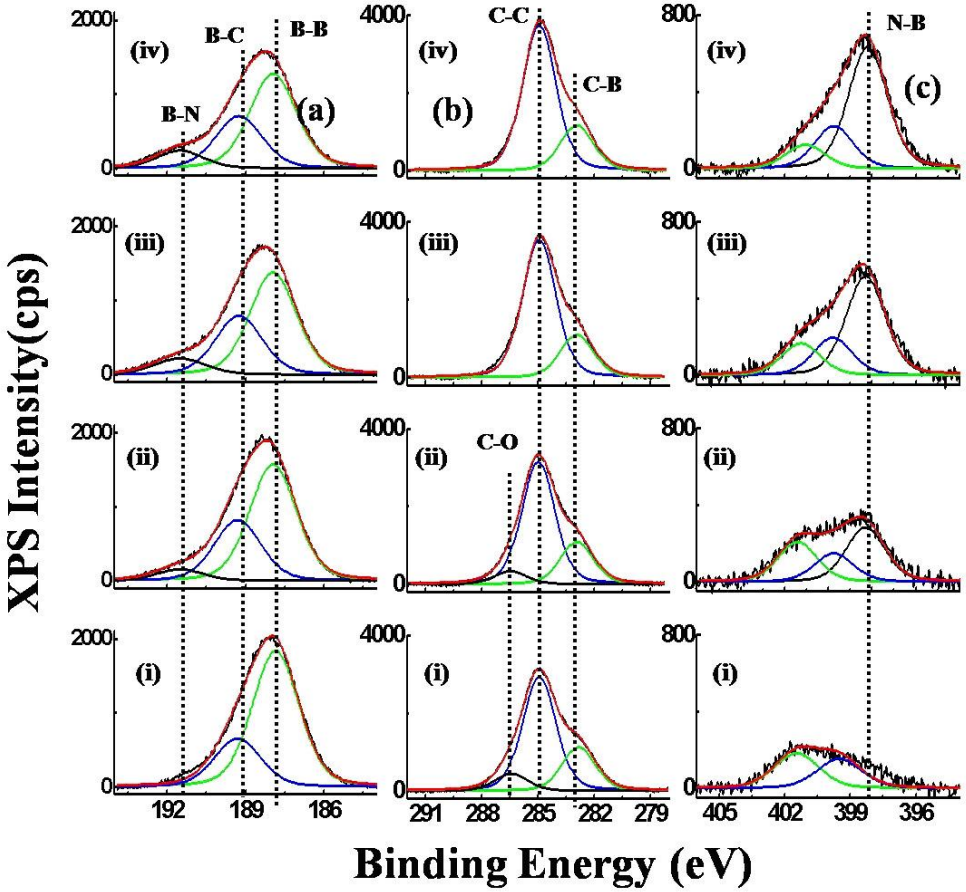

Figure 4.8. Evolution of core level spectra photoelectron spectra (XPS) of heavily hydrogenated semiconducting "$C_2B_{10}H_x$" boron carbide films as a function of exposure to 8.4 eV photon flux in the presence of 10^{-4} Torr NH_3. The core level XPS spectra are shown for the (a) B 1s, (b) C 1s and (c) N 1s core levels for the surface after sputter cleaning procedures and after (i) 0 min, (ii) 30 min, (iii) 90 min and (iv) 180 min exposure to ammonia at 10^{-4} Torr. Adapted from reference [3].

The C 1s spectrum (Fig. 18b,i) can be similarly decomposed into features at 286.7 eV, 285 eV and 282.7 eV attributable to C-O, C-C and C-B (carbide) environments, respectively [20]. From the core level intensities, corrected from core level cross-sections and transmission function of the analyzer, the boron to carbon atomic ratio is estimated to be 4.3:1, consistent with the carbon atoms of the upmost icosahedra of the semiconducting "$C_2B_{10}H_x$" boron carbide films facing the vacuum interface. The relative intensities of B-B/B-C components, however, is 2.9, and reflects the ratio of 2.9 B-B bonds for every C-B bond, though we expect deviations from calculated 2.9 bond ratio due to the expected edge bonding of the icosahedra in the sold state [10].

The evolution of the B 1s, C 1s, and N 1s core level spectra as a function of exposure to 8.4 eV photons in the presence of 10^{-4} Torr NH_3 is displayed in Figure 4.8a-c, ii-iv. Notably, exposure results in a decrease in B 1s intensity near the low binding energy portion of the spectrum, and the growth of a new feature near a binding energy of 192 eV (Fig. 8a, ii-iv). This B 1s binding energy feature is similar in nature to the core level feature identified as being due to B-N bonding environments in boron carbide nanoparticles milled in N_2 [20], and close to the B(1s) binding energy for boron in boron nitrides [23]. During VUV exposure in the presence of NH_3, the B-C feature (Fig. 8a) near 189.3 eV remains unchanged in

relative intensity, indicating that B-C sites are not affected by the B-N bond formation process.

The growth of the N 1s feature near a binding energy of 398.3 eV has been previously identified as due to N bound to B [20], but is somewhat less that the N 1s binding energy for the nitride (399.1 eV [23]). This indicates that the nitrogen atoms contributing to this feature are not in a similar environment as would occur in C-BN—covalently bound to other boron atoms, and that a boron nitride phase is not being formed. The B 1s and N 1s data are instead consistent with formation of a $-NH_2$ species.

There is no evidence for C-N bond formation with ammonia exposure even in the presence of VUV light at 8.4 eV photon energy, in spite of the "carbon" rich surface of the semiconducting "$C_2B_{10}H_x$" boron carbide films. In the C 1s core level spectra we would be expected to lead to additional intensity at binding energies > 285 eV [20,24], but the high binding energy C 1s features in the region near 286.7 eV (Fig. 4.8b) actually decreases with increasing VUV+NH_3 exposure. The data in Figure 4.8, therefore, suggests N to B bond formation at B-B sites, without any evidence of nitrogen bonding to carbon sites.

The absence of any evidence of C-N bond formation or nitrogen reaction at boron atoms bound to carbon atom sites (Figure 4.8) indicates that N bond formation occurs

primarily at reactive sites formed by B-H bond scission at B atoms bound only to boron, rather than to C nearest neighbors:

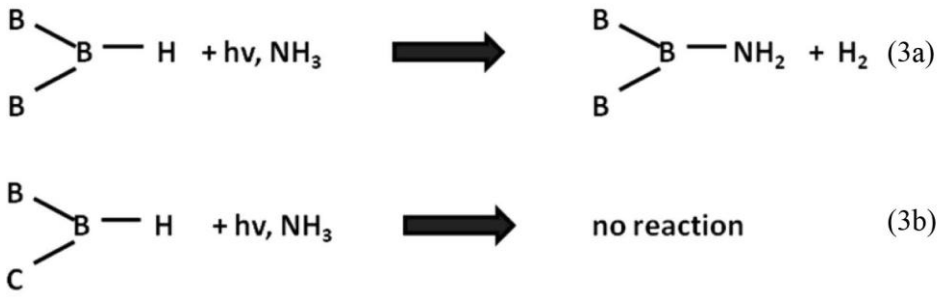

Although the exact mechanism for hydrogen loss and the site-specific amine bond formation mechanism are not known from our experimental data of the heavily hydrogenated semiconducting boron carbide, the results are consistent with studies of gas phase carboranes just discussed above. In the gas phase dehydrogenation cation reaction, the lowest energy pathway for photodissociation near the ionization threshold is pair-wise loss of atomic hydrogen, and the corresponding to the formation of H_2. In the solid state, the semiconducting boron carbides are excitonic insulators, so "local" cation formation is possible with a long lifetime charge restricted to the icosahedral cage "building bock" of the semiconductor material. The site-specific nitrogentation of solid boron carbide (Figure 4.8, eqns. 3a,b) is therefore consistent with the gas phase experimental and theoretical data (Figures 4.3,4.4,4.5) indicating that formation of a cation near the ionization threshold is followed by correlated B-H bond scission at B sites opposite carbon atoms and loss of H_2. There is an important

and obvious caveat: H_2 production from the cation parent molecule likely occurs from adjacent cage B-H sites, as discussed above; but in the solid state, the amidization of equation 18a itself may produce H_2 from a single B-H site. The energy gain for the reaction of equation 3 was found to be slight for the *closo*-carboranes (about -0.12 eV per bond). Overall, a photoactivated reaction is thus not a complete surprise.

4.2 Energetics of single ion fragmentation processes

4.2.1 Ionic photofragmentation measurement by time of flight (TOF) mass spectroscopy

To investigate the ionic fragmentation, a time-of-flight mass spectrometer was used. Time-of-flight ion mass spectra of the three *closo*-carborane isomers obtained with both electron impact and photon ionization are done by my collaborators, as shown in Figure 4.9. The most dramatic difference between the electron impact and the photoionization mass spectra is in the parent ion yield. The fragmentation yields differ significantly from those following valence ionization using 70 eV electron impact and 202 eV incident photons but do not vary greatly in different B 1s states. By contrast, the parent ion, with some contribution from fragment ions involving loss of one H atom, is by far the dominant signal in the electron impact mass spectrum. Indeed, the high stability of the parent ion produced by electron impact valence shell ionization has been noted in previous discussions of the mass spectra of the

carboranes [25]. At 70 eV impact energy fully 74% of all observed ions have the mass of the parent ion, missing possibly only the mass of one hydrogen or two [26]. In contrast, under our detection conditions the parent ion yield is only ~3% at energies below the onset of B 1s core excitation and drops to less than 1% above the B 1s ionization potential (IP). The TOF signal is associated with Y_n^+ ions (where Y=BH or CH), with all possible n values, although with particularly prominent yields of Y_3^+ and Y_6^+. Note that because of the 20:80 ^{10}B:^{11}B relative abundance, each ion peak (except for the Y^+ signal, shown in detail in inset of Figure 4.9) is actually a family of peaks which are not resolved in the TOF spectra.

Above the core excitation threshold (in the region of 188.9 eV for the B 1s threshold) the very low parent ion yield in the photoionization measurements might be considered to be a consequence of core hole decay leading to extensive ionic fragmentation, including large amounts of multiple ionization, almost all of which ends up as ion pairs. However, the parent ion yield was also very small below 188 eV, in the region of valence ionization, where a greater similarity to the electron impact mass spectrum might be expected. In part this can be attributed to use of a photon energy well above the valence double-ionization threshold (~35 eV), whereas the 70 eV electron impact creates primarily singly ionized states (since electron impact cross sections typically are strong only a few times above threshold). In addition, another important fact is that our TOF system has enhanced sensitivity to low-energy

electrons which distorts the ion yields in favor of the double ionization events which produce typically two electrons, one of which has low kinetic energy.

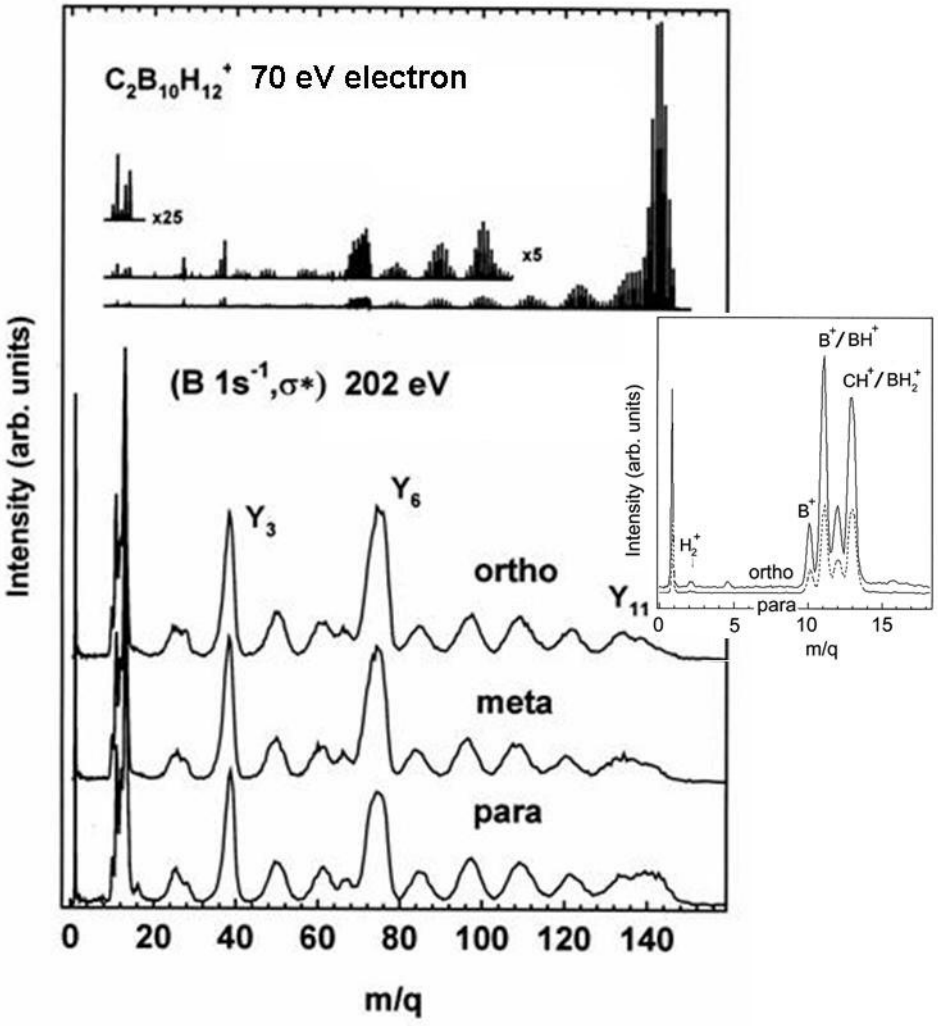

Figure 4.9. Time of flight (TOF) mass spectra of the isomeric caboranes taken at photon energy of 202 eV (bottom spectra). The peaks correspond to cluster fragments with all possible number of vertices, denoted as Y_n^+, where Y represents BH or CH. Enhanced time of flight (TOF) mass spectra in the region of m/q=0 to 18 as inset, adapted from bottom spectra. Note that in this display, peak height is not a reliable

indicator of peak intensity. The top spectrum is from electron impact using electron kinetic energies of 70 eV.

The TOF mass spectra of three carborane isomers with photon energy of 290-292 eV on the peak of the C 1s $\rightarrow \sigma^*$ transition were taken, which is believed to be the C 1s counterpart to the B 1s $\rightarrow \sigma^*$ transition at 202 eV. As with the B 1s excitation, the spectra of three isomers are quite similar to each other. Overall the C 1s and B 1s spectra are quite similar, with the most notable difference being a relatively more prominent contribution from the Y_3^+ and Y_6^+ species in the C 1s than the B 1s region as well as a much larger yield of the lightest fragments, H^+, $^{10}BH^+/^{11}B^+$ (m/q =11), and $CH^+/^{10}BH_3^+/^{11}BH_2^+$ (m/q=13). The very sharp H^+ production at C 1s edge is not strong in the B 1s edge.

The partial ion yields and branching ratio for lighter fragments at B 1s region for three isomers were illustrated Figure 4.10. The following parent and fragment species were identified in the mass spectrum: H^+, $^{10}B^+$, $^{10}BH^+/^{11}B^+$ (m/q =11), $^{11}BH^+$, and $CH^+/^{10}BH_3^+/^{11}BH_2^+$ (m/q=13), etc. Again, para-, meta- and orthocarboranes spectra are quite similar, with the main variations being changes in the detailed line shape and partial overlap of BH+ and H+ branching ratios and partial ion yields for metacarborane. When the signals from the ions $CH^+/^{10}BH_3^+/^{11}BH_2^+$ (m/q=13), H^+ and $^{11}B^+/^{10}BH^+$ (m/q=11) are compared, the strong signal is associated with

$CH^+/^{10}BH_3^+/^{11}BH_2^+$ (m/q=13) followed by B^+ and H^+. The changes in ion yield are most dramatic at the absorption core threshold below about 192 eV for the B 1s but also increase dramatically at the ionization limits, as determined by XPS [27,28] and

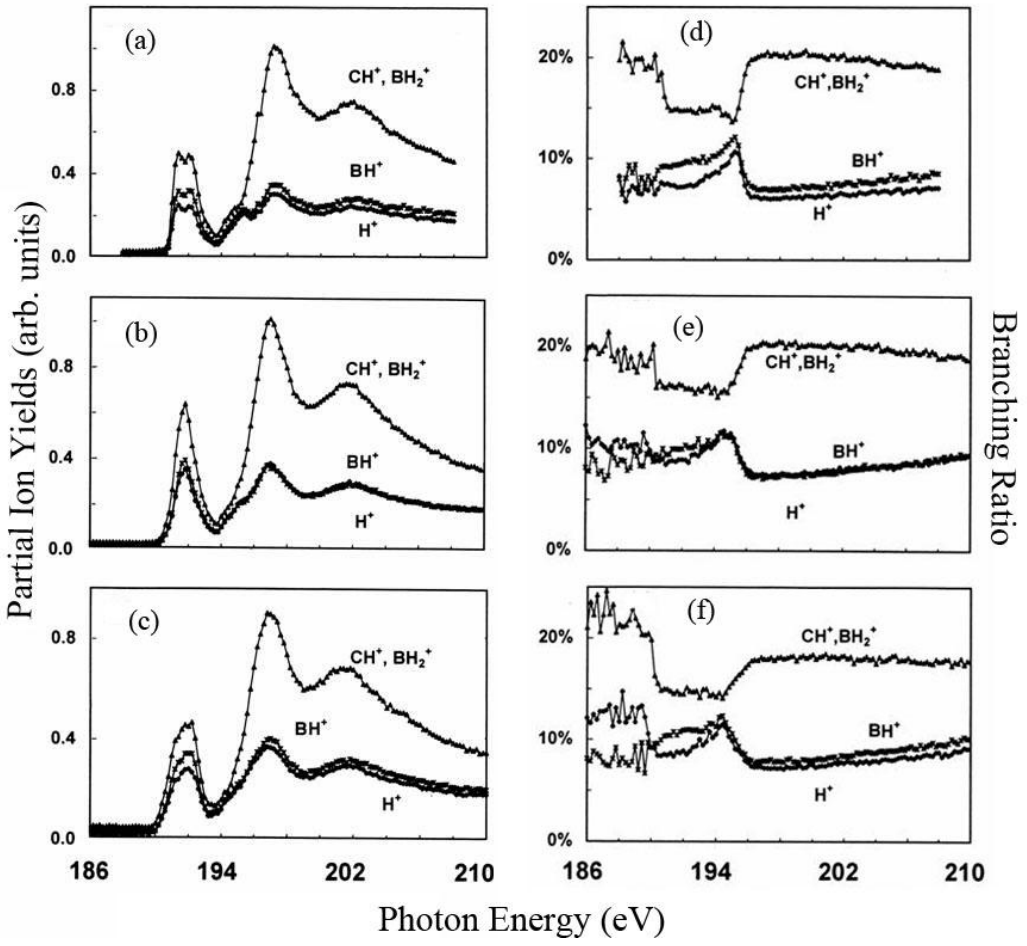

Figure 4.10. Ion yield data for the major ion fragments of *closo*-1,2-orthocarborane (a), *closo*-1,7-metacarborane (b), and *closo*-1,12-paracarborane (c) and Branching ratio for the major ion fragments of for *closo*-1,2-orthocarborane (d), *closo*-1,7-metacarborane (e), and *closo*-1,12-paracarborane (f) derived from sequences of TOF mass spectra recorded in the B 1s region using the same conditions as used for Figure 4.9.

excitations to antibonding σ^* orbitals of unspecified symmetry [27,29] at energies above 194 eV, as noted above. The core ionization energy is approximately the core-level binding energy plus the energy difference between the chemical potential and the vacuum level, the latter being the work function of the condensed phase, i.e., 188.7($\pm$0.2) + 5.5($\pm$1) eV or about 194 eV.

For the heavier Y_n^+ ion (where Y=BH or CH) fragments, the ion yields and branching ratio have been plotted for orthocarborane (Figure 4.11) and paracarborane (Figure 4.12). Y_3^+ and Y_6^+ are the most prominent in both cases, although the branching ratios differ somewhat from one isomer to the next. These heavy ion yields

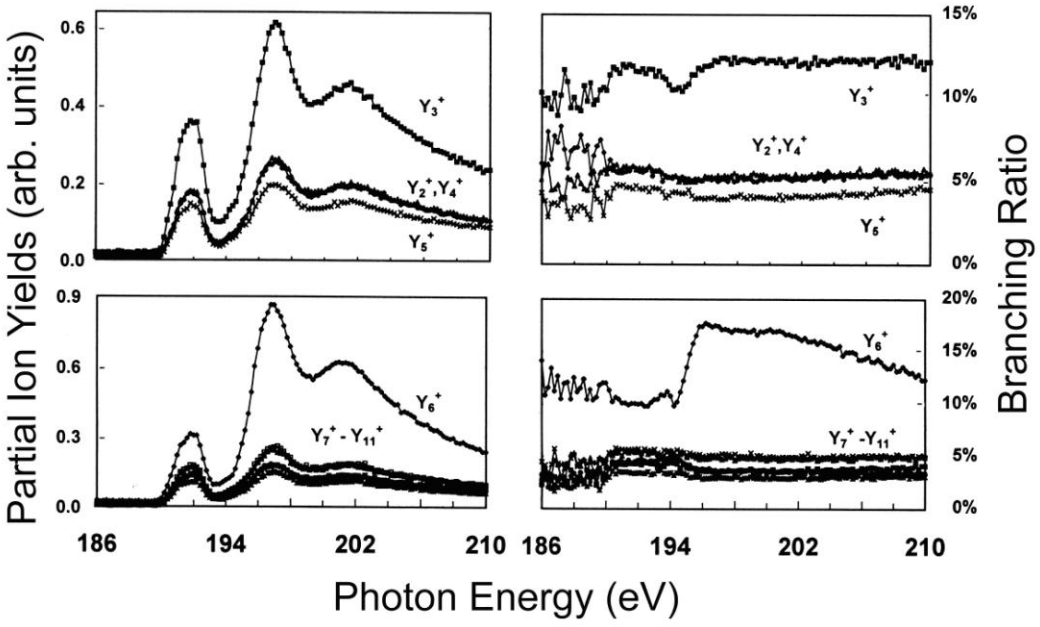

Figure 4.11. Ion yield and branching ratio data for Y_n^+ ions (where Y=BH or CH, as indicated in Figure 4.10) fragments of *closo*-1,2-orthocarborane derived from sequences of TOF mass spectra recorded in the B 1s region using the same conditions as used for Figure 4.9.

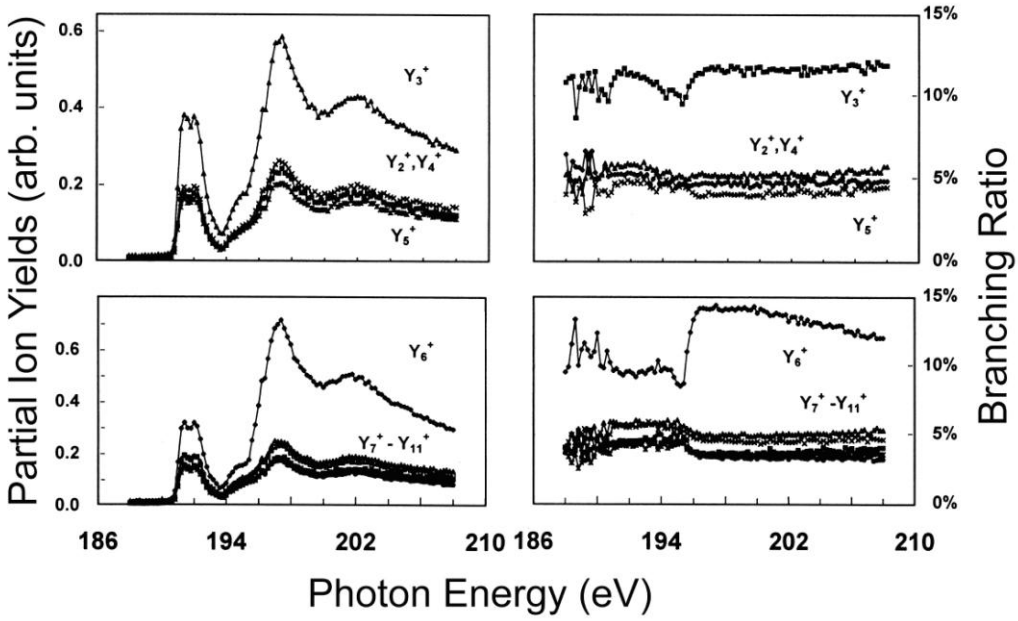

Figure 4.12. Ion yield and branching ratio data for Y_n^+ ions (where Y=BH or CH, as indicated in Figure 4.10) fragments of *closo*-1,12-paracarborane derived from sequences of TOF mass spectra recorded in the B 1s region using the same conditions as used for Figure 4.9.

also change dramatically at excitations to antibonding σ^* orbitals of unspecified symmetry above 194 eV [27,29]. Regrettably, a direct relationship between the excitation to specific unoccupied orbitals and the ion fragment yield cannot be determined from this data.

In spite of differences in the heavy Y_n^+ ion (where Y=BH or CH) fragment yields, overall there is little difference among the partial yields of the isomeric species and relatively little change in individual ion or ion pair yields, which are a result of fission

of the doubly or multiply charged molecules, aside from a major step up or step down in specific channels at the onsets of B 1s core excitation and ionization [27,29] These changes at the ionization threshold are qualitatively consistent with changes in the estimated photoionization efficiency [27] Thus, any selectivity among these three species which may exist with regard to properties of boron carbide films prepared by X-ray assisted CVD is more likely to be associated with specificity of the chemistry of fragments or due to different relaxation processes (which are not known) rather than selectivity in the initial excitation.

At issue is the origin for the very high production of $CH^+/^{10}BH_3^+/^{11}BH_2^+$ (m/q=13) fragments in the photofragmentation process. This can be understood, in part, from the energetics associated with photoionization and fragmentation. As seen in Figure 4.10, however, these yields also increase where excitations to antibonding σ^* orbitals of unspecified symmetry occur [27,29] at energies above 194 eV. The application of energetics to the heavy Y_n^+ ion (where Y = BH or CH) fragment yields (Figures 4.11 and 4.12) is more difficult as specific fragment ion identification is fraught with difficulties based on the data presented here, but again these yields also increase where excitations to antibonding σ^* orbitals of unspecified symmetry occur at energies above 194 eV.

4.2.2 Energetics of *closo*-carborane decomposition

The measured yields depend on the ionization process and associated fragmentation (Figure 4.10), e.g., electron impact versus photoionization. The dominant signal is loss of one H atom for the electron impact mass spectrum, while for photoionization mass spectra, the majority of the TOF signal are associated with $(B/BH)_n^+$, $CH^+/^{10}BH_3^+/^{11}BH_2^+$ (m/q=13), or $(CH)_n^+$ ions. In order to understand the difference yields in the core-level resonant photoionization processes and evaluate the thermal stability of the *closo*-carboranes, the energetics for several reactions which involve loss of small fragment ions of carbon, boron, and hydrogen atoms have been calculated for all three parent *closo*-carboranes using both the PM3 semiempirical model and DFT, as shown in Figure 4.13.

There are many (energetically) different site symmetry combinations of boron, hydrogen, and carbon atoms that are candidates for ion (and neutral) fragmentation. This is especially true for the meta- and orthocarboranes because of their lower symmetry structures (C_{2v} instead of D_{5d}).

The symmetrically distinct possibilities for *closo*-carboranes are associated with different energies, as illustrated in Figure 4.13, where the fragmentation energies are plotted in ascending order, as ascertained using DFT. Also shown for comparison are values obtained using the semiempirical PM3 approach, which differ significantly in absolute energies but typically show the same trends as DFT, as seen in Figure 4.13. As expected, the fragmentation energies of the three isomeric species are quite similar,

consistent with the photoionization and fragmentation experimental results. For orthocarboranes, the minimum energies to remove atoms occurs for atoms located typically near the sites of the carbon atoms, except for the loss of H^+ from orthocarborane. In the case of meta- and paracarboranes, loss of H^+ from sites near the carbon are favored. In the production of H_2, it has already been noted that the initial state site does play a role with pairwise (adjacent sites) H loss favored, with one site

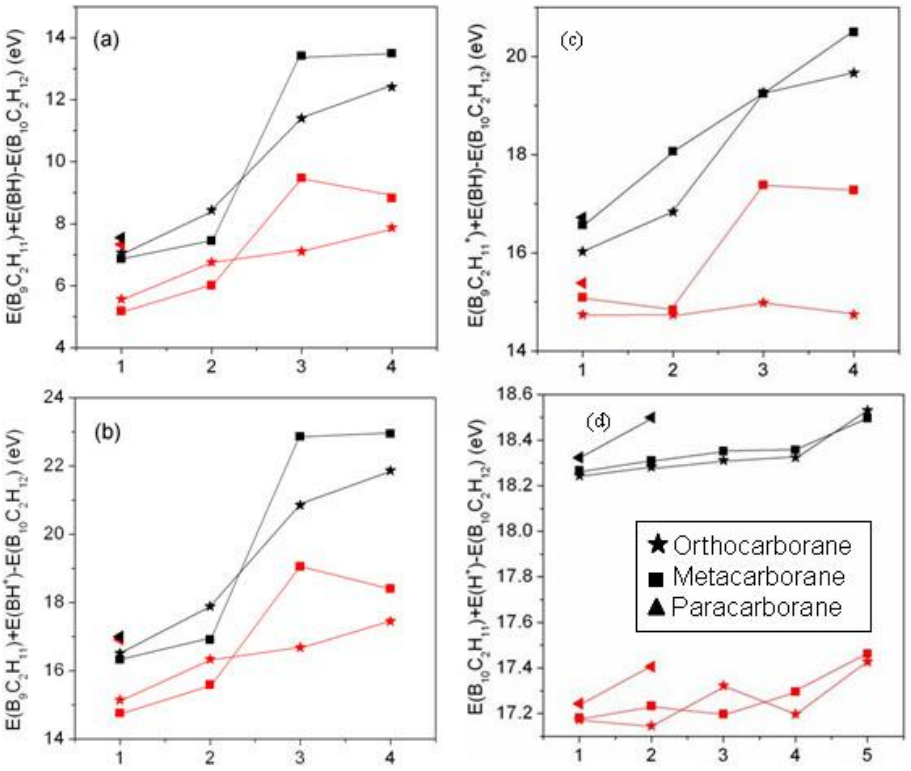

Figure 4.13. Calculated ion fragmentation energies for BH (a), BH^+ (b), $C_2B_9H_{11}^+$ (c) and H^+ (d) by semi-empirical PM3 method (red) and density functional theory (DFT) (black) methods for three isomeric *closo*-carboranes.

including a carbon atom [2]. The absence of H_2^+ in the data can be understood as formation of this ion fragment is very energy expensive, requiring 28.5 eV or more per molecule.

On the basis of the DFT, the energetics of closo-carboranes fragmentation and fragment ionization have been used to construct thermodynamic cycles to illustrate the reaction energies, as shown in Figure 4.14. Each value is the minimum energy calculation among all possible symmetrically inequivalent possibilities. The choice of thermodynamic cycles is based on he observed ion fragmentations, removing CH, CH^+, BH, BH^+, BH_2, BH_2^+, H_2, H, H^+, BCH_3, and BCH_3^+ from each of the three isomers of the *closo*-carboranes, as undertaken by us for far more simple parent molecular species.

The calculated energetics are consistent with formation of $^{11}BH_2^+$ over CH^+ or $^{11}BH^+$. While we cannot distinguish $CH^+/^{10}BH_3^+/^{11}BH_2^+$, the most probable formation paths of BH_2^+, BH^+ and CH^+ fragment ions are

$$C_2B_{10}H_{12} \rightarrow C_2B_9H_{10} + BH_2^+ + e^- \quad (4)$$

$$C_2B_{10}H_{12} \rightarrow C_2B_9H_{11} + BH_2^+ + e^- \quad (5)$$

$$C_2B_{10}H_{12} \rightarrow CB_9H_{10} + CH^+ + e^- \quad (6)$$

The energy cost for BH_2^+ ions formation is about 0.5 eV per molecule less than is the case for the most probable formation paths of BH^+ fragment ions which is about 2.5-3.5 eV per moleculeless again than is the case for the most probable formation paths of CH^+ fragment ions.

The energetics indicate the most likely ion species are BH_2^+ and $C_2B_9H_{11}^+$. The latter may be consistent with decomposition initiated by core to bound photoexcitations, illustrated in Figures 4.9-4.12, but we are limited by the fact that we cannot distinguish BH_2^+ and CH^+ in our data. Given the large size of some of the ion fragments, kinetic barriers to the fragment ion formation may be a significant hindrance, as could be symmetry [30,31], and this has not been considered in the calculations undertaken here. More importantly, above the core threshold, molecular fission and multiple ion fragment production is likely [5]. A similar problem is evident in that H^+ production is more intense than BH^+ well below the B 1s core threshold inconsistent with the energetics of ion fragmentation, which slightly favors BH^+ production over H^+, as observed in the region of the B1s threshold and above.

Excited-state lifetimes or excitations to specific unoccupied molecular orbitals may play a significant role in the ion fragmentation yields, as suggested by the strong photon energy dependence of the ion fragmentation yields (Figures 4.10-4.12). Kinetic barriers to fragmentation are certainly not considered in these energetic calculations.

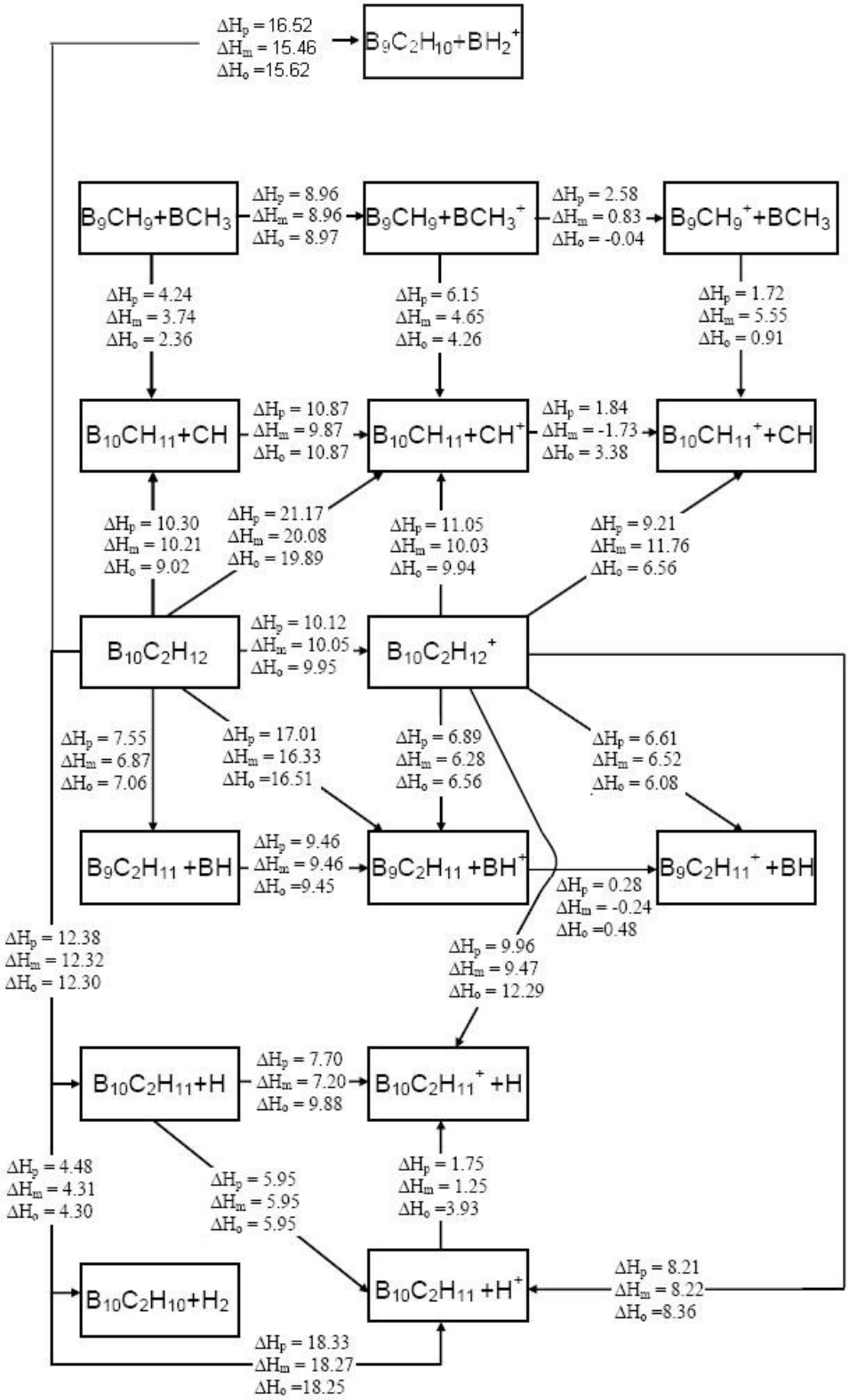

Figure 4.14. Energetics of *closo*-1,2-orthocarborane (H_o), *closo*-1,7-metacarborane (H_m), and *closo*-1,12-paracarborane (H_p) neutral and ionic fragmentation. $\triangle H_o$, $\triangle H_m$

$\triangle H_p$ respectively represent the energy costs of each fragmentation path for three isomers of *closo*-carborane. All energies were calculated using density functional theory and are given in units of eV/molecule.

4.3 Double cation fragmentation

The single photofragmentation studies is a starting point to get insights of the fragmentation mechanisms of plasma-enhanced chemical vapor deposition and white light synchrotron-initiated decomposition processes of *closo*-carboranes. The multiple ion fragmentation is not only possible but likely at or above B1 s and C 1s threshold. The attempts to explore the double cation fragmentation processes have been made by coincidence TOF mass spectroscopy as well as the construction of energetics.

4.3.1 Double and triple coincidence time of flight mass spectra

The photoion-photoion coincidence (PIPICO) mass spectra show the coincidence counts as function of the difference in time of arrival of two ions, as exemplified in Figure 4.8a for *closo*-1,7-dicarbadodecaborane (metacarborane). Note again that because of the 20:80 ^{10}B:^{11}B relative abundance, each ion peak (except for the Y_1^+ signal) is actually a family of peaks which are not easily resolved in the TOF spectra. The most prominent peaks in the PIPICO spectra of 1,3-carboraneare,

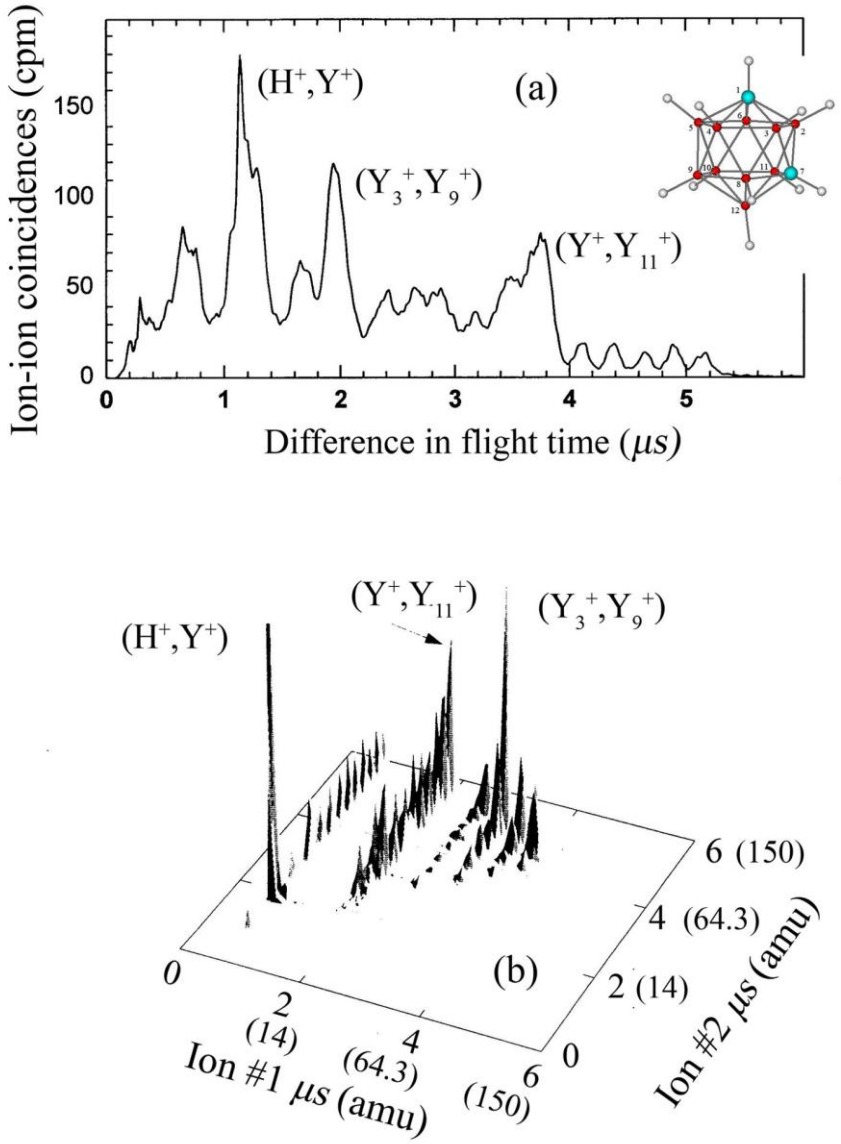

Figure 4.15. Photoion-photoion coincidence (PIPICO) spectrum (top) and photoelectron-photoion-photoion coincidence (PEPIPICO) spectrum (bottom) for metacarborane recorded at 192 eV photon energy, above the B 1s threshold (188 eV) are shown. The peaks corresponding to cluster fragments are denoted as Y_n^+, where Y represents BH or CH.

recorded at 192 eV photon energy, in Figure 4.8a, are associated with H^+ and BH_2^+/CH^+ ion pairs, BH_2^+/CH^+ and Y_{11}^+ ion pairs (where Y = (BH) or (CH)), Y_3^+ and Y_9^+ ion pairs (where Y = (BH) or (CH)). The differences of time of flight corresponding to these pairs respectively are about at 1.16 μs, 1.95 μs and 3.75 μs. In Figure 4.15a, the peak shape for Y_3^+/Y_9^+ ionic fragments suggests a "narrow" single peak which indicates that most of the momentum is imparted perpendicular to spectrometer axis after dissociation. The peak corresponding to Y^+/Y_{11}^+ ionic fragments is slightly off rectangular, which suggests that it is likely little or no alignment after cation dissociation.

In Figure 4.15b, the triple coincidence PEPIPICO signals were recorded as a function of the times of light of two ions in each pair at photon energy of 192 eV. The mass of ions were also calibrated from the time-of-flight mass spectra, as indicated elsewhere [3,4,6]. The coincidence event information from the PEPIPICO spectra is rich and three major features are identified in Figure 4.8b, for *closo*-1,7-carborane at a photon energy of 192 eV; an energy above the B 1s-absortion edge of 188 eV photon energy [26,28]. The intensity of signals contributed by H^+ and BH_2^+/CH^+ ion pairs with neutral Y_{11} fragment, BH_2^+/CH^+ and Y_{11}^+ ion pairs (where Y = (BH) or (CH)), Y_3^+ and Y_9^+ ion pairs (where Y = (BH) or (CH)) yields dominate, which is in consistent with the PIPICO features.

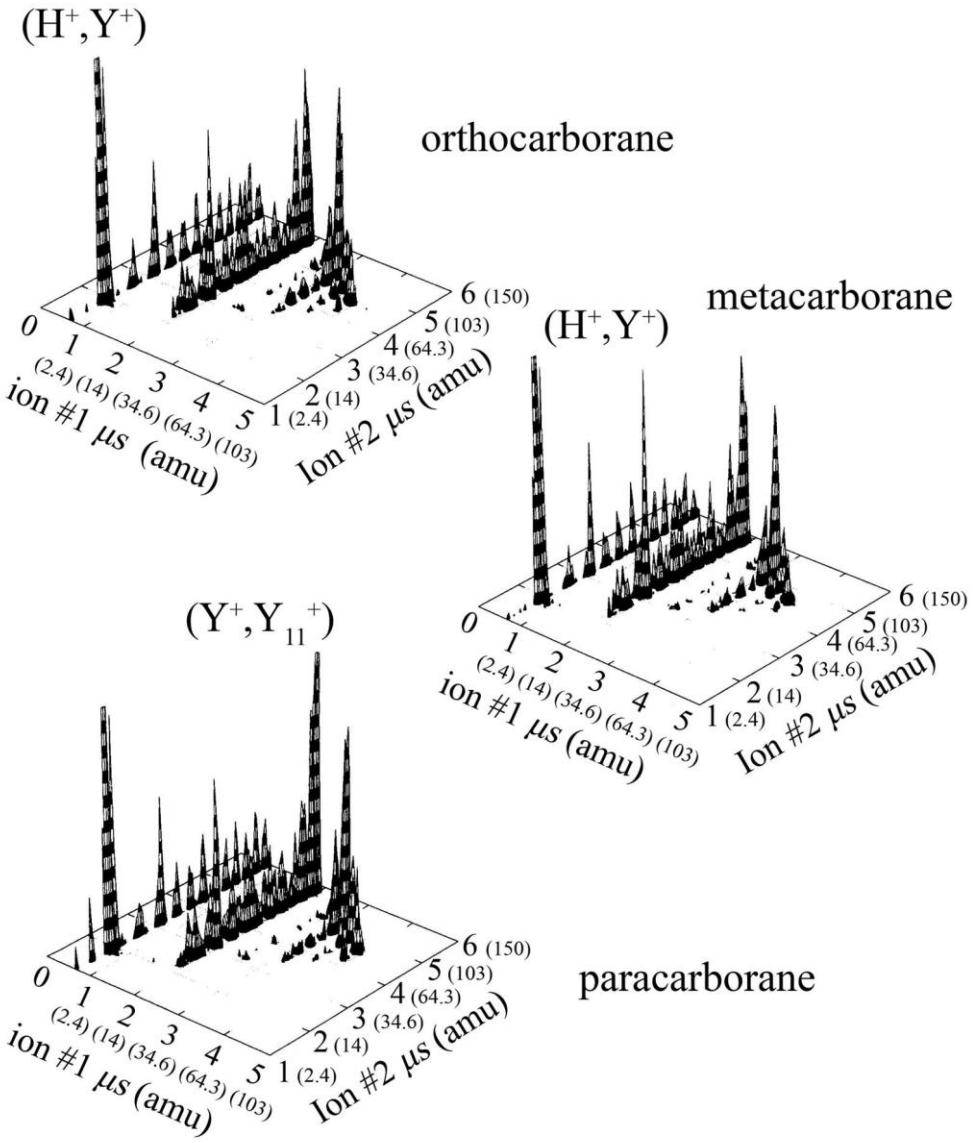

Figure 4.16. Photoelectron-photoion-photoion coincidence (PEPIPICO) spectra taken at photon energy of 202 eV for ortho-, meta- and para- carborane. The time of flight values have been converted to approximate mass values and denoted in brackets (amu).

The contour plot of PEPIPICO in t_1-t_2 plane provides an excellent means for identifying the shape and intensities of the coincidence events. The contour plots on sections of the PEPIPICO spectrum for 1,2-orthocarborane, at 220 eV, has been previously reported [6] and resembles the data, presented here, for lower photon energies. For the H^++Y^+ fission channels, the PEPIPICO spectra contour plots (Figures 4.1 and 4.2) indicates that the H^+ is predominantly correlated with $^{11}B^+$, $^{11}BH^+$ and CH^+ and the unseen neutral fragment corresponds to Y_{11}. It was proposed that the charges delocalize before fission occurs in this three body dissociation based on data of kinetic energy release and geometry of neutral [6].

It was observed [6] that the main signals in Y^+ and Y_{11}^+ ion pair yield correspond to B^++Y_{11}^+(m/z=124) and CH^++Y_{11}^+(m/z=124). The slope of B^++Y_{11}^+(m/z=124) signal is -1 ± 0.05, which is typical for two body fission or deferred charge separation. Overall, asymmetric dissociation dominates the dissociation processes of 1, 2-orthocarborane [6], and we believe this to be true of the other isomers of the icosahedral *closo*-dicarbadodecaboranes.

The comparison between the photoelectron-photoion-photoion coincidence time-of-flight (PEPIPICO TOF) mass spectra of the three carboranes excited by 202 eV photons (B 1s continuum) shown in Fig. 16. Clearly the fragmentation yields and charge separation mass spectra at photon energy of 202 eV of all three isomers are generally quite similar in that H^+ and BH_2^+/CH^+ ion pairs, BH_2^+/CH^+ and Y_{11}^+ ion

pairs (where Y = (BH) or (CH)), Y_3^+ and Y_9^+ ion pairs (where Y = (BH) or (CH)) yields dominate. The coincidence counts seem to be intense as the incident photon energy increased from 192 to 202 eV. The H^+ and BH_2^+/CH^+ ion pairs dominate multi-photofragment ion yield of ortho- and metacarborane at the B 1s threshold, while Y_1^+ and Y_{11}^+ ion pairs (where Y = (BH) or (CH)) have almost same intensity of ion yield as H^+ and BH_2^+/CH^+ ion pairs for paracarborane at the B1s threshold, as summarized in Figure 4.16. The difference may come from the different group symmetry or charge populations of three isomers. A boron or carbon with anionic character will likely remain bonded to a cationic hydrogen in the fragmentation process. Thus the kinetic and symmetry barriers along with ionic dipole atom pair combinations may indeed affect some ion fragments formation.

4.3.2 Enegetics of double ionization and discussion

To further examine the favorable pathways of double ionization of three isomers of *closo*-carboranes, the dissociation energies of the three major ion pairs species observed in both PIPICO and PEPIPICO mass spectra were calculated. All the possible molecular structures of ion pairs, with same mass, were considered in modeling for each dissociation pathway related to the reactions by considering all symmetrically non-equivalent appropriate carbon and boron atom combinations from within the *closo*-carboranes, and we report here the fragmentation energies as those

with the minimum energy cost. The possible pathways of following reactions (7), (8) and (9) as:

$$C_2B_{10}H_{12} \rightarrow H^+ + Y^+ + Y_{11} + 2e^- \quad (7)$$

$$C_2B_{10}H_{12} \rightarrow Y^+ + Y_{11}^+ + 2e^- \quad (8)$$

$$C_2B_{10}H_{12} \rightarrow Y_3^+ + Y_9^+ + 2e^- \quad (9)$$

where Y = (BH) or (CH). The corresponding minimum values for the dissociation energies are shown in Figure 4.17 as associated with each fragmentation reaction.

Due to the limitation of time-of-flight mass spectrometer, the ions with same mass to charge ratio can not be distinguished in the TOF mass spectra. In three body fission processes (7), we examined the energy cost separately for dissociative pathways including H^+, Y^+ as B^+, BH^+, CH^+ and BH_2^+ and corresponding neutral fragments. The boron atom in all the calculations was assumed to be ^{11}B and even with the consideration of all the possible molecular structures of ion pairs with same mass, in modeling for each dissociation pathway related to the reactions (7)-(9), the lower energy dissociation processes are not always favored.

Comparing the calculated minimum energy cost for all three isomers fission reaction, it appears that energetically the H^+/Y^+ pairs are generally most favorable in experiment (Figure 4.16) and yet the Y_3^+/Y_9^+ pair production of $CB_2H_3^+/CB_8H_9^+$ is favored by the experiment.

In the reaction (8) resulting in production of the Y^+ plus Y_{11}^+ ion pairs, the dissociation energies corresponding BH^+ plus $C_2B_9H_{11}^+$ and CH^+ plus $CB_{10}H_{11}^+$ were compared. Energetically, the BH^+ is preferred than CH^+, while in PEPIPICO spectra they showed the same intensity corresponding to m/z=124. For the Y_3^+ and Y_9^+ pairs, the $CB_2H_3^+/B_8H_9^+$ is more favored than C_2BH_3 and $B_3H_3^+$ as lighter fragments. The Y_3^+ ion, removed from parent molecule, prefers a corresponding face or linear chain on the icosahedra cage than separate sites on the cage by energetic arguments. For example for $B_3H_3^+$ ion, the energy cost corresponding to remove a face or chain from the icosahedral cage could be as much as 3.6, 3.3 and 0.8 eV less than separate sites for 1,2-orthocarboarane, 1,7-metacarborane and 1,12-paracarborane, respectively.

Yet it is likely that the local dipoles of the di-cation parent molecules, before dissociation, play a role in the experimentally favored dissociation processes. In comparing the calculated di-cation fragmentation dissociation energies for the experimentally observed major ion pair pathways, the significant differences observed with paracarborane (Figure 4.16), as opposed to meta carborane or orthocarborane, that are not reflected in the calculated energetics (Figure 4.17), suggest that for paracarborane, the difference in the atomic pair local dipole attraction may play a role, particularly if CH^+ is a favored fragment. Although the energy cost pathways among two possible fission pathways of Y^+ and Y_{11}^+ suggests that BH^+ may be more preferred (Figure 4.17), even for orthocarborane CH^+/Y_{11}^+ is favored [6], so that this

may be the origin of the increase in the relative intensity of the di-cation coincidence feature corresponding Y^+/Y_{11}^+ seen with paracarborane (Figure 4.16) compared to the H^+/Y^+ di-cation fragment production. This seems to occur in spite of the reduced energy cost of H^+/Y^+ di-cation fragment production compared to Y^+/Y_{11}^+, even for paracarborane (Figure 4.17).

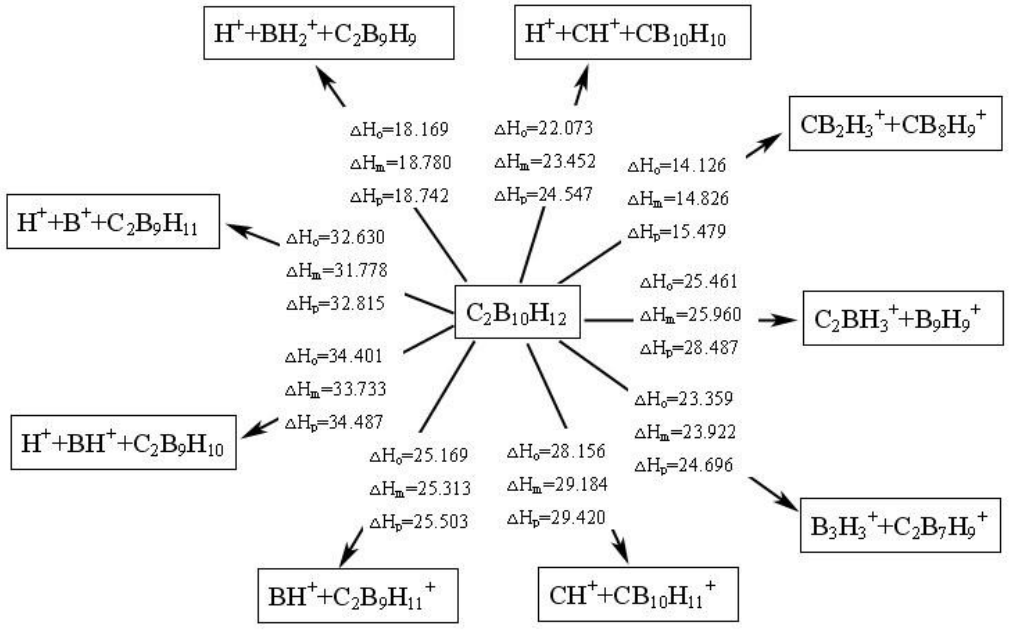

Figure 4.17. Energetics of ortho-, meta-, and para-carboarnes double ion fragmentation for experimentally observed ion pairs ($H^+ + Y^+$, $H^+ + Y^+ + Y_{11}$, $Y_3^+ + Y_9^+$, $Y^+ + Y_{11}^+$). $\triangle H_o$, $\triangle H_m$ $\triangle H_p$ respectively represent the energy costs of each fragmentation path for three isomers of *closo*-carborane. All energies were calculated using density functional theory and are given in units of eV/molecule.

As noted in table 1, the calculated dissociation energies for Y_2^+ and Y_3^+ ion pairs are compared. $CB_2H_3^+$ plus $CB_8H_{10}^+$ ion pairs are most preferred on the basis of

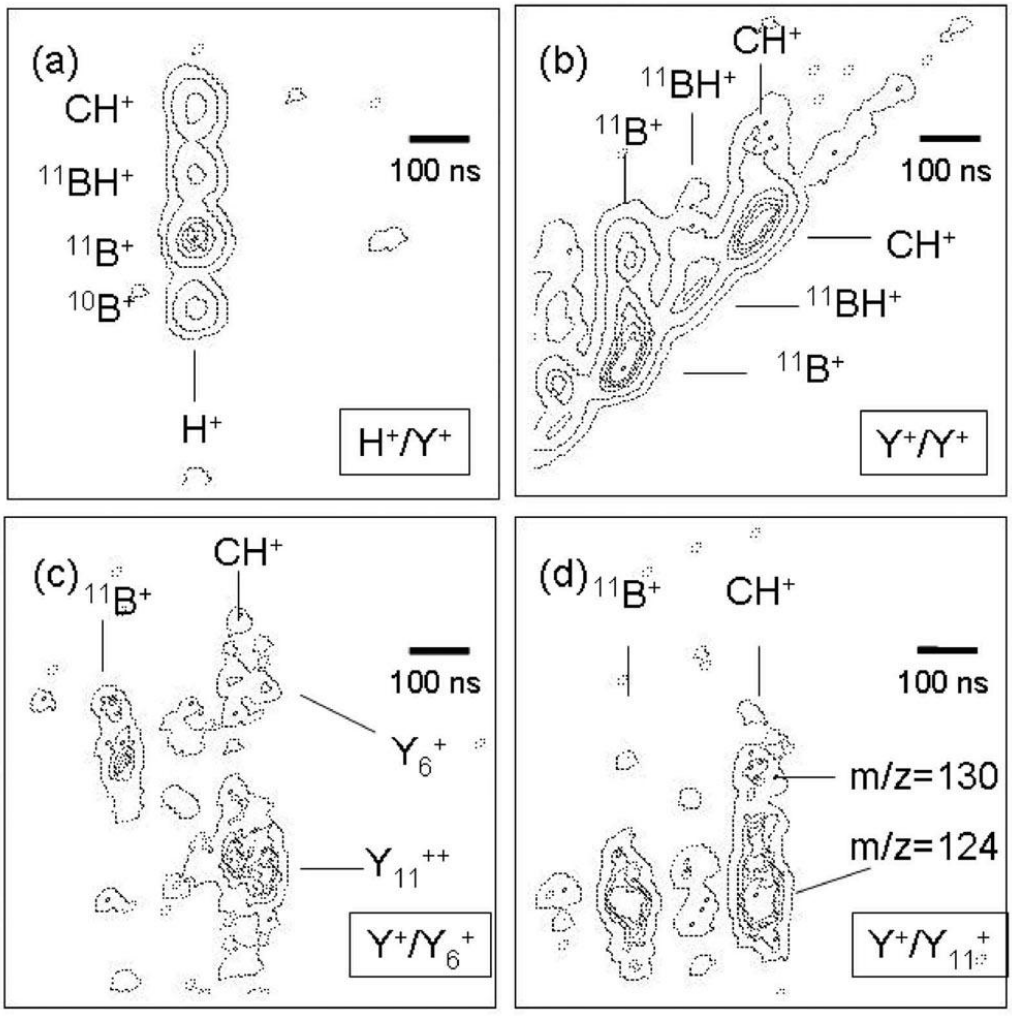

Figure 4.18. Detailed views represented as contour plots on sections of the photoelectron-photoion-photoion coincidence (PEPIPICO) spectrum for *closo*-1,2-dicarbadodecaborane: orthocarborane (1,2-$C_2B_{10}H_{12}$) recorded at 220 eV photon energy (Y^+: CH^+ or BH^+): (a) H^+/Y^+-regime; (b) Y^+/Y^+-regime; (c) Y^+/Y_6^+-regime; (d) Y^+/Y_{11}^+-regime. Adapted from Ref. [6].

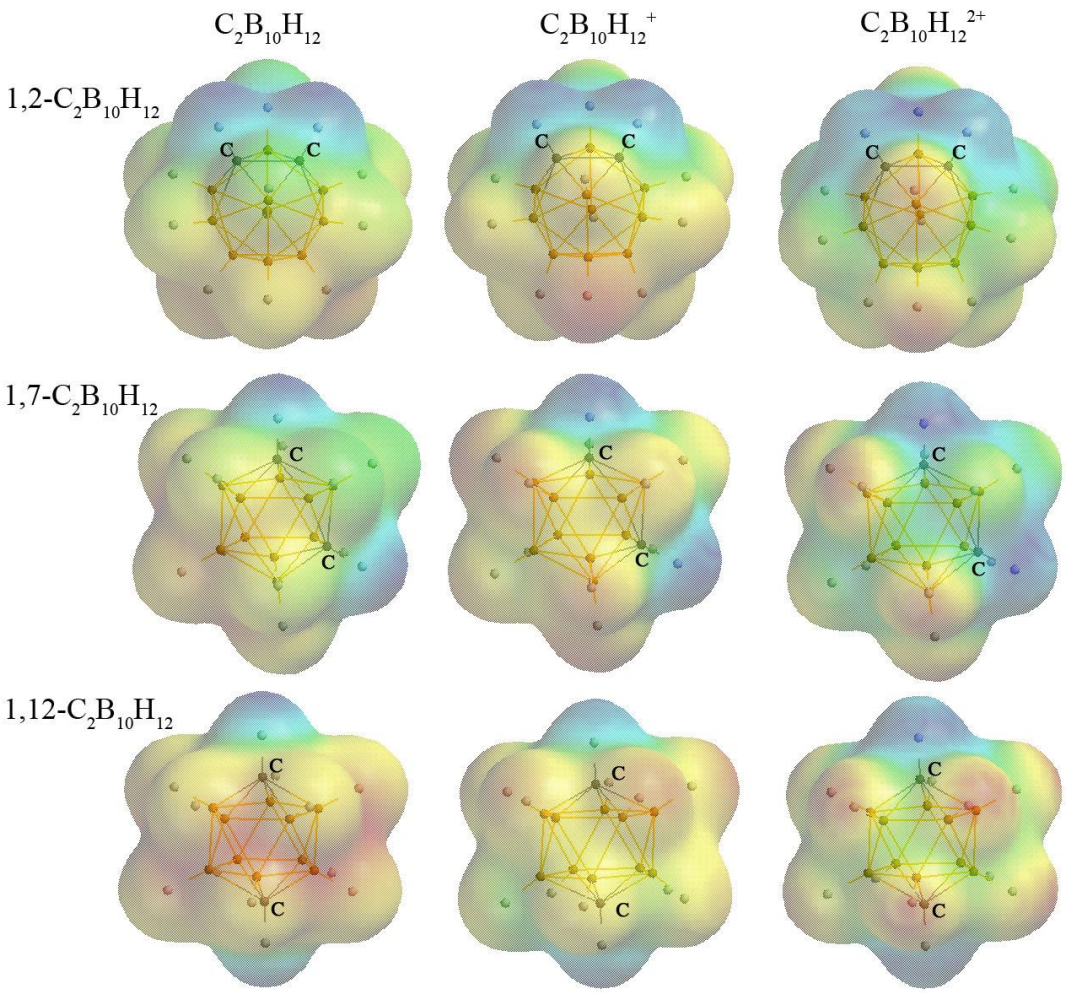

Figure 4.19. Changes in the relative surface charge densities of the three *closo*-dicarbadocedaborane isomers, from neutral (left) to cation (center) to di-cation (right). Blue indicates relatively more positive charge.

energetics. The energy cost is about 8.6 eV to 10 eV lower than $B_2H_2^+$+$C_2B_8H_{10}^+$ ion pairs and 11.2 eV to 12.9 eV lower than CBH_2^++$CB_9H_{10}^+$ ion pairs. Energetically, the Y_3^+ is more stable and favored in fission processed than Y_2^+. This is in generally good agreement with the observation of PIPICO and PEPIPICO spectra. It was observed that the fission processes involving Y_2^+ are weak in PEPIPICO, due to the instability

of Y_2^+. It is on inspection of the detailed fragment intensities, as seen in Figures 4.18, we see more evidence that the energetics is not the sole guide to the favored di-cation production. For the corresponding Y^+/Y_{11}^+ di-cation pair production, BH^+/Y_{11}^+ should be favored over CH^+/Y_{11}^+, but as just noted, even for orthocarborane CH^+/Y_{11}^+ is favored [6].

Table 4.1. Comparison of energies consumed to create ion pairs of Y_3^++Y_9^+ and Y_2^++Y_{10}^+, where Y represents BH or CH.

	$B_3H_3^+$+$C_2B_7H_9^+$ (eV)	$B_2H_2^+$+$C_2B_8H_{10}^+$ (eV)	$CB_2H_3^+$+$CB_8H_9^+$ (eV)	CBH_2^++$CB_9H_{10}^+$ (eV)
Orthocarborane	23.359	24.159	14.126	25.607
Metacarborane	23.922	24.324	14.826	26.308
Paracarborane	24.696	24.045	15.479	28.347

Table 4.2. Selected atomic charges (|e|) of H and B/C on selected positions for *closo*-carborane di-cations, calculated by Mulliken method.

Main Group Atom Position		1	2	4	7	10	12
1,2-$C_2B_{10}H_{12}^{2+}$	H	0.349	0.3349	0.256	0.256	0.182	0.209
	B/C	-0.373	-0.373	-0.067	0.067	0.033	-0.014
1,7-$C_2B_{10}H_{12}^{2+}$	H	0.339	0.256	0.204	0.339	0.247	0.196
	B/C	-0.419	-0.018	0.020	-0.419	-0.067	0.020
1,12-$C_2B_{10}H_{12}^{2+}$	H	0.335	0.253	0.253	0.253	0.253	0.335
	B/C	-0.383	-0.043	-0.043	-0.043	-0.043	-0.383

The Figure 4.19 shows relative surface charge densities of the three *closo*-dicarbadocedaborane isomers. The relative more positive charges are concentrated on the hydrogen connected to carbon sites. From table 4.2, it is clear from the calculated Mulliken charge populations that, for the di-cation, the strongest local dipole localized at the C-H bond for each of the three isomers. In reaction 8, this provides one reason for CH^+/Y_{11}^+ being favored over BH^+/Y_{11}^+ in the Y^+/Y_{11}^+ di-cation pair production, as was observed for orthocarborane [6]. The fact that the B-H bond is not usually a strong dipole, in the di-cation, tends to explain why B^+ separation from H^+ is far more commonly observed than C^+ separation from H^+ in the di-cation fragmentation route 7 [6].

The fact that paracarborane favors the di-cation ion Y^+/Y_{11}^+ pair fragmentation route 8, far more than metacarborane or orthocarborane (as seen in Figure 16), is not explained as easily by the local charge populations or the ground state energetics. But kinetics, not easily calculated, may play a significant role, as may to some extent symmetry, as has been observed with some cation fragmentation processes [30].

4.4 Conclusions

The irradiation of PECVD-deposited hydrogen rich semiconducting "$C_2B_{10}H_x$" boron carbide films by 8.4 eV photons in the presence of 10^{-4} Torr NH_3 results in B-N bond formation specifically at boron sites with boron nearest neighbors. No reaction

is observed at carbon sites or at the site of boron atoms bound to carbon, and the amine reaction does not occur in the absence of VUV light. These results are in excellent agreement with density functional theory calculations which indicate that lowest energy H_2/cationic $B_{10}C_2H_{10}$ formation involves B-H bond breaking at sites *opposite* the carbon atoms for pair-wise H-B and H-C dissociation/H_2 formation from a variety of *closo*-carborane molecules.

What is clear is dehydrogenation of the parent *closo*-carborane cations is dominated by H_2 loss. The largely H_2 loss by the parent cation occurs at energies just above the photoionization threshold for orthocarborane (1,2-$C_2B_{10}H_{12}$), metacarborane (1,7-$C_2B_{10}H_{12}$), paracarborane (1,12-$C_2B_{10}H_{12}$), 1-phospha-2-carbadodecaborane (1,2-$PCB_{10}H_{11}$) and 1-phospha-7-carbadodecaborane (1,7-$PCB_{10}H_{11}$).

In the region of the B 1s and C1s core thresholds, single photoion creation is relatively more straightforward to model but is generally best applicable near the appearance and ionization potentials. Although we cannot distinguish between $CH^+/^{10}BH_3^+/^{11}BH_2^+$ in the TOF mass spectroscopy of the photofragmentation in the region of the B 1s and C1s core thresholds , the energetics of decomposition favors formation of BH_2^+ rather than the mass equivalent CH^+. The possible long-lived bound core excitations result in the high H^+ and B^+ production, but the strong variations in fragment ion yields with photon energy implicate kinetic and symmetry

barriers to some ion fragment formation. In addition, a direct relationship between excitation to specific unoccupied orbitals and ion fragment yield cannot be determined from this data and is not evident from the present results. As a result, energetics alone is not a reliable guide to fragmentation yields, particularly above the B 1s core threshold where multiple fragment creation from the photofragmentation is likely. It is believed there is significant bias toward low-energy electrons, and thus, events in which stepwise electronic decay occurs, giving rise to both copious fragmentation and slow electrons.

In this study of the coincidence time-of-flight (PEPIPICO TOF) mass spectra of three *closo*-carborane isomers, taken using photo-excitations in vicinity of the B 1s core threshold, we see many similarities between the three isomers. Fragmentation yields and charge separation mass spectra of all three isomers are generally quite similar in that H^+ and BH_2^+/CH^+ ion pairs, BH_2^+/CH^+ and Y_{11}^+ ion pairs (where Y = (BH) or (CH)), Y_3^+ and Y_9^+ ion pairs (where Y = (BH) or (CH)) yields dominate. The strong dominance of select cation pairs indicates that the di-cation fragmentation is not a statistical process, but is not solely governed by the fragmentation energetics. With the di-cation in the vicinity of the B 1s core threshold, we find that the fragmentation energetics are not an infallible guide to the observed fragmentation. This is very different from the simpler cation fragmentation [4] and the loss of H_2 from the parent cation [3], where the energetics are a reliable indicator of the likely

fragmentation pathways. The strong difference observed with paracarborane provide a compelling indication that the cation molecular symmetries may influence the fragmentation processes at or greater than the core level B 1s threshold energy.

Reference:

[1] D. L. Schulz, A. Lutfurakhmanov, B. Maya, J. Sandstrom, D. Bunzow, S. B. Qadri, R. Bao, D. B. Chrisey and A. N. Caruso, J. Non-Cryst. Sol. **354**, 2369 (2008).

[2] K. Park, M. R. Pederson, L. L. Boyer, W. N. Mei, R. F. Sabirianov, X. C. Zeng, S. Bulusu, S. Curran, J. Dewald, E. Day, S. Adenwalla, M. J. Diaz, L. G. Rosa, S. Balaz and P. A. Dowben, Phys. Rev. B **73**, 035109 (2006).

[3] E. Ruhl, N. F. Riehs, S. Behera, J. Wilks, J. Liu, H.-W. Jochims, A. N. Caruso, N. Boag, J. A. Kelber and P. A. Dowben, J. Phys. Chem. A **114**, 7284 (2010).

[4] D. Feng, J. Liu, A. P. Hitchcock, A. L. D. Kilcoyne, T. Tyliszczak, N. Riehs, E. Ruhl, J. D. Bozek, D. McIlroy and P. A. Dowben, J. Phys. Chem. A **112**, 3311 (2008).

[5] J. Liu, E. Rühl, A. P. Hitchcock, D. N. McIlroy, J. D. Bozek, A. L. David Kilcoyne, T. Tyliszczak, A. Knop-Gericke, N. M. Boag and P. A. Dowben, "Photo-fragmentation of the *closo*-Carboranes Part III: Double Cation Fragmentation", in preparation.

[6] E. Rühl, A. P. Hitchcock, J. D. Bozek, T. Tyliszczak, A. L. D. Kilcoyne, D. N. McIlroy, A. Knop-Gericke and P. A. Dowben, Physica Status Solidi B **246**, 1496 (2009).

[7] Z. Y. Liu, P. A. Dowben, A. P. Popov and D. P. Pappas, Phys. Rev. A **67**, 033202 (2003).

[8] K. P. Huber and G. Herzberg, Molecular Spectra and Molecular Structure Constants of Diatomic Molecules, (Van Nostrand: New York, New York ,1979).

[9] H. C. Longuet-Higgins and M. de V. Roberts, Proc. Roy. Soc. Lon. A **230**, 110 (1955).

[10] L. Carlson, D. LaGraffe, S. Balaz, A. Ignatov, Ya. B. Losovyj, J. Choi, P. A. Dowben and J. I. Brand, Appl. Phys. A **89**, 195 (2007); P. A. Dowben, O. Kizilkaya, J. Liu, B. Montag, K. Nelson, I. Sabirianov and J. I. Brand, Mat. Lett. **63**, 72 (2009); J. Liu, G. Luo, W.-N. Mei, O. Kizilkaya, E. D. Shepherd, J. I. Brand and P. A. Dowben, J. Phys. D: Applied Physics **43**, 085403 (2010).

[11] S. Balaz, D.I. Dimopv, N.M. Boag, K. Nelson, B. Motag, J. I. Brand and P. A. Dowben, Appl. Phys. A **84**, 149 (2006).

[12] R. B. Billa, T. Hofmann, M. Schubert and B. W. Robertson, J. Appl. Phys. **106**, 033515 (2009).

[13] S. Balaz, A. N. Caruso, N. P. Platt, D. I. Dimov, N. M. Boag, J. I. Brand, Ya. B. Losovyj and P. A. Dowben, J. Phys. Chem. B **111**, 7009 (2007).

[14] S. Lee, J. Mazurowski, G. Ramseyer and P. A. Dowben, J. Appl. Phys. **72**, 4925 (1992).

[15] A. A. Ahmad, N. J. Ianno, P. G. Snyder, D. Welipitiya, D. Byun and P. A. Dowben, J. Appl. Phys. **79,** 8643 (1996).

[16] P. Lunca-Popa, J. I. Brand, S. Balaz, L. G. Rosa, N. M. Boag, M. Bai, B. W. Robertson and P. A. Dowben, J. Physics D: Applied Physics **38**, 1248 (2005).

[17] S. Balaz, A. N. Caruso, N. P. Platt, D. I. Dimov, N. M. Boag, J. I. Brand, Ya. B. Losovyj and P. A. Dowben, J. Phys.Chem. B **111**, 7009 (2007).

[18] F. Truica-Marasescu and M. R. Wertheimer, J. Appl. Polym. Sci. **91**, 3886 (2004).

[19] V. M. Donnelly, A. P. Baranovski and J. R. McDonald, Chem. Phys. Lett. **43**, 283 (1979).

[20] M. W. Mortensen, P. G. Sørensen, O. Björkdahl, M. R. Jensen, H. J. G. Gundersen and T. Bjørnholm, Appl. Radiation and Isotopes **64**, 315 (2006).

[21] L. G. Jacobsohn, R. K. Schulze, M. E. H. Maia da Costa and M. Nastasi, Surf. Sci. **572**, 418 (2004).

[22] I. Jimenez, D. G. J. Sutherland, T. van Buuren, J. A. Carlisle, L. J. Terminello and F. Himpsel, J. Phys. Rev. B **57**, 13167 (1998).

[23] J. Deng and G. Chen, Appl. Surf. Sci. **252**, 7766 (2006).

[24] J. F. Moulder, W. F. Stickle, P. E. Sobol and K. D. Bomben, Handbook of X-ray photoelectron spectroscopy, (Perkin-Elmer: Eden Prairie, MN, 1995).

[25] N. I. Vasyukova, Y. S. Nekrasov, Y. N. Sukharev, V. A. Mazunov and Y. L. Sergeev, Akad. Izv. Nauk SSSR Ser. Khim. **6**,1337 (1984). (transl.: 1223)

[26] L. C. Ardini and T. P. Fehlner, Int. J. Mass. Spec. Ion Phys. **10**, 489 (1972).

[27] A. P. Hitchcock, A. T. Wen, S. Lee, jr. J. A. Glass, J. T. Spencer and P. A. Dowben, J. Phys. Chem. **97**, 8171 (1993).

[28] D. C. Allison, G. Johansson, C. J. Allan, U. Gelius, H. Siegbahn, J. Allison and K. Siegbahn, J. Electron Spectrosc. Relat. Phenom. **1**, 269 (1972).

[29] A. P. Hitchcock, S. G. Urquhart, A. T. Wen, A. L. D. Kilcoyne, T. Tyliszczak, E. Rühl, N. Kosugi, J. D. Bozek, J. T. Spencer, D. N. McIlroy and P. A. Dowben, J. Phys. Chem. B **101**, 3483 (1997).

[30] Y. J. Kime, D. C. Driscoll and P. A. Dowben, J. Chem. Soc. Faraday, Transactions II **83**, 403 (1987)

[31] D. C. Driscoll, J. A. Bishop, B. J. Sturm, P. A. Dowben and C. G. Olsen, J. Vac. Sci. Technol. A **4**, 823 (1986).

Chapter 5 The local structure of transition metal doped semiconducting boron carbides

The studies of various types of transition metal doping carborane compounds have been a fruitful area since the first metal-carborane sandwich complexes synthesized in 1965 [1-17]. The introduction of the transition metal has effectively influenced the structures, electronic and magnetic properties of the boron and carborane compounds. The doping of semiconducting boron carbides has been driven largely by device applications [4-12]. Plasma enhanced chemical vapor deposition (PECVD) has been an effective approach to fabricate metal doped semiconducting boron carbide, metalloborane and metallocarborane thin films without long-range crystalline ordering structure. For example, boron carbide homojunctions have been fabricated by PECVD of carboranes, with nickel doping [13,14], cobalt doping [15] and iron doping [16]. Indeed, nickel doping of boron carbide opened a route to the fabrication of the first boron carbide Esaki tunnel diode [13,14].

Successful n-type doping of ß- rhombohedral boron has been accomplished with dopants such as iron [18-21], vanadium [21], chromium [21], nickel [21], and cobalt [22]. For the related boron carbides, nickel [13,14,23,24] and iron [16] are certainly n-type dopants while cobalt may or may not [15] be a p-type dopant of the boron carbides, depending upon temperature. The common route for semiconducting doping is to include a metallocene, $M(C_5H_5)_2$, M=V, Cr, Mn, Fe, Co, Ni, simultaneously with the carborane source molecule, during plasma enhanced chemical vapor deposition

(PECVD) [13-16,23-24]. This chemistry provides a significant range of possible 3d transition metal dopants of boron carbide, but a unified picture of the possible differences (and similarities) in local structure and electronic structure adopted by each of these potential dopants in semiconducting boron carbide has not been developed.

Given that these potential 3d transition metal dopants of semiconducting boron carbide have a local magnetic moment, the local electronic structure in the vicinity of the dopant may also affect the local magnetic order, although this aspect remains as yet unexplored experimentally. This is an effort to bring a more unified picture to the local electronic structure of the doped semiconducting boron carbides fabricated by the plasma enhanced chemical vapor deposition (PECVD) of carboranes.

The historical challenge for theorists has been that the structure of the semiconducting boron carbides has not been unequivocally elucidated, although clearly it is complex based on some packing of icosahedra. As discussed here, some information about the local structure of the doped boron carbides has recently become available [15,25]. The local structure of the cobalt doped semiconducting boron carbide has been successfully characterized by extended X-ray absorption fine structure (EXAFS) and X-ray absorption near edge structure (XANES) spectroscopies [15,25] and to some extent in model cluster calculations [26]. XANES and EXAFS techniques did not prove to be very successful in the undoped boron carbides [27,28], though the extended electron energy loss fine structure has proved to be a

comparatively useful technique [29]. With metal doping, at least local structure in the vicinity of transition metal is now accessible. This opens a window to obtain the local structure of the semiconducting boron carbides using the 3d transition metal K-edge in extended X-ray absorption fine structure (EXAFS) spectroscopy.

The manganese and iron doped boron carbide films used for the X-ray absorption near edge structure (XANES) and extended X-ray absorption fine structure (EXAFS) measurements were produced using plasma enhanced chemical vapor deposition (PECVD) with orthocarborane (*closo*-1,2-dicarbadodecaborane; 1,2-$C_2B_{10}H_{12}$), ferrocene (for Fe), manganocene (for Mn) and argon as the plasma reactor gases, as previously described [13-16,23-25]. This PECVD approach is well established and has been successful in the fabrication of homojunction diodes [13-16,23-24]. The simulation and fitting of EXAFS results of manganese and iron doped boron carbide thin film using FEFF-6 codes were done using the structural parameters of Mn and Fe doped boron carbide generated by both semi-empirical and *ab initio* calculations for all tested molecule models, which have been compared with the measurements of cobalt doped boron carbide which has been done previously [15,25].

5.1 The Local structure of manganese doped boron carbide

Mn K-edge X-ray absorption near edge structure (XANES) and extended X-ray absorption fine structure (EXAFS) measurement has been performed for Mn doped plasma enhanced chemical vapor deposition (PECVD) grown semiconducting boron

carbides "$C_2B_{10}H_x$". The normalized Mn K-edge EXAFS spectrum of Mn-doped boron carbide is shown in Figure 5.1.

The characteristic signatures of manganese at value is close to the expected [30]

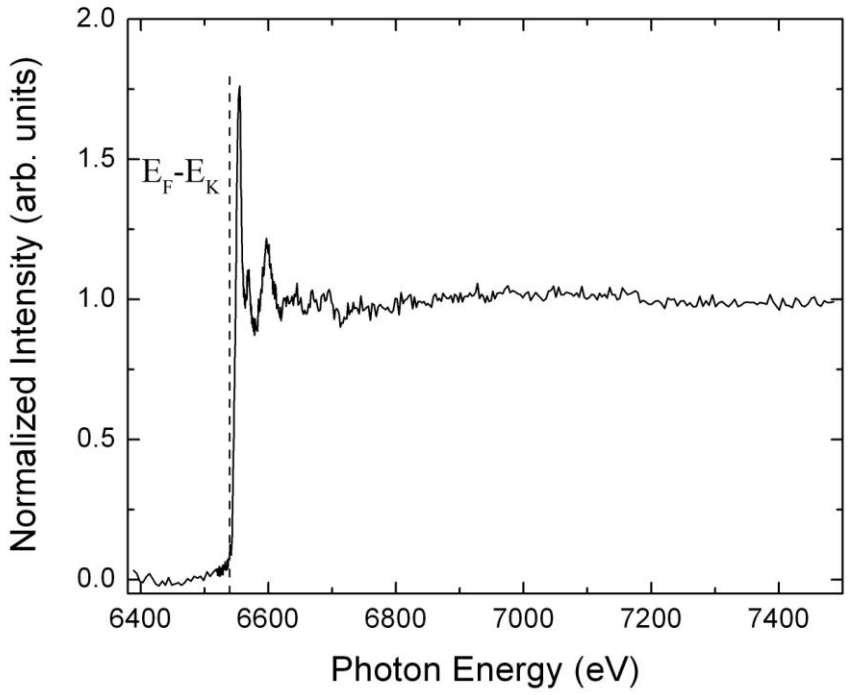

Figure 5.1. Normalized Mn K-edge XANES spectra of Mn doped PECVD semiconducting boron carbide. The Mn K-edge energy (E_F-E_K) at 6539 eV is highlighted, where E_K is the K-edge energy adapted from [30].

Mn K-edge energy (E_F-E_K) at 6539 eV. Therefore, we can infer from Figure 5.1 that manganocene source gases do result in manganese doping of the PECVD grown boron carbides. This establishes that the sublimed molecular vapors of the various metallocenes ($M(C_5H_5)_2$, M= Fe [16], Co [15,25], or Mn,), when added to the other plasma CVD sources gases, appear to behave in a similar fashion in delivering the

transition metal dopant during the plasma CVD process, although the similarities are in fact more significant as discussed below.

There are some distinctive features at the absorption edge of the Mn-doped boron carbide, indicating strong hybridization between iron and the inorganic host matrix. This is similar, in some respects, to that observed for the Co-doped plasma enhanced chemical vapor deposition (PECVD) grown "$C_2B_{10}H_x$" semiconducting boron carbides, using cobaltocene [15-16,23-25]. The K-edge absorption is perhaps strongest for the Mn-doped boron carbide (as compared with the Fe [16] or Co [15, 25] doped semiconducting PECVD boron carbide).

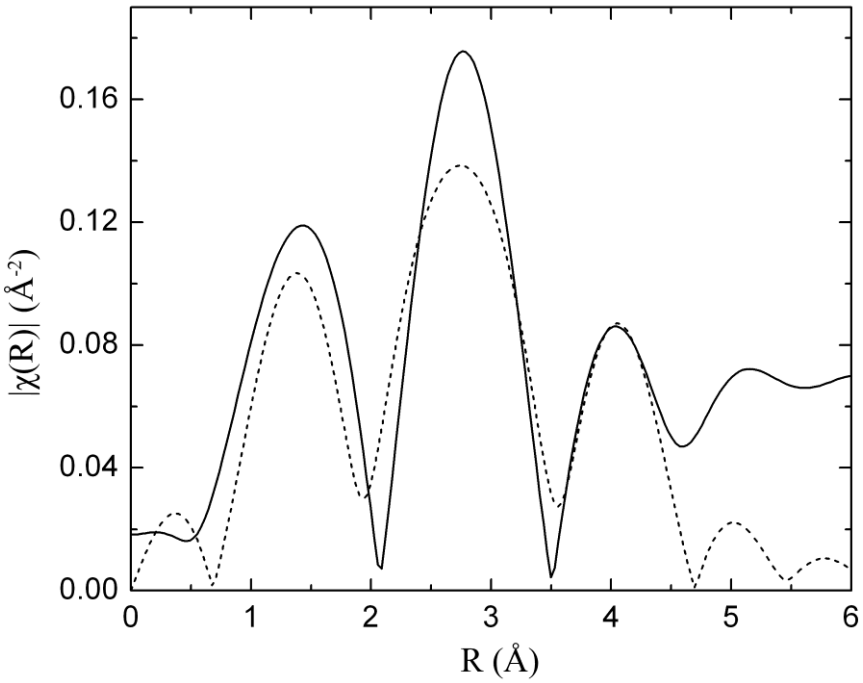

Figure 5.2. Magnitude of the Fourier transformed EXAFS $k\chi(k)$ data for the manganese doped PECVD semiconducting boron carbide are compared with the theoretical Fourier transformed EXAFS $k\chi(k)$ (broken line), using the schematic model of Figure 5.4. The data are transformed for data taken between 4 and 8 $Å^{-1}$.

The EXAFS data was reduced according to the standard procedure [31] and analyzed by the FEFF-6 codes. The EXAFS data was first reduced by subtracting the background absorption, and then normalized as described in equation (3) in chapter 3. Data analysis can be performed in either in real space and k space. Real space analysis is to use the Fourier transform of the EXAFS. The Fourier transformed EXAFS wave vector weighted $k\chi(k)$ data, in radial coordinates was obtained for Mn (solid line in Figure 5.2). The radial positions of peaks represent the distance between the absorbing Mn atom and their near neighbors within 6 Å. This makes possible acquisition of some structural and geometrical information of Mn doped boron carbides at a local level. The amplitude gives a qualitative description of the number of neighbors, and provides an overall sense of the local order.

Major peak at 1.4 Å is due to single-scattering contribution of Mn-B(C) (Figure 5.3) pairs as nearest neighbors. Peaks observed between 1.96 to 4.6 Å are due to Mn-X pairs (X could be any of light scatters, such as B, C, N, O) and multiple scattering contributions. The peak at 4 Å corresponds to another Mn-B(C) pairs with longer distance from the Mn or Fe atom. The feature at about 5.2 Å is associated with the Mn-Mn pairs.

The structural parameters of Mn doped boron carbide were generated by both semi-empirical and ab-initio calculations for all tested molecule models to simulate EXAFS using FEFF-6 codes. Geometry optimization was performed for a number of possible structural models by obtaining the lowest unrestricted Hartree-Fock energy

states. Similar to the prior studies with cobalt doping of semiconducting boron carbides [15,25], a number of local structural cluster models were tested for fit to the experimental EXAFS data.

Among the tested models, the best fit of the unfiltered EXAFS data is from the

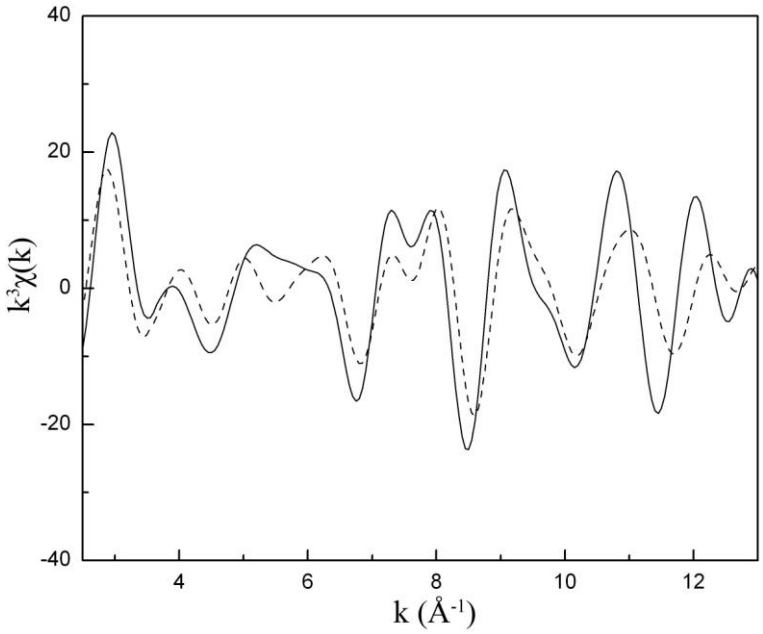

Figure 5.3. EXAFS spectrum in k-space (solid line) with factor k^3 within range from 3.2-13 $Å^{-1}$ using the schematic model of Figure 5.4.

model that two adjoined icosahedral cages with Mn atom sitting in the apical icosahedral sites, possibly at a boron or carbon site for each cage, as schematically shown in Figure 5.4. The separation between two paired Mn was found to be close to 5.15±0.03 Å. We find that this model (Figure 5.4), involving transition metal atom Mn-Mn pairs sitting in the apical sites on opposite sides of the adjacent icosahedra, reasonably account for all major features shown in the EXAFS spectra Mn doped

PECVD semiconducting boron carbides. The fairly good fitting has been also shown in k-space fitting in the range from 3.5 to 13 $Å^{-1}$ as seen in Figure 5.3 corresponding in R space in Figure 5.2. The difference in magnitudes between the experimental and modeling curves mainly reflects low concentration of manganese in the studied material. Other tested models, in which the metal atoms are not paired, do not show agreement with the experimental data, especially in the region corresponding to lattice constants greater than 3 Å. This effect was noted previously in the studies of cobalt doped boron carbides [15,25].

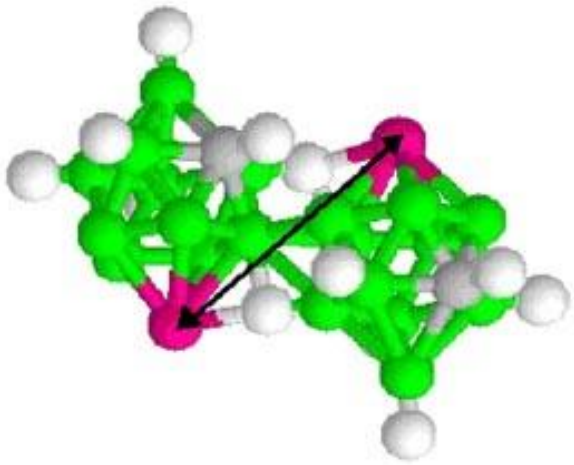

Figure 5.4. Schematic of the transition metal capped co-joined icosahedra structures with a metal to C distance of about 2Å to satisfy the EXAFS derived results. The transition metal atoms sit on opposite sides in the apical sites on the adjacent icosahedra, with a metal to metal distance (indicated by the arrow) chosen again to fit the EXAFS derived results.

5.2 The local structure of ion doped boron carbide

Fe K-edge X-ray absorption near edge structure (XANES) and extended X-ray absorption fine structure (EXAFS) measurement has been performed for Fe doped plasma enhanced chemical vapor deposition (PECVD) grown semiconducting boron carbides "$C_2B_{10}H_x$" in a similar way as the measurements on Mn doped boron carbide. The characteristic signatures of manganese and iron are evident at values close to the expected [30] Fe K-edge energy (E_F-E_K) at 7112 eV (Figure 5.5). It suggests that

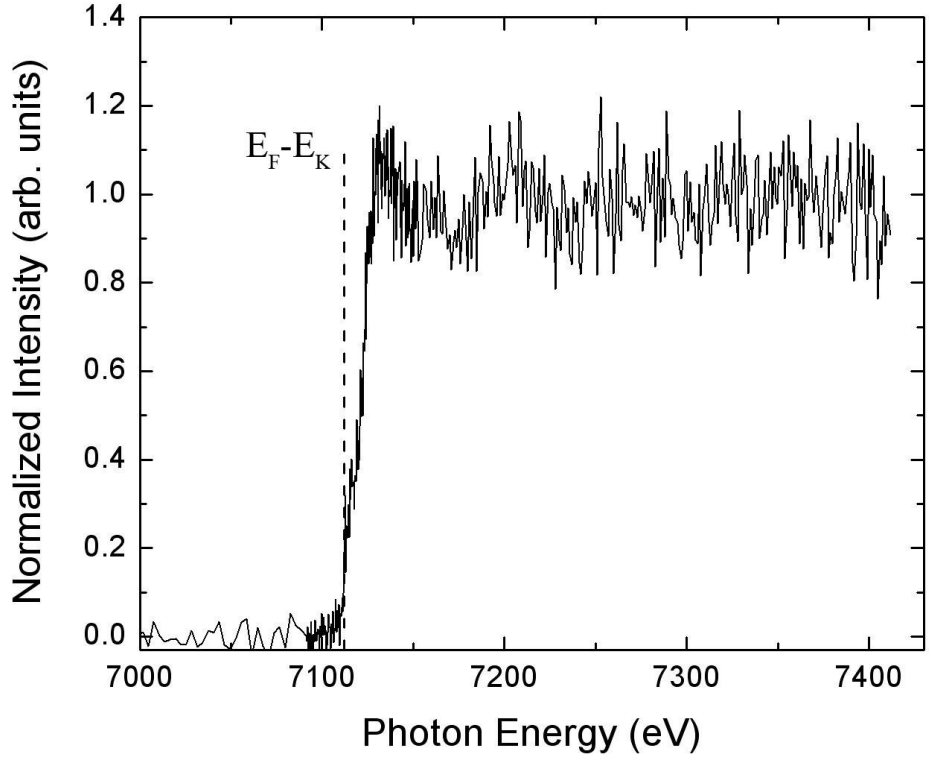

Figure 5.5. Normalized Fe K-edge XANES spectra of Fe doped PECVD semiconducting boron carbides. The Fe K-edge energy (E_F-E_K) at 7112 eV is highlighted, where E_K is the K-edge energy adapted from [30].

ferrocene source gases do result in iron doping of the PECVD grown boron carbides. The distinctive features at the absorption edge of the Fe-doped boron carbide,

indicating strong hybridization between iron and the inorganic host matrix, similar to the observation of Mn doped case. The less clear features compared with Mn doped boron carbide EXAFS spectrum may indicate the lower concentration of Fe in the Fe doped boron carbide sample. The normalized Fe K-edge EXAFS spectrum of Fe-doped boron carbide is shown in Figure 5.5.

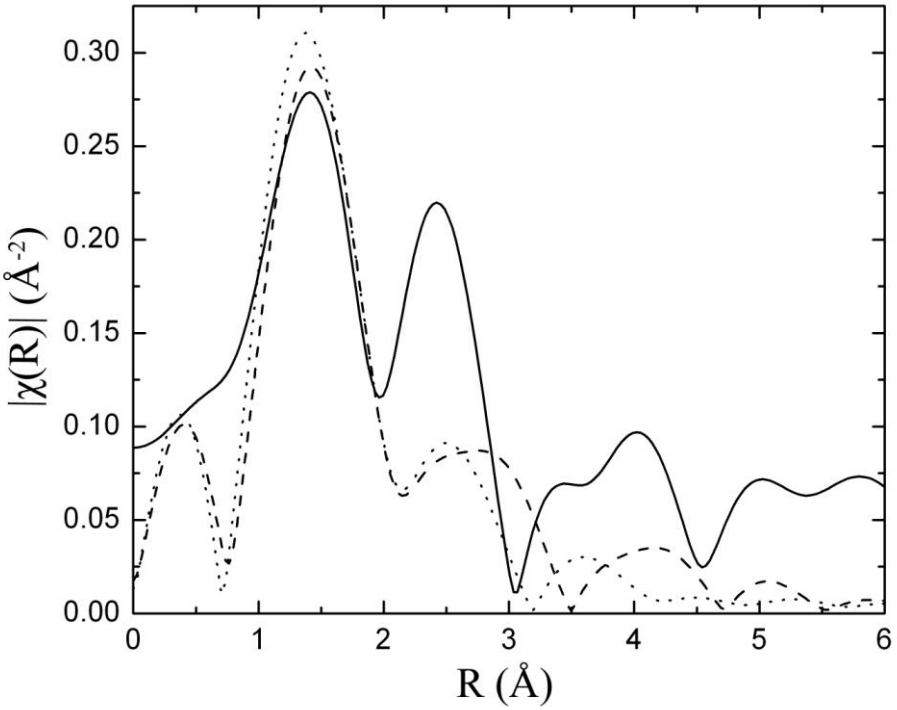

Figure 5.6. Magnitude of the Fourier transformed EXAFS $k\chi(k)$ data for the iron doped PECVD semiconducting boron carbide are compared with the theoretical Fourier transformed EXAFS $k\chi(k)$ (broken line), using the schematic model of Figure 5.4. The fitting using other molecular model where single Fe atom is in the vicinity of two octahedral cages is shown as dot line for comparison. The data are transformed for data taken between 2 and 6.46 $Å^{-1}$.

The procedure to deduce and analyze the EXAFS data for Fe doped boron carbide is the same as the steps for Mn doped sample. A magnitude of the Fourier transformed EXAFS $k\chi(k)$ data of Fe doped sample in radial coordinates was shown Figure 6. The radial positions of peaks represent the distance between the absorbing Fe atom and its near neighbors within 6 Å. The major feature at 1.4 Å is due to single-scattering contribution of Fe-B(C) pairs as nearest neighbors. Peaks observed between 1.96 to 4.5 Å are due to Fe-X pairs (where X could be any of the light scatters, such as B, C, N, O, although we can exclude the impurities such as N and O from the XPS studies) and multiple scattering contributions. The peak at 4 Å corresponds to another Mn-B(C) Fe-B(C) pairs with longer distance from the Mn or Fe atom. The feature at about 5 Å is associated with the Fe-Fe pairs.

The structural parameters of Fe doped boron carbide were generated by both semi-empirical and *ab initio* calculations for all tested molecule models to simulate EXAFS using FEFF-6 codes. Similar to studies with Mn doping of semiconducting boron carbides, a number of local structural cluster models were tested for fit to the experimental EXAFS data. The best fit of the unfiltered EXAFS data is from the model that two adjoined icosahedral cages with Fe atom sitting in the apical icosahedral sites, which in consistent with Mn doped boron carbide fit, as schematically shown in Figure 5.4. The separation between two paired Fe ions is about 5.03 ± 0.03 Å. This model (Figure 5.4) again involving transition metal atom Fe-Fe pairs sitting in the apical sites on opposite sides of the adjacent icosahedra,

reasonably account for all major features shown in the EXAFS spectra for ion doped PECVD semiconducting boron carbides.

5.3 Comparison of EXAFS for Mn, Fe, Co doped semiconducting boron carbide

Compared with the case of cobalt doped boron carbides, it is fairly clear, just from visual inspection, that the local order about the Mn or Fe transition metal atoms in semiconducting boron carbide is greater than previously observed for cobalt doping of PECVD semiconducting boron carbide (Figure 5.7) [15,25]. In the case of the latter, the nearest neighbour and next nearest neighbour shells about the transition metal have strong components, but weaken dramatically with increasing radius compared with Fe, and particularly Mn-doped semiconducting boron carbides.

The distance for single-scattering contribution of both the Mn-B(C) pairs and Fe-B(C) pairs is about 1.4 Å, smaller than the cobalt case (1.8 Å). This suggests that the manganese and iron atoms prefer to sit in the icosahedral apical sites in positions much closer to the boron and carbon atoms than is the case for cobalt. This tends to indicate the greater stability of the Mn and Fe doped boron carbide structures and stronger bonds formed between B(C) and either Mn or Fe atoms. In all three transition doped boron carbide, the modeling of the EXAFS data favors the formation of metal-metal pairs to an even greater extent with Mn and Fe doping, but in all cases the peak location for Mn-Mn, Fe-Fe and Co-Co pairs are all very close, at about 5 Å.

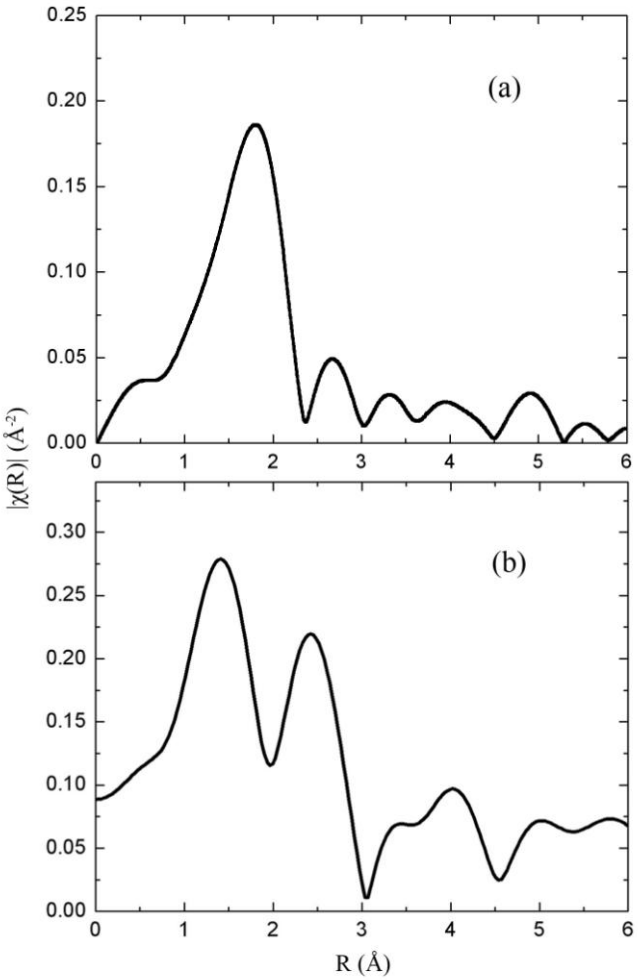

Figure 5.7. Magnitude of the Fourier transformed EXAFS $k\chi(k)$ data for (b) the iron doped PECVD semiconducting boron carbides respectively are compared with (a) that of cobalt doped PECVD semiconducting boron carbide.

The *ab initio* Co K-edge XANES [15,25] and Co, Fe and Mn EXAFS spectra simulations suggest that all three transition metals adopt an endohedral position occupying an apical position within the icosahedral cage, as indicated in Figures 5.4 and 5.8, giving the transition atom a five-fold coordination to the *nido*-carborane CB_{11} cage. This is very much like a number of known metalloboranes [32]. In

metalloborane examples, there is a conversion of adjacent icosahedra by removal of a B, BH, C or CH vertex, followed by introduction of the $M(C_5H_5)$ vertex [32,33]. This should be a facile reaction [32]. Given the structural similarities among all three transition metal doped semiconducting PECVD boron carbides, we can make now some estimates of electronic structure, at least in the region of the transition metal dopant from *ab initio* theory. Two approaches are possible: cluster calculations using M_2-$C_2B_{20}H_{18}$ clusters (M=Ti, V, Cr, Mn, Fe, Co, Ni, and Cu), as were used to help solve and fit the EXAFS data, or chains of doped icosahedra with periodic boundary conditions.

5.4 The local electronic structure and likely local spin configurations for the transition metal doped semiconducting boron carbides

The theoretical calculations of electronic structures and local spin configurations for transition metal doped semiconducting boron carbide, Ti through to Cu, were contributed by collaborators with theory expertise [34]. As stated in theoretical papers, all the first-principles calculations are performed in the framework of density functional theory as implemented in the $DMol^3$ code [35,36]. The PW91 generalized gradient approximation (GGA) was used for the exchange-correlation functional because of the better performance of GGA than the local density approximation (LDA) in many molecular systems. All the electrons were considered equally, and the double numerical plus polarization (DNP) basis set, which is comparable to the $6\text{-}31G^{**}$ basis

set, was used. The convergence tolerance for the self-consistent field is 2.72×10^{-6} eV, and the structures were optimized till the maximum force is below 0.054 eV/Å. To explore the possible magnetic ordering configurations, different initial spin states of the transition metal atoms in the spin-polarized calculated model systems were considered and optimized. Where possible, the electronic structure and spin configuration for metal atom pairs on the same (UU) and opposite sides (UD) of the adjacent icosahedra for both the infinite chain structures with periodic boundary conditions, i.e. M_2-$C_2B_{20}H_{14}$ (M= Ti, V, Mn, Fe) and the clusters M_2-$C_2B_{20}H_{18}$ (M=Ti, V, Cr, Mn, Fe, Co, Ni, and Cu) were calculated. These are schematically shown in Figure 5.8.

It is found that energetically the transition metal atoms prefer to situate at the alternate sides of the chain or symmetric axis when in molecular clusters, as summarized in Table 5.1. This is in good agreement with our experimentally derived local structure (Figure 5.4). The differences in energy between the unfavourable structure placing the transition metals on the same side (UU) and favourable structures placing the transition metals on opposite sides (UD) of the adjacent icosahedra vary from 0.3 to 0.5 eV regardless of spin configurations.

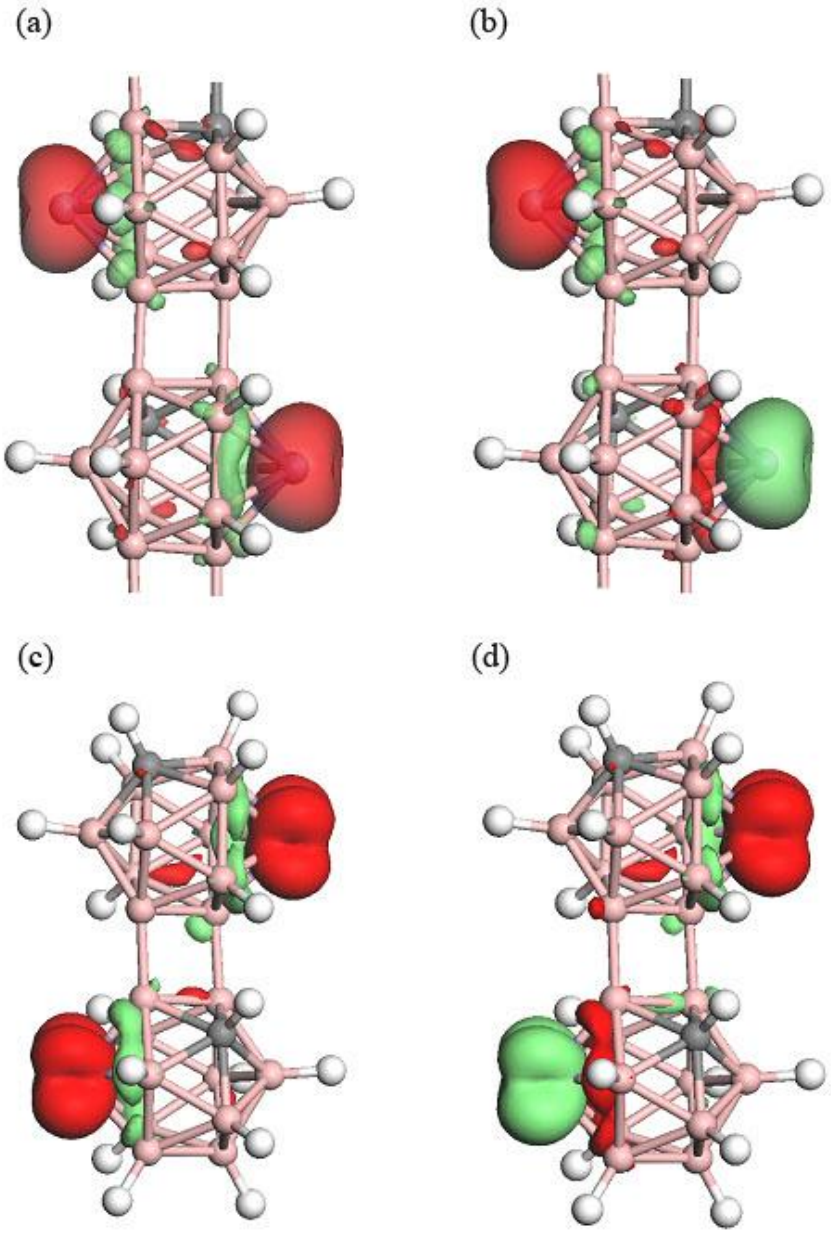

Figure 5.8. The spin distribution on the optimized structure with an isovalue of 0.0179 a.u. of the stable ferromagnetic high spin (a,c) and less stable low spin (b,d) configuration of metal pairs on the same (UU) and opposite sides (UD) of the adjacent icosahedra for both the infinite chains structures with periodic boundary conditions, i.e. Fe_2-$C_2B_{20}H_{14}$ (as shown in (a) and (b)) and the clusters Fe_2-$C_2B_{20}H_{18}$ (as shown in (c) and (d)).

Metal	E_{uu}-E_{ud} (eV)	$E_{high\ spin}$-$E_{low\ spin}$ (eV)	Average Magnetic Momentum (μ_B)
Ti	0.46 (0.32)	-0.002 (0.00)	0.85 (1.05)
V	0.59 (0.34)	-0.02 (-0.02)	2.15 (2.2)
Mn	0.78 (0.51)	0.003 (0.13)	3.45 (3.2)
Fe	1.1 (0.44)	-0.24 (-0.01)	1.1 (1.1)
Cr	(0.36)	(-0.03)	(3.3)
Co	(0.59)	non-magnetic spin configuration	non-magnetic spin configuration
Ni	(0.51)	non-magnetic spin configuration	non magnetic spin configuration
Cu	(0.08)	non-magnetic spin configuration	non-magnetic spin configuration

Table 5.1. Total energy difference (eV) between stable structures with metal pairs on the same (E_{uu}) and opposite sides (E_{ud}) of theadjacent icosahedra for both the infinite chain structures with periodic boundary conditions, i.e. M_2–$C_2B_{20}H_{14}$ (M = Ti, V, Mn and Fe) and the clusters M_2–$C_2B_{20}H_{18}$ (M = Ti, V, Cr, Mn, Fe, Co, Ni and Cu), as shown in Figure 5.8, with the latter values in brackets ( ). The total energy difference (eV) between the high- and low-spin configurations and average magnetic moment magnitude (μB) per atom with the metal pairs on the opposite sides of the adjacent icosahedra for both the M_2–$C_2B_{20}H_{14}$(M = Ti, V, Mn and Fe) infinite chains and M_2–$C_2B_{20}H_{18}$(M = Ti, V, Mn, Fe Cr, Co, Ni and Cu) molecular clusters have also been tabulated with the latter numbers again in brackets ( ).

From spin-polarized calculations, it shows that Fe favor the high-spin stable ground states, i.e. the spins are roughly aligned in the same direction and the net spin

magnetic moments on the transition metal atoms are nonzero. For Co, Ni, and Cu, non-magnetic states are adopted where not only are the net magnetic moments zero, but the systems are entirely non-magnetic with no local magnetic order at all. This situation observed for Co, Ni, and Cu was contributed to the hybridization between the more than half-filled d-shell and s-levels. Such hybridization effects have been suggested to result in reduced magnetic moments in Co and Ni clusters [37] and thus are not entirely unexpected.

The atomic charges of all the carborane cluster and carborane chain systems, with 3d transition metal substitutions, were analyzed by using the Hirshfeld method (as implemented in DMol3), which has been shown to give chemically meaningful results [38]. The detailed average electron charges for the metal pairs on opposite sides of the adjacent icosahedra for both the clusters M_2–$C_2B_{20}H_{18}$ (M = Ti, V, Cr, Mn, Fe, Co, Ni and Cu) and infinite chain structures with periodic boundary conditions, i.e. M_2–$C_2B_{20}H_{14}$ (M = Ti, V, Cr, Mn, Fe, Co, Ni and Cu) are summarized in Table 5.2. The calculated average atomic charges differ little between the high- and low-spin configurations as calculated by the Hirshfeld method [38]. For comparison, the results by using the Mulliken method are also listed. Generally, the average charge state on each transition metal is in the range of 0.3–0.6 |e|, which suggests that the transition metal generally adopts a covalently bonded like scenario.

The bond lengths of the five M-B bonds are calculated for different spin configurations. There are very small differences δL in the M-B bond lengths between

	Cluster		Chain	
Transition Metal	Atomic charge (|e|) of the high spin state	Atomic charge (|e|) of the low spin state	Atomic charge (|e|) of the high spin state	Atomic charge (|e|) of the low spin state
Ti	0.652 (0.534)	0.652 (0.534)	0.617 (0.454)	0.617 (0.454)
V	0.559 (0.408)	0.561 (0.409)	0.541 (0.364)	0.541 (0.365)
Cr	0.659 (0.266)	0.659 (0.267)	0.643 (0.219)	0.644 (0.220)
Mn	0.445 (0.241)	0.480 (0.271)	0.444 (0.251)	0.442 (0.243)
Fe	0.388 (0.297)	0.389 (0.298)	0.379 (0.273)	0.386 (0.285)
Co	0.331 (0.077)		0.381 (0.033)	
Ni	0.291 (0.248)		0.281 (0.220)	
Cu	0.483 (0.109)		0.459 (0.018)	

Table 5.2. The average atomic charges for the metal pairs on opposite sides of the adjacent icosahedra for both the clusters M_2–$C_2B_{20}H_{18}$ (M = Ti, V, Cr, Mn, Fe, Co, Ni and Cu) and infinite chain structures with periodic boundary conditions, i.e. M_2–$C_2B_{20}H_{14}$ (M = Ti, V, Cr, Mn, Fe, Co, Ni and Cu), as shown in Figure 5.8. The average atomic charges calculated differ little between the high- and low-spin configurations as calculated by the Hirshfeld method [38] and again by the Mulliken method, shown in brackets ( ).

the high and low spin configurations for Ti, V, Cr, Mn, and Fe, as listed in Table 5.3. While these bond length differences δL are slight for some transition metal systems, there are differences nonetheless. It indicated that strong connection between the stable structures and the bond lengths that do depend upon the local spin configuration for Mn doped clusters and chains. The bond length differences between the transition metal atoms and nearby boron atoms in the high and low-spin ground

M	High-spin	Low-spin	δL (Å)
Ti	2.184	2.181	0.003
V	2.152	2.156	-0.004
Cr	2.157	2.162	-0.005
Mn	2.087	2.210	-0.123
Fe	2.009	2.017	-0.008
Co	2.020	2.020	0
Ni	2.058	2.058	0
Cu	2.236	2.236	0

Table 5.3. The *M*–B bond and maximum length difference, *δ*L, between the high- and low-spin states of M_2–$C_2B_{20}H_{18}$.

states are very similar for all cases, with the maximum δL ranging at most from 0.004 to 0.009 Å, for Ti, V, Cr, and Fe. However, in the case of Mn, δL is as large as 0.123 Å. In the nonmagnetic systems containing Co, Ni, and Cu, only an average bond length can be cited. Accordingly, we may expect slightly different fits to the experimental structural data from EXAFS for Ti, V, Cr, Mn and Fe doped PECVD semiconducting boron carbides, depending on the model spin configuration used, as indicated in Figure 5.9. The fitting curves with the high net spin and low net spin configuration are mostly overlapped in the radial distance region corresponding to single scattering pathways between Fe and B(C). Since the structure parameters for high net spin and low net spin states are quite close, the radial positions of peaks are almost the same. The variation of the scattering amplitude occurs in the range from 2

Å to 4.25 Å dominated by multiple scattering effects probably due to the slight change of bridging angle in multiple scattering pathways [39].

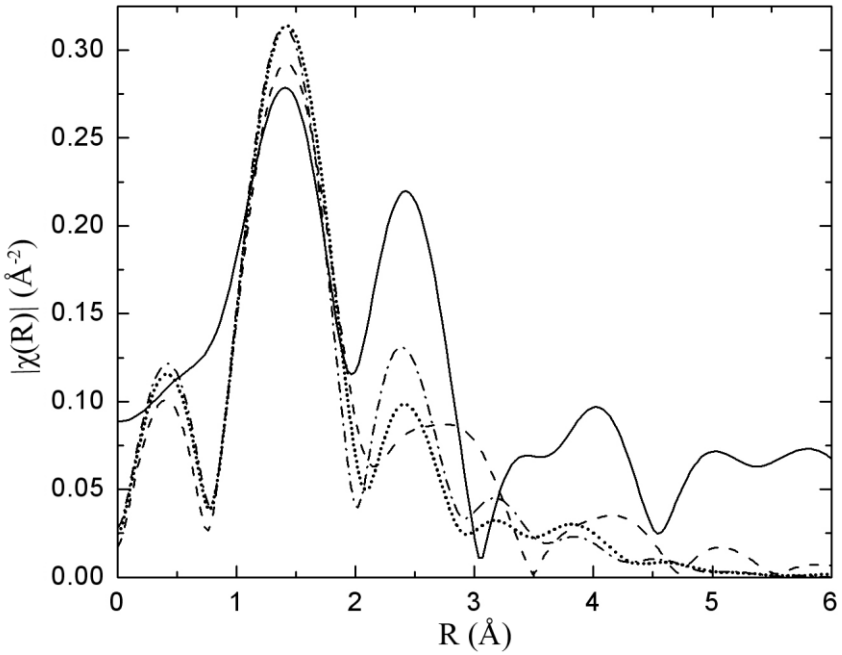

Figure 5.9. Comparison of the theoretical modeling of the Fourier transformed EXAFS of the iron doped PECVD semiconducting boron carbide. The magnitude of the Fourier transformed experimental EXAFS is shown as a solid line. The fitting curves are based on structural parameters calculated by semi-empirical calculation (dashed line) and density functional theory calculations with both the high-spin (dotted line) and low-spin (dash dot line) configurations, see text.

Of course, for the PECVD grown semiconducting boron carbides, the transition metal atoms are very likely to be more highly coordinated than in the models of Figure 5.8. We can expect that the greater coordination that is likely to occur in the

semiconducting solid material will also result is changes to bond length as well as diminish any differences in the bond lengths between the high spin and low spin configurations. Generally, the M-B(C) bond lengths obtained from theory are in the region of 2 Å, as expected from the analysis of the EXAFS experiments, although somewhat larger as summarized in Table 5.2. Again, this is expected for a metal atom that might not be as fully coordinated as may occur in the solid boron carbide semiconductor.

5.5 Characteristics of chromium doped semiconducting boron carbide thin films

The local spin configuration and band structure of chromium doped boron carbide calculated by density functional theory suggests local magnetic ordering. While the long range dopant position appears random in the boron carbide semiconductor, the local position and initial empirical/computational results suggest the promise of large magneto-resistive effects.

The efforts to characterize Cr doping boron carbide thin film by using I-V curves and measurement of temperature dependence of magnetic moment is a starting point to explore the magneto-electric property of this material which may have potential to make new co-tunneling barrier of magnetic tunnel junction and other spintronic devices

5.5.1 Local electronic structure and spin configuration of Cr doped semiconducting boron carbide

The predicted local structure and spin configuration of Cr doped semiconducting boron carbide in chain system are shown in Figure 1. From spin polarized calculation, Cr favors the state that the spins are roughly aligned in the same direction and the net spin magnetic moment on the Cr atoms is nonzero or at maxima [34]. This is similar to the expectations for Ti, V and Fe doping of semiconducting boron carbides [34].

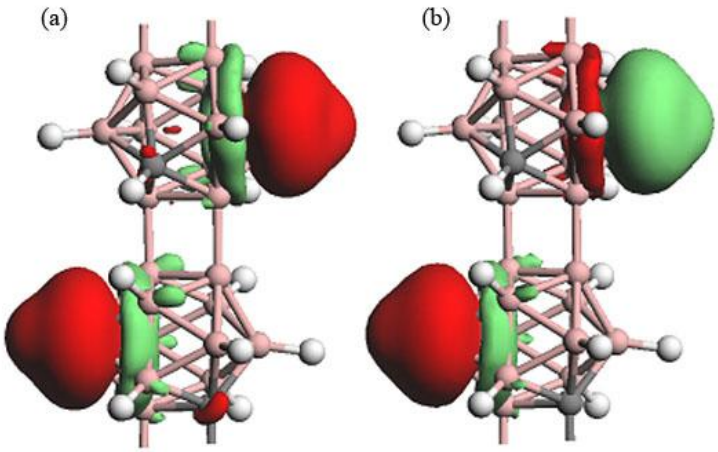

Figure 5.10. Optimized structure with spin distributions of Cr_2–$C_2B_{20}H_{14}$ (isovalue is chosen to be 0.0179 a.u.) of the stable ferromagnetic high spin (a) and less stable low spin (b) configurations. Chromium metal pairs are placed on the opposite sides of adjacent icosahedra for the infinite periodic chain, based on local structural information obtained for a number of transition metal doped boron carbides [34].

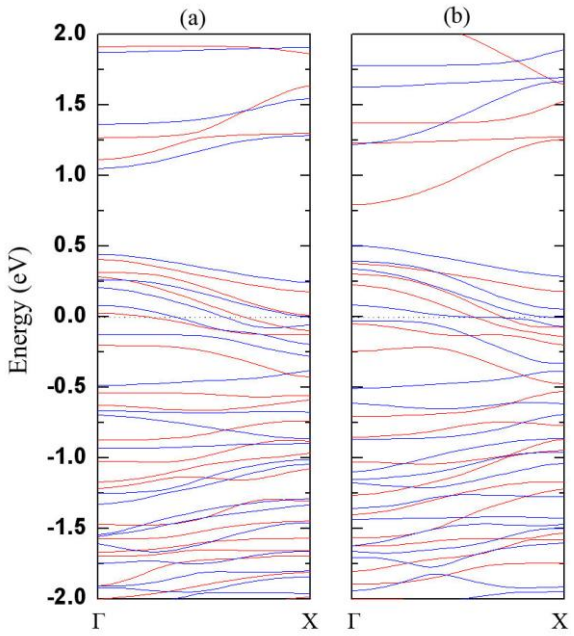

Figure 5.11. The band structures of the infinite periodic Cr_2–$C_2B_{20}H_{14}$ chain with two metal atoms placed on opposite sides of the chain. Plotted are both the spin-polarized ground state band structures from Brillouin zone center to zone edge for both the high net spin momentum (a) and the low net spin momentum (b). The red and blue curves are majority- and minority-spin bands, respectively, and binding energies are plotted with respect to $E-E_F$ in (eV), so that occupied states hold negative values [34].

The band structure of the infinite chain system Cr_2-$C_2B_{20}H_{14}$ for both states with high and low net spin momentum is shown in Figure 2. The Cr_2-$C_2B_{20}H_{14}$ appears to be metallic, as indicated by the band crossing of the Fermi level for both high and low spin momentum states. Given that the chain structure modeling represent much higher concentration than the real Cr doped boron carbide thin film sample whose concentration is about 2-5% (atomic percent), it may be that the states are more

localized than in this model calculation, i.e. the states near the Fermi level little band width and limited dispersion. Thus chromium doping may only place the states in the vicinity of the Fermi level and contribute to a hopping conduction channel. This is born out by the transport measurements.

5.5.2 I-V characteristics and temperature dependent magnetic property of Cr doped semiconducting boron carbide thin film

The I-V characteristics of chromium doped semiconducting boron carbide thin film were measured at room temperature, as indicated in Figure 5.12. We observed a hysteresis in the current with the direction of the applied voltage bias. The positive voltage bias applied from lower value to higher value results in generally higher resistance states than the resistance measured in reverse direction. Semiconducting boron carbides are highly resistive and diode devices made from boron carbide have long been know to exhibit hysteretic behavior consistent with an effective capacitance or diode in series with a resistor [40]. While not unexpected, neither the hysteresis, nor the non linear behavior of the I(V) curves suggest metallic behavior – in fact these chromium doped boron carbide films are either dielectrics or semiconductors.

It is interesting to note that resistance represented by I-V characteristics depends on the polarity of applied voltage bias. The mechanisms of this polarity of voltage dependent resistance changing phenomenon observed in Cr doped boron carbide thin film is still not fully explored, but the asymmetric conductance, obtained by applying

positive and negative voltage bias separately, is indicative of either a magneto-electric effect or a ferroelectric effect. Though local electric dipoles within the film are likely [34], global polarization is not very likely at all, though cannot at present be excluded. This is consistent with the sudden increases in current in the high resistance state (Figure 5.12), as such behavior could be caused by weak charge trapping states.

There is increased resistance and lower currents measured when a magnetic field is applied, as seen in Figure 5.12. The main features of the I-V characteristics measured at 8000 Gauss magnetic field are similar to the ones obtained without magnetic field, but both the currents and hysteresis decrease. We observe a resistance

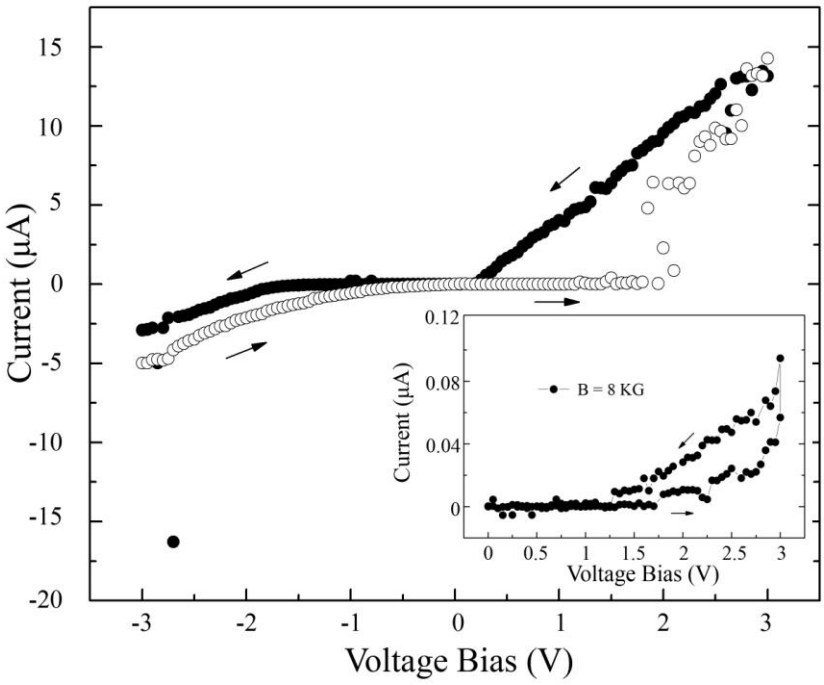

Figure 5.12. The I-V characteristics of Cr doped semiconducting thin film at room temperature measurement with applied voltage bias from +3 V to -3 V (black dots) and -3 V to +3 V (black circles). The I-V curve taken at 8 KG magnetic field shown at inset.

over 100 times greater in the range from +1 V to +3 V when 8 kGauss magnetic field was applied.

Because of the likely local structure in the vicinity of the chromium dopants, which involve both a local polarization and spin, it may well be that Cr doped semiconducting boron carbides represent a possible magneto-electric glass, as identified in other local moment materials [41-44]. Both the model calculations and the decrease in hysteresis in the I(V) curves suggest that this is a possibility worth pursuing.

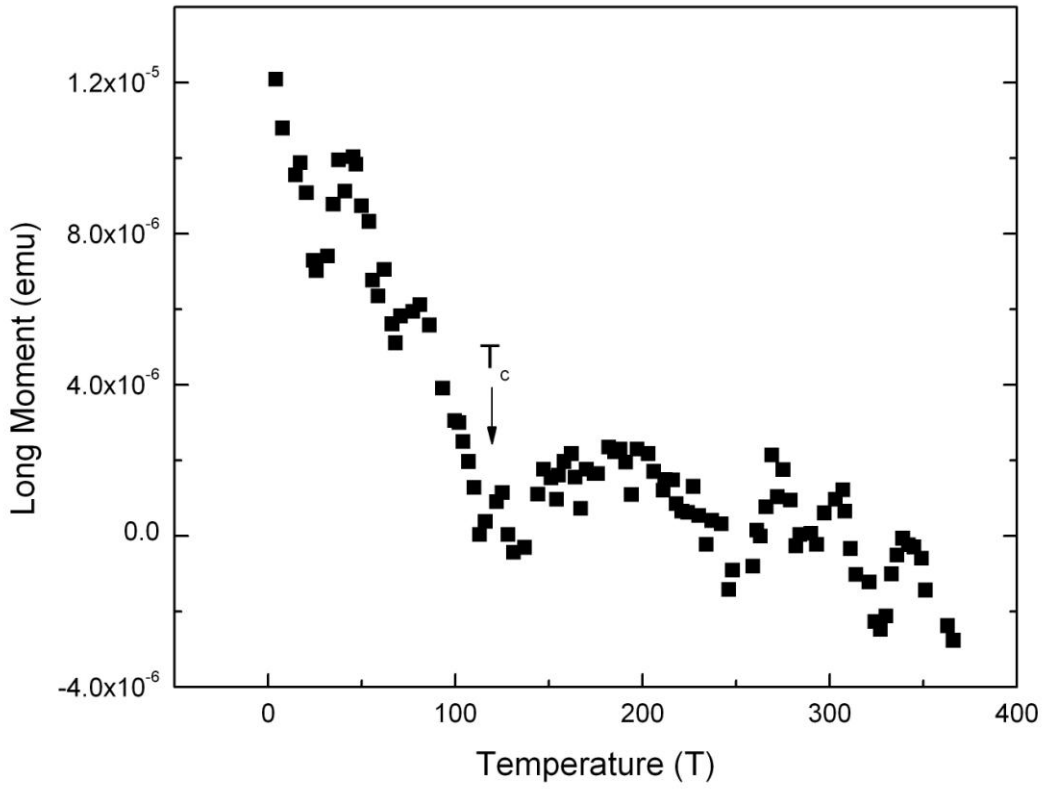

Figure 5.13. Temperature dependence of magnetic moment with magnetic field 5 kGauss for Cr doped boron carbide thin film. The temperature ranges from 4 K to 370 K.

In order to obtain the information of magnetic moment for Cr doped boron carbide thin film, the temperature dependence of magnetic moment measurement was carried out in the 4-370 K temperature range with magnetic field (5 kGauss) using superconducting quantum interference device (SQUID). As it is shown in Figure 5.13, the magnetic moment significantly decreases, with a critical temperature of 120 K.

5.6 Conclusion and implications for the future

From the analysis of Mn and Fe K edge XANES and EXAFS spectra, there are indications that the manganese and iron atoms are chemically bonded within icosahedral boron-carbide cages of PECVD grown semiconducting boron carbides, in a similar fashion to that observed for cobalt doping of PECVD grown semiconducting boron carbides. In all three transition metal samples for the doping of semiconducting boron carbides, the doping occurs pairwise with each transition metal sitting on adjacent adjoined icosahedral cages with a metal to metal spacing of about 5 Å. This observation is consistent with theory, while the adoption of an apical endohedral position within the cage, by the various transition metals, is consistent with known main group metalloborane synthetic chemistry [32,33]. The spin density calculations indicate that Mn prefers a low spin antiferromagnetic configuration, and Co, Ni, and Cu adopt local non-magnetic spin configurations.

The theoretical modeling of Cr doped boron carbide indicates that the Cr atoms prefer to occupy the apical position on the opposite sides of icosahedral cages and

adopt high net spin (locally ferro or ferri magnetic) state, and this seems to clearly occur below 120K. Although the mechanism for the observed magnetoresistance is as yet clear, both theory and experiment suggest that some chromium doped boron carbides might either imitate or act as a magneto-electric glass. The temperature dependent measurement of magnetic moment showed a critical temperature of 120 K.

The studies of electronic and magnetic properties of Cr doped boron carbide thin film just started, further efforts are needed to explore the magnetic properties in details. It is interesting to examine whether Cr doped boron carbide is suitable for spintronic applications, as suggested by other transition metal doped materials [45].

The surface sensitive tools like X-ray photoemission, ultraviolet photoemission and inverse photoemission spectra can provide the information of electronic structure for Cr doped boron carbide. It is important for setting up a more completed connection between the electronic structure and the physical properties for transition metal doping. The question of how the concentration of dopant Cr affects the conductivity and magnetic property leaves for research. The potential for using Cr doped boron carbide to fabricate a new homojunction diode exists, like Fe, Ni, Co dopants.

Reference:

[1] M. F. Hawthorne, D. C. Young, and P. A. Wegner, J. Am. Chem. Soc. **87**, 1818 (1965); M. F. Hawthorne, D. C. Young, T. D. Andrews, D. V. Howe, R. L. Pilling, A. D. Pitts, M. Reintjes, L. F. Warren Jr., and P. A. Wegner, J. Am. Chem. Soc. **90,** 879 (1968).

[2] D. A. Owen, and M. F. Hawthorne, J. Am. Chem. Soc. **92**, 3194 (1970); D. A. Owen, and M. F. Hawthorne, J. Am. Chem. Soc. **93**, 873 (1971); D. E. Harwell, J. McMillan, C. B. Knobler, and M. F. Hawthorne, Inorg. Chem. **36**, 5951 (1997).

[3] M. F. Hawthorne, L. F. Warren Jr., K. P. Callahan, and N. F. Travers, J. Am. Chem. Soc. **93**, 2407 (1971); H. C. Kang, S. S. Lee, C. B. Knobler, and M. F. Hawthorne, Inorg. Chem. **30**, 2024 (1991).

[4] B. W. Robertson, S. Adenwalla, A. Harken, P. Welsch, J. I. Brand, P. A. Dowben, and J. P. Claassen, Appl. Phys. Lett. **80**, 3644 (2002).

[5] B. W. Robertson, S. Adenwalla, A. Harken, P. Welsch, J. I. Brand, J. P. Claassen, N. M. Boag, and P. A. Dowben, Advances in Neutron Scattering Instrumentation, I. S. Anderson, B. Guérard, Eds.; Proc. SPIE **4785**, 226 (2002).

[6] S. Adenwalla, R. Billa, J. I. Brand, E. Day, M. J. Diaz, A. Harken, A. McMullen-Gunn, R. Padmanabhan, and B.W. Robertson, Penetrating Radiation Systems and Applications V, Proc. SPIE **5199**, 70 (2003).

[7] C. Lundstedt, A. Harken, E. Day, B. W. Robertson, and S. Adenwalla, Nucl. Instrum. Methods in Phys. Res. A **562**, 380 (2006).

[8] A. D. Harken, E.E. Day, B. W. Robertson, and S. Adenwalla, Jap. J. Appl. Phys. **44**, 444 (2005).

[9] A. N. Caruso, R. B. Billa, S. Balaz, J. I. Brand, and P. A. Dowben, J. Phys. Cond. Matter **16**, L139 (2004).

[10] E. Day, M. J. Diaz, and S. Adenwalla, J. Phys. D: Appl. Phys. **39**, 2920 (2006).

[11] A. N. Caruso, P. A. Dowben, S. Balkir, N. Schemm, K. Osberg, R. W. Fairchild, O. Barrios Flores, S. Balaz, A. D. Harken, B. W. Robertson, and J. I. Brand, Mater. Sci. Engineering B **135**, 129 (2006).

[12] K. Osberg, N. Schemm, S. Balkir, J. I. Brand, S. Hallbeck, P. Dowben, and M. W. Hoffman, IEEE Sensors Journal **6**, 1531 (2006).

[13] S.-D. Hwang, K. Yang, P. A. Dowben, A. A. Ahmad, N. J. Ianno, J. Z. Li, J. Y. Lin, H. X. Jiang, and D. N. McIlroy, Appl. Phys. Lett. **70**, 1028 (1997).

[14] S.-D. Hwang, N. Remmes, P. A. Dowben, and D. N. McIlroy, J. Vac. Sci. Technol. A **15**, 854 (1997).

[15] L. Carlson, D. LaGraffe, S. Balaz, A. Ignatov, Ya. B. Losovyj, J. Choi, P. A. Dowben, J. I. Brand, Applied Physics A **89**, 195 (2007).

[16] P. A. Dowben, O. Kizilkaya, J. Liu, B. Montag, K. Nelson, I. Sabirianov, J. I. Brand, Materials Letters **63**, 72 (2009).

[17] N. Hong, M. A. Langell, J. Liu,1 O. Kizilkaya, and S. Adenwalla, J. Appl. Phys., **107**, 024513 (2010)

[18] H. Takizawa, N. Haze, K. Okamoto, K. Uheda, and T. Endo, Materials Research Bulletin **37**, 113 (2002).

[19] U. Kuhlmann, H. Werheit, J. Pelloth, W. Keune, and T. Lundstrom, Physica Status Solidi B **187**, 43 (1995).

[20] U. Kuhlmann, H. Werheit, T. Dose, and T. Lundstrom, J. Alloys and Compounds **186**, 187 (1992).

[21] H. Werheit, R. Schmechel, V. Kueffel, and T. Lundstrom, J. Alloys and Compounds **262**, 372 (1997).

[22] H. Matsuda, T. Nakayama, K. Kimura, Y. Murakami, H. Suematsu, M. Koboyashi, and I. Higashi, Phys. Rev. B **52**, 6102 (1995).

[23] D. N. McIlroy, S.-D. Hwang, K. Yang, N. Remmes, P. A. Dowben, A. A. Ahmad, N. J. Ianno, J. Z. Li, J. Y. Lin, and H. X. Jiang, Appl. Phys. A **67,** 335 (1998).

[24] S.-D. Hwang, N. B. Remmes, P. A. Dowben, and D. N. McIlroy, J. Vac. Sci. Technol. B **14**, 2957(1996).

[25] A. Yu. Ignatov, Ya. B. Losovyj, L. Carlson, La Graffe, J. I. Brand, and P. A. Dowben, J. Appl. Phys. **102**, 083520 (2007).

[26] P. A. Dowben, A. Yu. Ignatov, J. Liu, and R. Skomski, J. Appl. Phys. **103**, 07D125 (2008).

[27] S. W. Lee, J. Mazurowski, W. L. Obrien, Q. Y. Dong, J. J Jia, T. A. Callcott, Y. X. Tan, K. E. Miyano, D. L. Ederer, D. R Mueller, and P. A. Dowben, J. Appl. Phys. **74**, 6919-6924 (1993).

[28] I. Jiménez, D. G. J. Sutherland, T. van Buuren, J. A. Carlisle, L. J. Terminello, and F. J. Himpsel, Phys. Rev. B **57**, 13167 (1998).

[29] S. Lee, P. A. Dowben, A. T. Wen, A. P. Hitchcock, J. A. Jr Glass, and J. T. Spencer, J. Vac. Sci. Technol. A **10**, 881 (1992).

[30] J. A. Bearden, and A.F. Burr, Rev. Mod. Phys. **39**, 125 (1967).

[31] T. M. Hayes, and J. B. Boyce, Solid State Physics, edited by H. Ehrenreich, F. Seitz, and D. Turnbull (Academic, New York, 1982) Vol. 37, P. 173.

[32] M. F. Hawthorne, Accounts of Chemical Research **1**, 281 (1968).

[33] R. B. King, Chem. Rev. **101**, 1119 (2001).

[34] J. Liu, G. Luo, W-N Mei, O. Kizilkaya, E. D. Shepherd, J. I. Brand, and P. A. Dowben, J. Phys. D: Appl. Phys. **43**, 085403 (2010); G. Luo, J. Lu, J. Liu, W-N Mei, and P.A. Dowben, Materials Science and Engineering B **175,** 1 (2010).

[35] B. Delley, J. Chem. Phys. **92**, 508 (1990).

[36] B. Delley, J. Chem. Phys. **113**, 7756 (2000).

[37] S.-R. Liu, H.-J. Zhai, and L.-S. Wang, Phys. Rev. B **65**, 113401 (2002).

[38] C. F. Guerra, J-W Handgraaf, E. J. Baerends, and F. M. Bickelhaupt J. Comput. Chem. **25,** 189 (2004).

[39] M.S. Co, W. A. Hendrickon, Kieth O. Hodgson and S. Doniach, J. Am.Chem. Soc. **105**, 1144 (1983).

[40] S. Lee, J. Mazurowski, G. Ramseyer and P. A. Dowben, J. Appl. Phys. **72**, 4925 (1992).

[41] W. Kleemann, P. Borisov, V. V. Shvartsman, S. Bedanta, A. Tkach and P. M. Vilarinho, J. Magn. Magn. Mat. **321**, 1785 (2009).

[42] W. Kleemann, S. Bedanta, P. Borisov, V. V. Shvartsman, S. Miga, J. Dec, A. Tkach and P. M. Vilarinho, Eur. Phys. J. B **71**, 407 (2009).

[43] V. V. Shvartsman, S. Bedanta, P. Borisov, W. Kleemann, A. Tkach and P. M. Vilarinho, Phys Rev. Lett. **101**, 165704 (2008).

[44] W. Kleemann, V. V. Shvartsman, S. Bedanta, P. Borisov, A. Tkach and P. M. Vilarinho, J. Phys. Cond. Matter **20**, 434216 (2008).

[45] J. A. Colón Santana, R. Skomski, V. Singh, V. Palshin, A. Petukhov, Ya. B. Losovyj, A. Sokolov, P. A. Dowben and I. Ketsman, J. Applied Physics **105,** 07A930 (2009).

Publications

1. **Jing Liu**, Jie Xiao, Seok-Bong Choi, P. Jeppson, L. Jarabek, Ya.B. Losovyj, A.N. Caruso and P.A. Dowben, "The Electronic Structure of Co and Ni Tetraazaannulenes", *Journal of Physical Chemistry* B **110** (2006) 26180-26184
2. P.A. Dowben, A.Yu. Ignatov, **Jing Liu**, and Ralph Skomski, "The Local Environment of Co in B5CHx", *Journal of Applied Physics* **103** (2008) 07D125
3. Ya.B. Losovyj, Melanie Klinke, En Cai, Idaykis Rodriguez, Jiandi Zhang, L. Makinistian, A. G. Petukhov, E. A.Albanesi, P. Galiy, Ya. Fiyala, **Jing Liu** and P.A. Dowben "The Electronic Structure of Surface Chains in the Layered Semiconductor In4Se3(100)", *Applied Physics Letters* **92** (2008) 122107
4. Danqin Feng, **Jing Liu**, Adam P. Hitchcock, A.L. David Kilcoyne, Tolek Tyliszczak, Norman Riehs, Eckart Rühl, John D. Bozek, David McIlroy and Peter A. Dowben, "Photo-fragmentation of the *closo*-Carboranes Part 1: Energetics of Decomposition", *Journal of Physical Chemistry* A **112** (2008) 3311-3318
5. **Jing Liu**, Ya.B. Losovyj, Takashi Komesu, P.A. Dowben, L. Makinistian, E. A. Albanesi, A. G. Petukhov, P. Galiy, Ya. Fiyala, "The Bulk Band Structure and Inner Potential of Layered In4Se3", *Appl. Surf. Sci.* **254** (2008) 4322-4325
6. Ya.B. Losovyj, L. Makinistian, E. A. Albanesi, A. G. Petukhov, **Jing Liu**, P. Galiy, O.R. Dveriy, P.A. Dowben, "The Anisotropic Band Structure of Layered In4Se3(001)", *J. Appl. Phys.* **104** (2008) 083713

7. P.A. Dowben, Orhan Kizilkaya, **Jing Liu**, B. Montag, K. Nelson, I. Sabirianov and J.I. Brand, "3d Transition Metal Doping of Semiconducting Boron Carbides", *Materials Letters* **63** (2009) 72-74

8. Nina Hong, M. A. Langell, **Jing Liu**, Orhan Kizilkaya and S. Adenwalla1, "Ni Doping of Semiconducting Boron Carbide", *J. of Appl. Phys.* **107**, (2010) 024513

9. **Jing Liu**, Guangfu Luo, Wai-Ning Mei, Orhan Kizilkaya, Eric D. Hepherd, J. I. Brand and P. A. Dowben, "The Local Structure of Transition Metal Doped Semiconducting Boron Carbides", *J. of Physics D-Applied physics* **43** (2010) 085403

10. Guangfu Luo, Jing Lu, **Jing Liu**, Wai-Ning Mei and P.A. Dowben, " Insights into the Local Electronic Structure of Semiconducting Boron Carbides in the Vicinity of Transition Metal Dopants", *Materials Science and Engineering: B*, **175**, (2010) 1

11. Eckart Ruehl, Norman F. Riehs, Swayambhu Behera, Justin Wilks, **Jing Liu**, H. - W. Jochims, Anthony N.Caruso, Neil M. Boag, Jeffry A. Kelber and Peter A. Dowben, "Photofragmentation of the *closo*-Carboranes Part II: VUV Assisted Dehydrogenation in the *closo*-Carboranes and Semiconducting B10C2Hx Films", *Journal of Physical Chemistry* A **114** (2010) 7284-7291

12. **Jing Liu**, P. A. Dowben, Guangfu Luo, Wai-Ning Mei, Orhan Kizilkaya, Anil Kumar Rajapitamahuni, Andre Sokolov, Sudarshan Karki and Anthony Caruso, **"**The Local Structure and I-V Characteristic of Chromium Doped Semiconducting

Boron Carbide", *Mater. Res. Soc. Symp. Proc.*, (2011), 1307: mrsf10-1307-cc05-01.

13. **Jing Liu**, Eckart Rühl, Adam P. Hitchcock, D.N. McIlroy, John D. Bozek, A.L. David Kilcoyne, Tolek Tyliszczak, A. Knop-Gericke, Neil M. Boag, and P. A. Dowben, "Photo-fragmentation of the *closo*-Carboranes Part III: Double Cation Fragmentation", in preparation.